X-ray Timing of Young Pulsars

A DISSERTATION PRESENTED
BY
ROBERT FREDERIC ARCHIBALD
TO
THE DEPARTMENT OF PHYSICS

IN PARTIAL FULFILLMENT OF THE REQUIREMENTS
FOR THE DEGREE OF
DOCTOR OF PHILOSOPHY
IN THE SUBJECT OF
PHYSICS

MCGILL UNIVERSITY
MONTREAL, QUEBEC
MAY 2017

Thesis advisor: Professor Victoria Kaspi Robert Frederic Archibald

X-ray Timing of Young Pulsars

Abstract

Pulsars are the rotating compact remnants of exploded massive stars. The region surrounding the neutron star, known as the magnetosphere, has properties which are determined by the magnetic field of the star. In this thesis, I present several observational results involving rotation-powered radio pulsars and magnetars which indicate that pulsar magnetospheres have a more complex structure than a simple dipole, and that the magnetosphere can have a strong effect on all the observed properties of neutron stars.

One way to probe the pulsar magnetosphere is through the measurement of braking indices. A braking index quantifies the dependence of the torque on the spin frequency. In Chapter 4 I present a long-term timing study of the rotation-powered pulsar PSR J1846−0258, where we show that the change in braking index reported in this source is long-lived. The most plausible explanation for this changed braking index appears to be due to a change in magnetospheric configuration.

In Chapter 5, I present the measurement of a new braking index for the rotation-powered pulsar PSR J1640−4631 of $n = 3.15 \pm 0.03$ – the first measured braking index higher than the canonical three of a magnetic dipole. This result demonstrates that other physical mechanisms, such as mass or magnetic quadrupole moments most likely need to be taken into account to describe pulsar spin-down & energetics.

Another way to probe the magnetospheres of pulsars is by studying the extreme variability seen in the magnetar class. In Chapter 6 I present two years of flux and spin evolution monitoring of the magnetar 1E 1048.1−5937 following an outburst. By comparing to previous outbursts from the source, we show that this pattern of behaviour repeats itself with a quasi-period of ∼1800 days. This behaviour, when compared to similar less extreme events seen in rotation-powered pulsars, appears to implicate processes in the stellar magnetosphere.

In Chapter 7, I present the results of monitoring the magnetar 4U 0142+61 over two outbursts, including one with a net spin-down timing event, and compare this timing event to previous such events in other pulsars with high magnetic fields and discuss net spin-down glitches now seen in several young, high-B pulsars. The observations that these spin-down events occur in only high-B sources strongly implicates the influence of a large magnetic field in spin-down events and, coupled with the radiatively loud nature of the plurality of spin-down events, suggests an origin in the magnetosphere of the star.

In Chapter 8 I present observations of a magnetar-like outburst from the high-magnetic-field pulsar PSR J1119−6127, providing an unambiguous connection between the radio pulsar and magnetar populations.

Finally, in Chapter 9, I put these new results in context with recent advances in neutron-star astrophysics, and speculate on avenues for future advancement in the field.

Directeur de thése: Professeure Victoria Kaspi Robert Frederic Archibald

X-ray Timing of Young Pulsars

Résumé

Un pulsar est le résidu compact issu de l'explosion d'une étoile massive survenant lorsque cette dernière a épuisé son combustible nucléaire. Les caractéristiques de la région hautement magnétisée entourant une étoile à neutrons, connue sous le nom de magnétosphère, sont déterminées par le champ magnétique de l'étoile même. Dans cette thèse, plusieurs résultats issus d'observations seront présentés. Ces résultats indiquent, d'une part, que les magnétosphères des pulsars possèdent des structures plus complexes que le simple modèle dipolaire et, d'autre part, que ces magnétosphères peuvent avoir un effet important sur toutes les propriétés observées des étoiles à neutrons. Afin de mieux comprendre la physique entourant les magnétosphères, nous pouvons mesurer les indices de freinage des pulsars, une mesure qui quantifie la dépendance du torque de l'étoile sur sa fréquence de rotation.

Le Chapitre 4 présente une étude chronométrique à long terme du pulsar PSR J1846−0258 démontrant que le changement dans l'indice de freinage de cette source est durable. L'explication la plus plausible concernant la nature de ce changement serait liée à une modification de la configuration de la magnétosphère.

Le Chapitre 5 discute de la mesure d'un nouvel indice de freinage pour PSR J1640−4631 de $n = 3.15 \pm 0.03$. C'est la première fois que l'on observe un indice de freinage supérieur à la valeur canonique de $n = 3$, associée à un champ magnétique dipolaire.

L'analyse de l'extrême variabilité des magnétoiles peut également nous aider à mieux comprendre les magnétosphères d'étoiles à neutrons. Un suivi d'une durée de deux ans de l'évolution du flux et de la rotation suivant un événement radiatif de la magnétoile 1E 1048.1−5937 est présenté dans le Chapitre 6. En comparant ces résultats avec d'autres événements radiatifs provenant de cette même source, nous démontrons que ce type de comportement se répète quasi-périodiquement (quasi-période de ∼1800 jours). Des processus magnétosphériques semblent être à la source du phénomène lorsque comparés à des événements semblables (mais moins extrêmes) observés chez certains pulsars typiques qui tirent leur énergie de leur rotation.

Dans le Chapitre 7, les résultats d'une campagne d'observation de la source 4U 0142+61 sont présentés. Deux événements radiatifs sont survenus lors de ces observations, et une diminution nette de la fréquence de rotation suivant l'un de ces événements a été constatée. Cette irrégularité dans le ralentissement de la vitesse de rotation est comparée à d'autres cas similaires observés chez d'autres pulsars ayant de forts champs magnétiques. Le fait que de semblables changements dans la vitesse de rotation ne sont observés que chez des pulsars ayant de puissants champs magnétiques, en addition avec le dégagement important de radiation accompagnant ces types d'événements, suggère que ces phénomènes proviennent de magnétosphères d'étoiles à neutrons ayant des champs magnétiques intenses.

Le Chapitre 8 présente des observations d'événements radiatifs, semblables à ceux des magnétoiles, provenant du pulsar PSR J1119−6127. Cette source est doté d'un puissant champ magnétique, ce qui expose une connexion claire et non ambiguë entre la population de pulsars radio et celle des magnétoiles.

Le Chapitre 9 conclut cette thèse en mettant ces nouveaux résultats en contexte avec les progrès les plus récents en astrophysique, et spécule sur les possibles avancements futurs en ce qui concerne l'étude des pulsars.

Contents

Listing of figures

Listing of tables

For the family.

Acknowledgments

First and foremost I thank my supervisor, Vicky Kaspi, for many years of guidance and support. I would also like to thank Paul Scholz for starting the `swiftmonitor` program, and many fruitful discussions & collaborations over the past few years.

I am also indebted to Maggie Livingstone, Rim Dib, and Fotis Gavriil as many of the results presented in this thesis are continuations of projects they once led.

Thanks also to all members of the pulsar group, and to my colleagues at McGill –in addition to creating a world class place to do research, you've also made a fun place to spend the last few years.

Finally, I would like to thank Emilie Parent for translating the abstract.

* * *

The research presented in the manuscripts on which this thesis is based has been published elsewhere, in collaboration with other authors, and has been generously funded by various Canadian and international agencies. Below, I reproduce the acknowledgement sections of the original manuscripts.

Chapter 4: On the Braking Index of the Unusual High-B Rotation-Powered Pulsar PSR J1846−0258

R.F.A. acknowledges support from an NSERC Alexander Graham Bell Canada Graduate Scholarship and a Walter C. Sumner Memorial Fellowship. V.M.K. receives support from an NSERC Discovery Grant and Accelerator Supplement, Centre de Recherche en Astrophysique du Quebéc, an R. Howard Webster Foundation Fellowship from the Canadian Institute for Advanced Study, the Canada Research Chairs Program and the Lorne Trottier Chair in Astrophysics and Cosmology. We thank R. Ferdman and E. Madsen for useful discussions. We acknowledge the use of public data from the *Swift* data archive. This research has made use of data obtained through the High Energy Astrophysics Science Archive Research Center Online Service, provided by the NASA/Goddard Space Flight Center.

Chapter 5: A High Braking Index for a Pulsar

This work made use of data from the *NuSTAR* mission, a project led by the California Institute of Technology, managed by the Jet Propulsion Laboratory, and funded by the National Aeronautics and Space Administration. Parkes radio telescope is part of the Australia Telescope National Facility which is funded by the Commonwealth of Australia for operation as a National Facility managed by CSIRO. We also thank an anonymous referee for helpful comments that improved the paper. R.F.A. acknowledges support from an NSERC Alexander Graham Bell Canada Graduate Scholarship. E.V.G. received support from the National Aeronautics and Space Administration through Chandra Award Number GO5-16061X issued by the Chandra X-ray Observatory Center, which is operated by the Smithsonian Astrophysical Observatory for and on behalf of the National Aeronautics Space Administration under contract NAS8-03060. V.M.K. receives support from an NSERC Discovery Grant and Accelerator Supplement, Centre de Recherche en Astrophysique du Quebéc, an R. Howard Webster Foundation Fellowship from the Canadian Institute for Advanced Study, the Canada Research Chairs Program, and the Lorne Trottier Chair in Astrophysics and Cosmology. Part of this work was performed under the auspices of the U.S. Department of Energy by Lawrence Livermore National Laboratory under Contract DE-AC52-07NA27344.

Chapter 6: Repeated, Delayed Torque Variations Following X-Ray Flux Enhancements in the Magnetar 1E 1048.1−5937

We thank Jamie Stevens for carrying out the ATCA observations. The Australia Telescope Compact Array is part of the Australia Telescope National Facility which is funded by the Commonwealth of Australia for operation as a National Facility managed by CSIRO[i]. R.F.A. receives support from a Walter C. Sumner Memorial Fellowship. V.M.K. receives support from an NSERC Discovery Grant and Accelerator Supplement, Centre de Recherche en Astrophysique du Quebéc, an R. Howard Webster Foundation Fellowship from the Canadian Institute for Advanced Study, the Canada Research Chairs Program and the Lorne Trottier Chair in Astrophysics and Cosmology. We thank M. Lyutikov, D. Tsang, and K. Gourgouliatos for useful discussions. We acknowledge the use of public data from the *Swift* data archive. This research has made use of data and software provided by the High Energy Astrophysics Science Archive Research Center (HEASARC), which is a service of the Astrophysics Science Division at NASA/GSFC and the High Energy Astrophysics Division of the Smithsonian Astrophysical Observatory. The scientific results reported in this article are based in part on observations made by the *Chandra* X-ray Observatory. This research has made use of CIAO software provided by the *Chandra* X-ray Center (CXC).

---

[i] `http://www.atnf.csiro.au/research/publications/Acknowledgements.html`

Chapter 7: Swift observations of two outbursts from the magnetar 4U 0142+61

We are grateful to the *Swift* team for their flexibility in the scheduling of the timing monitoring campaign of 4U 0142+61. We thank A. Cumming for helpful discussions. RFA acknowledges support from an NSERC Alexander Graham Bell Canada Graduate Scholarship. VMK receives support from an NSERC Discovery Grant and Accelerator Supplement, Centre de Recherche en Astrophysique du Quebec, an R. Howard Webster Foundation Fellowship from the Canadian Institute for Advanced Study, the Canada Research Chairs Program and the Lorne Trottier Chair in Astrophysics and Cosmology. PS acknowledges support from a Schulich Graduate Fellowship from McGill University. We acknowledge the use of public data from the *Swift* data archive. This research has made use of data obtained through the High Energy Astrophysics Science Archive Research Center Online Service, provided by the NASA/Goddard Space Flight Center.

Chapter 8: A Magnetar-like Outburst from a High-B Radio Pulsar

The authors thank the operations teams of *NuSTAR*, particularly Karl Forster, and *Swift* for their speed and flexibility scheduling these observations. We thank *Fermi*-LAT Collaboration for the public data and tools used in this work. This work made use of data from the *NuSTAR* mission, a project led by the California Institute of Technology, managed by the Jet Propulsion Laboratory, and funded by the NASA. We acknowledge the use of public data from the *Swift* data archive. R.F.A. acknowledges support from an NSERC CGSD. V.M.K. receives support from an NSERC Discovery Grant, an Accelerator Supplement and from the Gerhard Herzberg Award, an R. Howard Webster Foundation Fellowship from the Canadian Institute for Advanced Study, the Canada Research Chairs Program, and the Lorne Trottier Chair in Astrophysics and Cosmology. S.P.T acknowledges support from a McGill Astrophysics postdoctoral fellowship. P.S. acknowledges support from a Schulich Graduate Fellowship.

Contribution of Authors

The university guidelines for a manuscript-based thesis state that PhD candidates have the option of including, as part of the thesis, the text of one or more papers submitted, or to be submitted, for publication, or the clearly duplicated text of one or more published papers.

In accordance with the above, the results presented in this thesis are original work that was, or will be, published in the following refereed articles:

CHAPTER 4: ON THE BRAKING INDEX OF THE UNUSUAL HIGH-B ROTATION-POWERED PULSAR PSR J1846−0258

Chapter 4 contains the lightly edited text of Archibald et al. (2015b):
R.F. Archibald, V. M. Kaspi, A. P. Beardmore, N. Gehrels, and J. A. Kennea. On the Braking Index of the Unusual High-B Rotation-Powered Pulsar PSR J1846−0258. *The Astrophysical Journal*, 810:67, Sept. 2015

I performed the data reduction and analysis for the *Swift* and *RXTE* data including the timing analyses, pulse profile analyses, and spectral analyses. V. Kaspi was the PI on both the *Swift* and *RXTE* programmes. I wrote the text with guidance from V. Kaspi, and with comments from my coauthors.

CHAPTER 5: A HIGH BRAKING INDEX FOR A PULSAR

Chapter 5 contains the lightly edited text of Archibald et al. (2016c):
R.F. Archibald, E. V. Gotthelf, R. D. Ferdman, V. M. Kaspi, S. Guillot, F. A. Harrison, E. F. Keane, M. J. Pivovaroff, D. Stern, S. P. Tendulkar, and J. A. Tomsick. A High Braking Index for a Pulsar. *The Astrophysical Journal Letters*, 819:L16, Mar. 2016

I performed the data reduction and timing analysis for the *NuSTAR* data and performed the timing noise simulations. V. Kaspi and I designed the timing campaign used in this work. E. F. Keane performed the Parkes observations, and R. D. Ferdman searched the radio data for pulsations. I wrote the text with guidance from V. Kaspi, and with comments from my co-authors.

CHAPTER 6: REPEATED, DELAYED TORQUE VARIATIONS FOLLOWING X-RAY FLUX ENHANCEMENTS IN THE MAGNETAR 1E 1048.1−5937

Chapter 6 contains the lightly edited text of Archibald et al. (2015c):
R.F. Archibald, V. M. Kaspi, C.-Y. Ng, P. Scholz, A. P. Beardmore, N. Gehrels, and J. A. Kennea. Repeated, Delayed Torque Variations Following X-Ray Flux Enhancements in the Magnetar 1E 1048.1−5937. *The Astrophysical Journal*, 800:33, Feb. 2015

V. Kaspi was the PI on both the *Swift* and *Chandra* programmes. I performed the data reduction and analysis for the *Swift* data including the timing analyses, pulse profile analyses, and spectral analyses. C.Y. Ng analysed the Australia Telescope Compact Array data. I wrote the text with guidance from V. Kaspi, and with comments from my co-authors.

CHAPTER 7:

Chapter 7 contains the lightly edited text of Archibald et al. (2017b):
R.F. Archibald, V. M. Kaspi, P. Scholz, A. P. Beardmore, N. Gehrels, and J. A. Kennea. Swift observations of two outbursts from the magnetar 4U0142+61. *The Astrophysical Journal*, 834:163, Jan. 2017.

V. Kaspi was PI on the *Swift* programme. I performed the data reduction and analysis for the *Swift* data including the timing analyses, pulse profile analyses, and spectral analyses.

I wrote the text with guidance from V. Kaspi, and with comments from my co-authors.

CHAPTER 8:

Chapter 8 contains the lightly edited text of Archibald et al. (2016a):
R.F. Archibald, V. M. Kaspi, S. P. Tendulkar, and P. Scholz. A Magnetar- like Outburst from a High-B Radio Pulsar. *The Astrophysical Journal Letters*, 829:L21, Sept. 2016

I performed the data reduction for the *Fermi* and *Swift* data and performed the timing analysis and pulsed flux analysis. P. Scholz reduced the *XMM-Newton* data. S. Tendulkar reduced the *NuSTAR* data, and performed the spectral fitting. V. Kaspi led the interpretation of the results and was PI on the *Swift* and *NuSTAR* programmes.

Ask God why he made the gem so small, and
why so huge the granite; it's so man might
know to place the greater value on it.

Robert Burns

1

Pulsar Basics

Neutron stars are the most compact form of matter known to exist in the universe. The existence, and name, of these exotic objects was first put forth by Baade & Zwicky (1934a,b), who proposed that the energetics of supernovae could be explained by a rapid transition between a normal star and a *neutron star* – an extremely dense object composed primarily of neutrons. Remarkably, the proposition that these exotic objects exist, made shortly after the discovery of the neutron (Chadwick, 1932), has held to be correct, although observational evidence of this would not appear for three decades.

That first observational evidence that neutron stars might exist came in 1962, with the discovery of X-rays from outside the Solar System (Giacconi et al., 1962). Later

X-ray sounding rockets would detect distinct sources – including the Crab (Bowyer et al., 1964a) and Scorpius X-1 (Bowyer et al., 1964b). By 1964 it was suggested that thermal emission from young neutron stars could be the source of this X-ray emission (Chiu & Salpeter, 1964; Oda, 1964; Morton, 1964). Later observations of pulsars (see § 1.1) would prove further evidence of the existence of neutron stars.

These young neutron stars, as postulated by Baade & Zwicky, are formed by the death of massive stars in core-collapse supernovae. Indeed it is the release of the gravitational binding energy from forming the neutron star that powers the supernova. In order for this explosion to produce a neutron star, rather than a black hole, the progenitor star must have an initial mass of approximately $8M_\odot - 25M_\odot$, although the exact mass range is debated, and depends on factors such as the metallicity and binarity of the progenitor (e.g. Muno, 2007).

PULSARS

In 1967, Jocelyn Bell and collaborators at the Mullard Radio Astronomy Observatory detected a new class of astrophysical object (Hewish et al., 1968). They dubbed this new class of objects "pulsars", a portmanteau of "PULSating stARs," as they appeared to pulse incredibly regularly with a pulse period of approximately a second. This new source class inspired several models including active regions on rapidly rotating white dwarf stars (Ostriker, 1968), the gravitational lens effect associated with a neutron star binary (Saslaw, 1968), and rotating neutron stars (Gold, 1968). Shortly after, observations of faster spinning pulsars (Large et al., 1968; Staelin & Reifenstein, 1968), including eventually pulsars with a millisecond spin period (Backer et al., 1982), would leave beamed emission from rotating neutron stars as the preferred model to describe these sources (Gunn & Ostriker, 1969).

The first detection of pulsars in the X-ray band came soon after with a rocket launched on the 16th of March, 1968 which detected pulsations from the direction of the Crab Nebula (Boldt et al., 1969; Ducros et al., 1970). Thus, while pulsars were initially discovered, and indeed are most frequently observed in the radio band, they are very broadband emitters. As more and more pulsars were discovered, it became useful to categorize them into the 'bestiary,' which I will lay out in § 1.3.

NEUTRON STARS

The measured masses of neutron stars are between $\sim 1.1 - 2\,M_{\odot}$ [i]. Coupled with measured radii between $\sim 7 - 14$ km, neutron stars are quite dense objects (see Özel & Freire, 2016, for a compiled list of all measured neutron star masses & radii). A rough calculation shows that even the average density of these objects is $\sim 10^{15}\,\mathrm{g\,cm^{-3}}$ – greater than the density of the nucleus of an atom. With this in mind the exact mass-radius relation is an open topic of research as, by measuring the mass-radius relation in neutron stars, we probe the equation of state for supra-nuclear matter which is currently not known (see e.g. Lattimer & Prakash, 2001; Potekhin, 2010).

THE INTERIOR

While the exact mass-radius relation of neutron stars is unknown, we do have a basic understanding of their structure. Neutron stars are held up from complete gravitational collapse by the support of neutron degeneracy pressure. Due to the interplay

---

[i] While no physical laws prevent a neutron star existing with a mass as low as $\sim$0.1 $\mathrm{M_{\odot}}$, there are no proposed astrophysical processes to produce a neutron star with such a low mass; see Haensel et al. (2002).

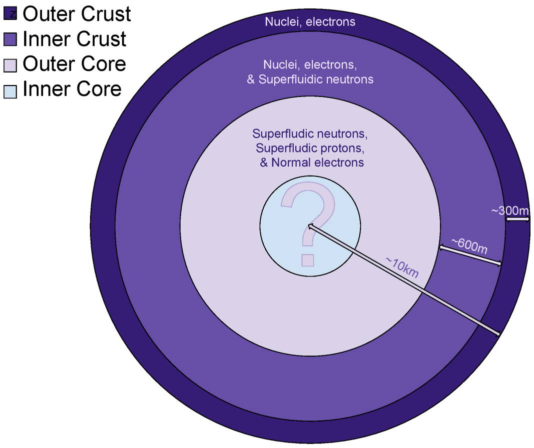

Figure 1.1 A schematic diagram of a neutron star. Note that this is not to scale, and that different equations of state predict different radii, and thus different widths of each component.

of this degeneracy pressure, gravity, and transitions between different states of degenerate matter, a neutron star is not uniform throughout its bulk, but rather self-organizes itself into layers, which I shall briefly describe here, and is represented in Figure 1.1.

The outer crust of a neutron star is similar to the bulk composition of white dwarfs. It is composed of a solid lattice of heavy nuclei ranging from ^{56}Fe near the surface to heavier nuclei towards the inner crust, and a sea of relativistic degenerate electrons (Haensel, 2001).

The inner crust starts at the neutron drip density $\sim 4 \times 10^{11}\,\mathrm{g\,cm^{-3}}$. At this density, the neutron chemical potential is equivalent to the rest mass of the neutron, and it becomes energetically favourable for the neutrons to leave, or ‘drip’ from the nuclei (Pethick & Ravenhall, 1991). These free neutrons form a superfluid that surrounds a lattice of heavy neutron-rich nuclei (Anderson & Itoh, 1975; Haensel, 2001). This superfluid will prove to be an independent source of angular momentum from the solid components (Anderson & Itoh, 1975), as will be discussed in §2.1.

At the boundary between the inner crust and outer core matter enters a series of unusual states referred to as 'nuclear pasta'. This name comes from the variety of shapes nuclei attain from almost round (gnocchi), to long cylinders (spaghetti), to slabs (lasagne), to slabs with cylindrical voids (bucatini), to slabs with voids (Swiss cheese[ii]), until all nucleons are free (sauce)(Lattimer & Prakash, 2004). For a more thorough review of the states of nuclear pasta, see Watanabe & Maruyama (2011).

The core regions contain the majority, up to 99%, of the mass of a neutron star. The outer core begins when all nuclei have fully dissolved into a relativistic sea of superfluidic neutrons and superconducting superfluidic protons (Lattimer & Prakash, 2004).

The inner core is the least well understood part of the neutron star, as its density and pressure far exceed conditions that can be created in terrestrial laboratories. It has been proposed to be composed of exotic matter such as free quarks, pions, kaons, hyperons, or strange matter (Lattimer & Prakash, 2004).

THE EXTERIOR

Surrounding a neutron star is a region known as the *magnetosphere*. The magnetosphere is the plasma filled region surrounding the neutron star where the properties are determined by the magnetic field of the star.

The rotation of the strong magnetic fields possessed by neutron stars creates the electric field $\vec{E} = (\vec{\Omega} \times \vec{r}) \times \vec{B}$ where B is the surface magnetic field, Ω the angular frequency, and r the radius of the neutron star. At the surface of the neutron star,

---

[ii] I am unaware of who decided that Swiss cheese was an acceptable form of pasta.

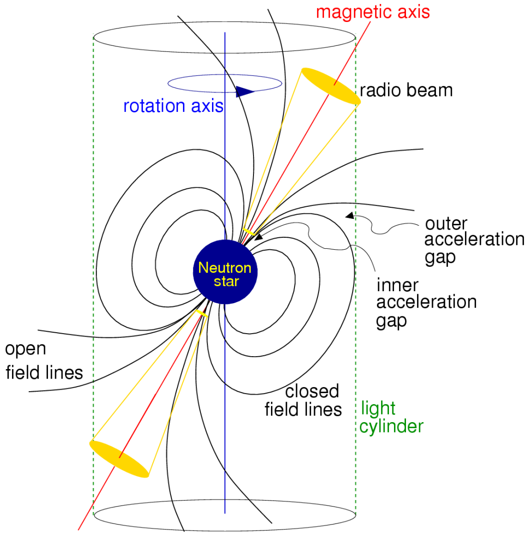

Figure 1.2 A schematic diagram of a neutron star magnetosphere from the Handbook of Pulsar Astronomy, Lorimer & Kramer (2005).

the component of this field parallel to the magnetic field will be $E = \frac{2\pi\nu R}{c}B$ (Lorimer & Kramer, 2005). This is strong enough to pull charged particles from the neutron star's surface. In order to obtain a force-free state, this fills the region surrounding the neutron star with a plasma with a charge density of

$$\rho_{GJ} = \frac{B\nu}{ec} \tag{1.1}$$

where e is the charge of an electron (Goldreich & Julian, 1969).

The extent of the magnetosphere is limited by the light cylinder. The light cylinder is defined by the radius from the rotation axis where a particle in co-rotation with the neutron star would need to travel at the speed of light ($r_{lc} = \frac{c}{2\pi\nu}$). The light cylinder sets the boundary between closed magnetic field lines, and open magnetic field lines, as can be seen in Figure 1.2 (Lyne & Graham-Smith, 1990).

While this Goldreich-Julian plasma-filled model of the magnetosphere above is illustrative, an analytic solution to the pulsar magnetosphere may not exist, and remains an active field of research (e.g. Spitkovsky, 2004; Chen & Beloborodov, 2014). Indeed, as we will see in § 1.4.1, many calculations are done in the vacuum limit of the magnetosphere (Deutsch, 1955), rather than the force-free plasma limit.

Aside from thermal emission from the surfaces of young, hot neutron stars, all the emission we see from neutron stars is thought to originate in the magnetosphere. Despite nearly 50 years of observations and theorizing, the exact mechanisms of pulsar emission remain elusive, and an active field of study (see e.g. Harding, 2007; Melrose & Yuen, 2016; Kalapotharakos et al., 2014). Here, I will briefly mention possible origin sites for the high energy emission we see from pulsars.

Pulsar emission comes from the acceleration of charged particles to relativistic speeds as the current strips them from the neutron star surface, and leave in a particle wind outside the light cylinder (Ruderman & Sutherland, 1975). These charged particles will travel along the magnetic field lines of the magnetosphere and, as the field lines are curved, the particles will be accelerated and will radiate via curvature radiation. In addition photons, such as those from the thermal surface emission of a pulsar, can interact with the high energy particles in the magnetosphere and be scattered to higher energy via Inverse Compton scattering (e.g. Lyne & Graham-Smith, 1990; Zhang & Harding, 2000). Models differ on where this acceleration takes place. In the inner acceleration gap, or polar cap emission model, this emission originates in the region defined by following the open field lines back to the surface of the neutron star – centred at the magnetic pole of the star (Ruderman & Sutherland, 1975). In the polar cap model, a return current may heat the neutron star surface near the polar cap, explaining the thermal radiation seem from small $10 - 100\,\mathrm{m}$ regions on some pulsars (Harding & Muslimov, 2001). Another possible emission region, the outer acceleration gap, is inside the light cylinder between the last closed field line and the first open field line known as the outer gap (Cheng et al., 1986; Wang et al., 2013).

THE PULSAR BESTIARY

As we see light from pulsars, they must be losing energy. Pulsars can draw the energy they emit from at least three distinct sources: through accretion, by drawing from rotational stores, and by extracting energy stored in magnetic fields. In this thesis, only isolated pulsars are studied so accretion does not play a role. Here, I will give the basic characteristics of pulsars which draw energy from their rotation & magnetic power stores.

ROTATION-POWERED PULSARS

The largest fraction of the pulsar population, with more than 2000 known members, are often referred to as 'radio pulsars' or 'rotation-powered pulsars' (RPPs). In Figure 1.3, referred to as a "P P-dot diagram", two of the main observables of RPPs are plotted against each other, the rotation period, P, and the change in that rotation period, $\dot{P}$, over time. As we shall see in the following sections, we can infer many things about a pulsar simply by where it falls on this diagram.

RPPs can be roughly divided into two categories: young pulsars whose spin characteristics are determined by birth, and the millisecond, or recycled pulsars whose spin characteristics are the end result of being spun up by an accretion process (e.g. Alpar et al., 1982; Radhakrishnan & Srinivasan, 1982).

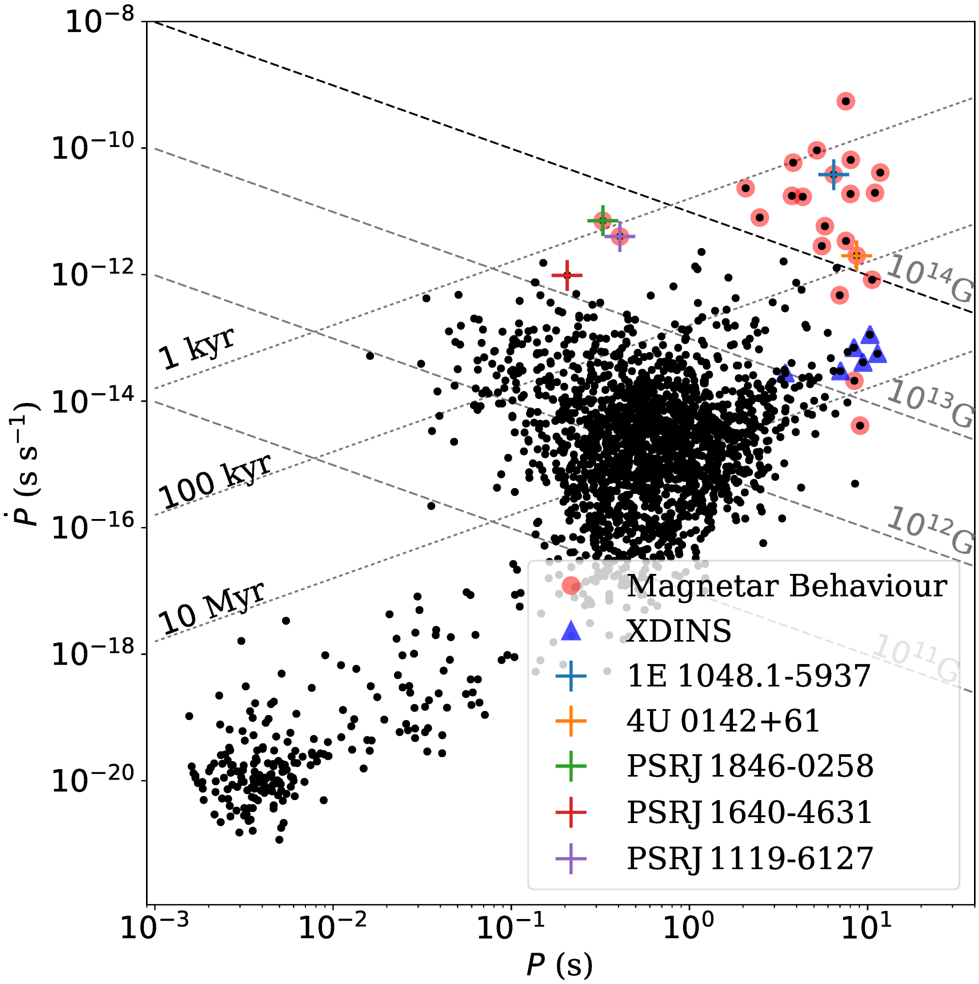

Figure 1.3 The $P - \dot{P}$ diagram displaying the spin parameters of all pulsars in the ATNF catalogue as of February 2017 (Manchester et al., 2005). The five pulsars studied in this thesis are indicated by coloured crosses. Lines of constant characteristic age, and constant magnetic field are shown. Pulsars which have displayed magnetar-like radiative behaviours (§ 1.5.1) are highlighted in red circles, and the XDINS (§ 1.4.3) are highlighted by blue triangles.

The bulk of the rotation-powered pulsar population, the large cluster of points in Figure 1.3, have spin periods of $\sim 1\,\mathrm{s}$. They have implied ages of $10^3 - 10^8$ years and magnetic fields from $\sim 10^{11} - 10^{13}\,\mathrm{G}$ (see §1.4.1 for details on characteristic ages and magnetic fields).

Compared to the bulk of the pulsar population, millisecond pulsars are old ($\sim 10^8 - 10^{10}$ years), and have much lower magnetic fields ($\sim 10^8 - 10^{10}\,\mathrm{G}$). Due to their past evolution, many millisecond pulsars are found to exist in binaries.

Both millisecond pulsars and bulk of the pulsar population are powered by extracting energy from their angular momentum stores (Gold, 1968; Pacini, 1967).

THE ENERGETICS OF ROTATION-POWERED PULSARS

The rotational energy, E, stored in an isolated pulsar can be described as

$$E = 2\pi^2 I \nu^2 \tag{1.2}$$

where ν is the rotation frequency[iii], and I is the moment of inertia of the pulsar. For a canonical pulsar with a mass of $1.4 M_\odot$ and a radius of $10\,\mathrm{km}$, and working with the incorrect yet still informative estimate that a pulsar is a uniform sphere of constant density, the moment of inertia of a pulsar is $I = 10^{45}\,\mathrm{g\,cm^2}$ (see e.g. Lyne & Graham-Smith, 1990). The total amount of rotational energy available to a pulsar is then

$$E = 2\pi^2 I \nu^2 \simeq 2 \times 10^{46} \left(\frac{\nu}{1\mathrm{Hz}}\right)^2 \mathrm{erg}. \tag{1.3}$$

Under the assumption that the moment of inertia of a pulsar is constant, the amount

---

[iii] The spin parameters of a pulsar can also be expressed in terms of angular frequency (ω), or spin period (P). These are all related as $\omega = 2\pi\nu = 2\pi/P$.

of energy loss per unit time can be found by taking a time derivative, giving[iv]:

$$\dot{E} = -4\pi^2 I\dot{\nu}\nu \simeq 10^{32}\left(\frac{\nu}{1\mathrm{Hz}}\right)\left(\frac{\dot{\nu}}{10^{-14}\mathrm{Hz\ s}^{-1}}\right)\mathrm{erg\ s}^{-1}. \tag{1.4}$$

This is usually referred to as a pulsar's spin-down luminosity. It represents the maximum amount of energy a pulsar can emit drawing *only* from its rotational energy stores.

Generally, it is thought that the dominant energy loss mechanism for rotation-powered pulsars is magnetic dipole radiation (Gunn & Ostriker, 1969). A rotating magnetic dipole will radiate energy at a rate of (e.g. Tsang, 1997):

$$\dot{E} = -\frac{32\pi^4 m_0^2 \sin^2\alpha}{3c^3}\nu^4 \tag{1.5}$$

where m_0 is the magnetic moment, c is the speed of light, and α is the misalignment angle between the spin axis and the magnetic axis.

If we assume all power lost is emitted via magnetic dipole radiation we can equate the spin-down power (Equation 1.4), and dipole radiation (Equation 1.5). We can see the prediction that:

$$\dot{\nu} = \frac{8\pi^2 m_0^2 \sin^2\alpha}{3c^3 I}\nu^3 \tag{1.6}$$

i.e. the spin-down rate is proportional to the spin-frequency raised to the third power.

Furthermore, if we model a neutron star as a point dipole, its magnetic moment is

$$m_0 \simeq B_s R^3 \tag{1.7}$$

[iv] Throughout this document, I follow the convention that a superscript "dot" represents a time derivative.

where B_s is the surface magnetic field, and R the radius of the neutron star (e.g. Lyne & Graham-Smith, 1990). With this and Equation 1.6 we can, simply by measuring the spin frequency and spin-down rate of a neutron star, estimate:

$$B_s = \left(\frac{3Mc^3}{20\pi R^4 \sin^2 \alpha}\right)^{\frac{1}{2}} \left(\frac{-\dot{\nu}}{\nu^3}\right)^{\frac{1}{2}} = 3.2 \times 10^{19} \left(\frac{-\dot{\nu}}{\nu^3}\right)^{\frac{1}{2}} \text{ G}. \tag{1.8}$$

B_s is referred to as the spin-down inferred dipolar magnetic field of the pulsar, and is often used as a proxy for the actual magnetic field.

Braking Indices

As we saw in the prior section, many of the quoted properties of pulsars, such as the surface magnetic field and the spin-down luminosity, are based on the assumption that pulsars are well modelled as a magnetic dipole in a vacuum. One of the ways we have to test the validity of this assumption, and by doing so probe the emission mechanisms of pulsars, is by measuring the change of a pulsar's spin frequency and spin-down rate over time. Under the assumptions that the moment of inertia (I), the angle of misalignment between the magnetic and rotational axes (α), and the magnetic moment (m_0) are constant, we can rewrite Equation 1.6 as:

$$\dot{\nu} = -K\nu^n, \tag{1.9}$$

Here, all the constants have been combined into K, and we have generalized the exponent of ν from the three expected from magnetic dipole radiation to n, which we refer to as the braking index (e.g. Manchester & Taylor, 1977).

By integrating the above equation, we can also get an age estimate for a pulsar:

$$\tau_c = -\frac{\nu}{(n-1)\dot{\nu}}\left(1 - \left(\frac{\nu}{\dot{\nu}}\right)^{n-1}\right) \tag{1.10}$$

which is generally referred to as the characteristic age. If we make the assumption that the birth spin frequency is much higher than the current spin frequency, this simplifies to:

$$\tau_c = -\frac{\nu}{(n-1)\dot{\nu}}. \tag{1.11}$$

In the literature, it is common to make the further assumption that $n = 3$, and most characteristic ages are estimated as $\tau_c = -\nu/(2\dot{\nu})$. Indeed, these are the lines of constant age plotted in Figure 1.3.

In more realistic models of a pulsar and its magnetosphere, the braking index is predicted to always lie between 1.8 and 3 (Melatos, 1997). Values less than this can be obtained by relaxing the various assumptions of the model – e.g. allowing magnetic field evolution (Blandford & Romani, 1988) or a varying angle between the spin and magnetic poles (Lyne et al., 2013).

As well, different values of n are expected for different energy loss mechanisms. If a pulsar is losing energy through the emission of a particle wind, we would expect n to have a value of one (Harding et al., 1999). If a pulsar's dominant energy loss mechanism is the loss of energy due to gravitational radiation from having a quadrupole moment in its mass, n should be five (Blandford & Romani, 1988).

Observationally, the braking index is measured by means of observing a gradual change in $\dot{\nu}$, the frequency derivative. We can see this by taking the time derivative of Equation 1.9 which gives us the following fundamental equation which contains only the braking index and observable quantities:

$$n = \frac{\ddot{\nu}\nu}{\dot{\nu}^2} \tag{1.12}$$

where $\ddot{\nu}$ is the second-derivative of the spin frequency.

Measuring braking indices for pulsars has proven to be difficult, as young pulsars typically exhibit large amounts of timing noise which can contaminate measurements of $\ddot{\nu}$ (e.g. Hobbs et al., 2010) (see §2.2 for details on timing noise.). A measurement of n can be made only for the youngest pulsars for which $\ddot{\nu}$ is large enough to detect on human time scales. As such, only eight pulsars of the ~ 2400 known have measured braking indices, with values ranging 0.9 ± 0.2 to 2.839 ± 0.001 (Lyne et al., 2015, and references therein)[v].

X-RAY DETECTED ISOLATED PULSARS

Of the ~ 2500 known isolated pulsars, only ~ 100 are detected as X-ray sources (see Kaspi et al., 2006; Olausen & Kaspi, 2014). The bulk of these are energetic RPPs – with the Crab pulsar being the best-known example. Much of this emission is non-thermal, originating in the pulsar magnetosphere (§ 1.2.2). Several classes of pulsars have also been detected as thermal X-ray emitters, which will now be discussed.

Central compact objects (CCOs) are a class of neutron stars found as hot, X-ray sources in supernova remnants. There are only 8 members of this class (Gotthelf et al., 2013). In cases where a periodicity has been found, the CCOs spin at periods of $\sim 0.1 - 0.5$ s and appear to have very low magnetic fields of $\sim 10^{10} - 10^{11}$ G. The most famous of these objects, however, the CCO in the Cas A supernova remnant has

---

[v] During the preparation of this document, new braking indices have been measured. A discussion of the significance of these results can be found in §9.1.

no detected period (Halpern & Gotthelf, 2010). As they are in supernova remnants, they can be independently dated, however for the CCOs where a period and period derivative have been measured, their implied τ_c is orders of magnitude larger than the supernova remnant age, which suggests they may have been born with spin periods close to their current periods (Klochkov et al., 2016; Gotthelf et al., 2013).

X-ray dim isolated neutron stars (XDINs) are a group of seven nearby (distances $\lessapprox 400\,\mathrm{pc}$)[vi] neutron stars with long spin periods ($\sim 3-11\,\mathrm{s}$) with only soft, modified thermal X-ray emission and no detected radio emission. They tend to have higher magnetic fields than the rotation-powered pulsars ($\sim 10^{13}\,\mathrm{G}$), and characteristic ages of millions of years. The XDINS are marked in blue in Figure 1.3. For a review of XDINs, see e.g. Turolla (2009) and van Kerkwijk & Kaplan (2007). They are more luminous in the X-ray band than RPPs of comparable ages, which may be due to heating from magnetic field decay (Pons et al., 2007; Kaplan & van Kerkwijk, 2009). It has been theorized that these objects may be the evolutionary descendants of magnetars (see § 1.5) (see e.g. Mereghetti et al., 2015).

High magnetic field RPPs, RPPS with magnetic fields higher than $\sim 10^{13}\,\mathrm{G}$, are more often detected as X-ray sources than their lower-B cousins. This is due to the observation that High-B RPPs have temperatures higher than comparably aged other RPPs (Zhu et al., 2011; Olausen et al., 2013), making them detectable as thermal X-ray sources. In the magnetothermal evolution model, these are heated by magnetic field decay (Pons et al., 2007; Pons & Perna, 2011).

[vi] This class of objects can only be seen if they are nearby due to their very soft X-ray spectrum;see Chapter 3.

Magnetars

In a tiny fraction ($\sim$ 20) of the isolated pulsar population, the loss of rotational energy is not sufficient to provide the observed energy output & extreme behaviour including orders of magnitude X-ray band flux increases, and the emission of short ($\sim 100\,$ms) bursts. These *magnetars* are characterized by their long ($\sim 2-12$ s) spin periods, extremely high spin-inferred magnetic fields ($\sim 10^{14}$ G), and X-ray luminosities which can greatly exceed the energy available from spin-down alone. These pulsars originally were classified under two different observational classes: Soft Gamma-ray Repeaters and the Anomalous X-ray Pulsars.

Soft Gamma-ray Repeaters (SGRs) get their name, unsurprisingly, from the repeated emission of soft gamma ray bursts (e.g. Golenetskij et al., 1979; Mazets et al., 1979a; Golenetskii et al., 1984). More details of these bursts can be found in §1.5.1. Their repetition and their periodicity made them stand out (Mazets et al., 1979b) as clearly distinct events from what today are known as gamma-ray bursts (GRBs), which originate from cosmological distances (e.g. Gehrels & Mészáros, 2012).

Anomalous X-ray Pulsars (AXPs) were identified as a group of stable X-ray emitting pulsars with strangely similar periods between $\sim 5.4-8.7\,$s (Mereghetti & Stella, 1995). They also seemed to spin much more stably than accreting X-ray pulsars, and spin-down stably. They were dubbed anomalous in that their X-ray luminosity exceeded their spin-down luminosity (Mereghetti et al., 1998). This meant that there was another power source in play in these pulsars and, as non-detections of Doppler shifts in their spin frequencies made the limits on possible companions more stringent, it seemed unlikely that accretion could be the answer (Mereghetti et al., 1998).

As the observed properties of these two source classes now substantially overlap and, as we shall see in the next section, are believed to have the same physical origins, these sources are collectively called magnetars.

Magnetar Radiative Behaviour

In addition to often having anomalously high luminosities, magnetars also undergo radiative events.

Transient Behaviour

Magnetar radiative events can be roughly divided into three categories: giant flares, bursts, and outbursts.

Giant flares are the most extreme radiative events seen in magnetars – having fluences of $\sim 10^{44} - 10^{46}$ ergs in soft gamma-rays. They are characterized by a ~ 100 ms long flash, which contains approximately half of the energy budget of the flare, followed by a minutes-long decay which is strongly modulated at the rotation period of the pulsar. Giant flares are incredibly rare events; we have only seen three giant flares since the dawn of X-ray astronomy. The first giant flare occurred on 5 March 1979 from SGR 0525−66 (Mazets et al., 1979b). The second occurred on 27 August 1998 from SGR 1900+14 (Hurley et al., 1999). The third, and most recent giant flare occurred on 27 December, 2004 from SGR 1806−20 (Palmer et al., 2005).

Soft-gamma-ray/hard X-ray bursts are the most common type of magnetar radiative behaviour. These are typically ~ 100 ms long, following roughly a log-normal distribution around this duration (e.g. Collazzi et al., 2015). These bursts have fluences of between $\sim 10^{36} - 10^{40}$ ergs. These bursts tend to have a higher average energy than the persistent magnetar emission, with their spectra often modelled with a blackbody temperature of a few keV, compared with the $\sim 0.5\,\mathrm{keV}$ temperature of the persistent emission. While sometimes these bursts occur as one-off events, they have a tendency to be clustered; see for example Chapter 7.

Outbursts are increases in the X-ray flux by anywhere between a factor of a few, to a factor of thousands. They are characterized by a long-term flux increase which decays on a time scale of months to years, and are usually heralded by one or more magnetar bursts. Magnetars in outburst tend to follow a flux-hardness correlation: the brighter they are, the higher the average energy of an emitted photon (e.g. Zhu et al., 2008; Tam et al., 2008; Scholz & Kaspi, 2011). See Chapter 6 for an example magnetar outburst, and see Rea & Esposito (2011) for an observational review of magnetars in outburst. Many of the magnetars known today were discovered in outburst, and these are often referred to as 'transient' magnetars as, with current X-ray observatories, they are only detectable is a reasonable integration time when in outburst.

Sources which display this kind of behaviour are now generally collectively called magnetars. Magnetars appear to have the highest spin-down-inferred dipolar surface magnetic fields of the neutron-star population, with magnetic fields of order $10^{14} - 10^{15}$ G, and as such appear in the top right hand corner of the P–$\dot{\mathrm{P}}$ diagram, Figure 1.3. Recently, however magnetars with more typical inferred dipole magnetic fields have been found (e.g. Rea et al., 2013; Scholz et al., 2014b). There are currently 23 confirmed magnetars; an up-to-date list of both confirmed and candidate magnetars is maintained in the McGill Magnetar Catalogue[vii] (Olausen & Kaspi, 2014).

[vii] `www.physics.mcgill.ca/~pulsar/magnetar/main.html`

Persistent Emission

Compared to rotation-powered pulsars of comparable ages, the magnetars tend to be hot (e.g. Olausen & Kaspi, 2014). In the soft X-ray band ($0.5 - 10\,\mathrm{keV}$) the emission is mainly thermal, being phenomenologically modelled as blackbody emission with a temperature of $kT \simeq 0.5\,\mathrm{keV}$ and/or a relatively soft power law ($\Gamma \simeq 2 - 4$). This is generally thought to be due to thermal surface emission, modified by resonant scattering in the magnetosphere (Thompson et al., 2002).

Magnetars can also emit as much, or even more, energy in the hard X-ray band ($10{-} \sim 100\,\mathrm{keV}$) as they do in the soft X-ray band. (e.g. An et al., 2013). This emission is thought to be due to the rapid deceleration of an electron positron outflow along a magnetar's magnetic field lines (Beloborodov & Thompson, 2007; Beloborodov, 2013; Hascoët et al., 2014). This emission is distinct from the typical magnetospheric emission from RPPs.

The Magnetar Model

The magnetar model (Duncan & Thompson, 1992; Thompson & Duncan, 1995, 1996) was developed to explain the behaviours described above of what at the time were thought as of two classes of sources – the Anomalous X-ray Pulsars and the Soft Gamma-ray Repeaters. In this model, a magnetar is born with rapid rotation which drives a dynamo to create a magnetic field of $B \sim 10^{15}\,\mathrm{G}$. This high magnetic field both provides an enormous store of magnetic energy, and explains why all the known SGRs and AXPs are slowly rotating compared to pulsars of comparable ages. In this model, magnetars are powered by the decay of their magnetic fields which heats the stellar interior and causes internal stresses on the stellar crust which occasionally yields. This model predicted that, since AXPs and SGRs were different manifestations of the same class, that AXPs should show bursts, like the SGRs.

In 2002, bursts were indeed detected from the AXP 1E 1048.1−5937, helping to unify these two classes under the magnetar model (Gavriil et al., 2002). That same year, the AXP 1E 2259+586 underwent a classic SGR-like outburst (Kaspi et al., 2003). Now, nearly all of the classic AXPs have exhibited bursts and outbursts (Dib & Kaspi, 2014)[viii]. For this reason, throughout this document I use the term magnetar rather than AXP or SGR to refer to magnetically powered neutron stars.

In the initial magnetar model, the dividing line between a regular pulsar and a magnetar occurred when the magnetic field of the pulsar exceeded B_Q, the magnetic field strength at which the first electron Landau level matches the electron rest-mass (Thompson & Duncan, 1995).

$$B_Q = \frac{m_e^2 c^3}{e\hbar} = 4.4 \times 10^{13}\, G. \tag{1.13}$$

However, many more recent observations would suggest that this is not a necessary condition. For example, the discovery of magnetars with low magnetic fields, such as SGR 0418+572 with a magnetic field of only 6×10^{12} G, (Rea et al., 2010, 2013), comparable to that of an average pulsar, and Swift J1822.3−1606, with a magnetic field of 1.35×10^{13} G (Scholz et al., 2014b) challenge the original magnetar definition of having a magnetic field greater than B_Q.

As well, magnetar-like activity has been seen from high-B rotation-powered pulsars. The earliest indication of this came in 2006 from a young pulsar, PSR J1846−0258. It emitted several magnetar-like X-ray bursts and increased its X-ray luminosity by

---

[viii] As of 21 February, with the detection of a burst from 1 RXS J170849.0−400910 all the long-term monitored AXPs have displayed magnetar-like bursts (Archibald et al., 2017a).

a factor of ~ 5, behaving remarkably similar to a magnetar in outburst (Gavriil et al., 2008). PSR J1846−0258 has one of the highest magnetic fields of rotation-powered pulsars and, both before and after the outburst, manifested itself as a typical rotation-powered pulsar (Archibald et al., 2015b). As we shall see in Chapter 8, now another high-B RPP too has been observed to have magnetar-like properties.

DOCUMENTATION

The principle goal of this thesis is exploring the behaviours and energetics of isolated neutron stars. With that goal in mind the proceeding chapters are laid out here.

In Chapter 2, the spin behaviour of pulsars is discussed, and pulsar timing techniques will be introduced. In Chapter 3 I describe the basics of X-ray astronomy, and the telescopes used in this work. Chapters 4 and 5 present new results measuring braking indices through the use of these timing techniques. Chapters 6 and 7 present results from long-term monitoring campaigns of magnetars as they go through outbursts. Chapter 8 presents a magnetar-like outburst from a high magnetic field RPP. Finally, in Chapter 9 I will discuss the implication of these results, and some other relevant recent results in pulsar science.

I saw thy pulse's maddening play, Wild send thee Pleasure's devious way, Misled by Fancy's meteor-ray, By passion driven;

Robert Burns

2

Pulsar Spin Behaviour & Timing Analysis Techniques

Owing largely to their enormous moments of inertia, $\sim 10^{45}\,\mathrm{g\,cm^2}$, pulsars generally rotate incredibly stably. They, however, do not always spin down as perfectly as we might like. In this chapter I will discuss deviations from a simple spin-down, namely the phenomena of glitches and timing noise, and then review the timing techniques used in this thesis.

Pulsars sometimes exhibit as yet unresolved changes in their rotation frequency in which they suddenly appear to start spinning faster. These sudden changes in rotation frequency are known as glitches. While some glitches are characterized by a simple step in spin frequency, many glitches have been seen to be accompanied by changes in $\dot{\nu}$, or to decay by some portion of the initial jump in an exponential manner (Espinoza et al., 2011). Observationally, glitches can then be described as:

$$\nu(t) = \nu_0(t) + \Delta\nu + \Delta\dot{\nu}(t - t_g) + \Delta\nu_d e^{-(t-t_g)/\tau_d} \tag{2.1}$$

where ν_0 is the expected frequency given the pre-glitch timing behaviour, $\Delta\nu$ and $\Delta\dot{\nu}$ are permanent changes to the spin parameters occurring at a time t_g, and $\Delta\nu_d$ is a change in spin frequency which decays with a characteristic time scale τ_d. A schematic representation of pulsar glitches is shown in Figure 2.1.

Glitches were discovered shortly after pulsars themselves, with the first reported glitches occurring in the Vela pulsar (B0833−45) (Radhakrishnan & Manchester, 1969; Reichley & Downs, 1969). The time scale over which a glitch occurs has not been resolved. The most constraining observation on the suddenness of glitches coming from observations of the Vela pulsar where during a glitch in the year 2000, the change in rotation frequency is limited to occur during a period of less than 40 s (Dodson et al., 2002). As pulsars are generally not continuously observed, we cannot resolve the time scale in which a glitch occurs, and so we model glitches as instantaneous changes in spin frequencies. As of now, more than 300 glitches have been seen in over 100 pulsars (Espinoza et al., 2011; Yu et al., 2013) with the glitch sizes,

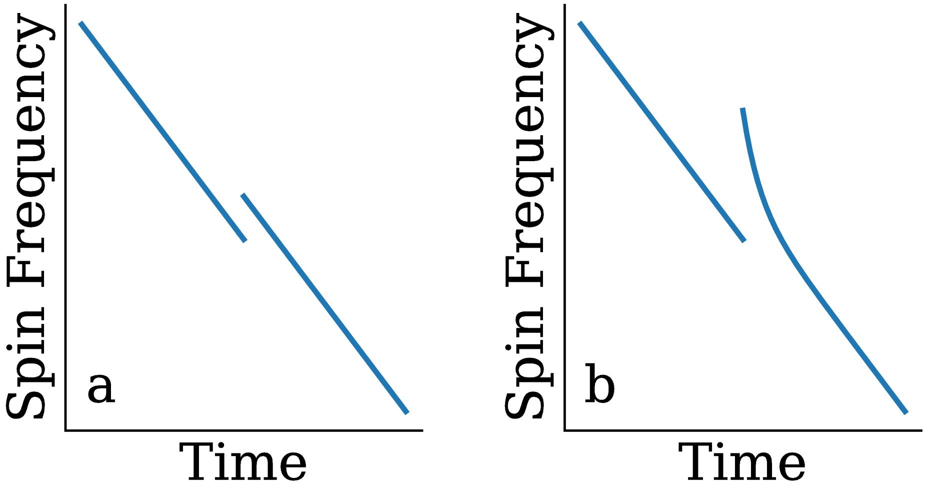

Figure 2.1 In both panels, the spin frequency of a pulsar is plotted against time. In panel **a**, the results of a typical step in spin frequency is shown. In panel **b**, a glitch with both a permanent step component, and an exponential recovery is shown.

$\Delta\nu/\nu$, ranging from 10^{-11} to 10^{-5}.

As glitches in RPPs generally have no detectable change in their pulsed emission or pulse shape at the time of a glitch, glitches are believed to have an origin inside the neutron star, and are used as a probe of the pulsar interior (see e.g. Link et al., 1992; Ho et al., 2015).

The first model put forth to explain the observed glitches in pulsars was the starquake model. In this model, neutron stars originally have an oblateness due to their spin. As they slow down, the crystal-like lattice of the neutron star crust gradually builds up a strain. Eventually, this strain reaches a breaking point, and a star quake (analogous to an earth quake) occurs which slightly rearranges the mass of the neutron star to become less oblate, and thus changes its moment of inertia, leading to the change in spin frequency (Ruderman, 1969).

A second model for pulsar glitches involves the exchange of angular momentum between various components of a neutron star. As discussed in § 1.2.1, the inner crust of a neutron star contains two major components: a lattice of neutron rich nuclei, and a sea of superfluidic neutrons (Anderson & Itoh, 1975). The existence of this superfluid component is suggested by the days to months long recoveries following glitches, as normal fluids and solids would recover on an orders of magnitude faster rate of 10^{-17} s (Baym et al., 1969). In a superfluid, angular momentum is quantized into vortices. These vortices can become pinned to defects in the lattice, effectively freezing the amount of angular momentum stored in the superfluid. As the rest of the star spins down, the superfluid cannot, and a differential rotation forms between the two components. In this model, a glitch occurs when when vortices become unpinned en masse from the crustal lattice. This allows the vortices to rearrange, and in this process, angular momentum is transferred from this superfluid to the crustal lattice. As the observed pulses from a pulsar originate from regions tied to the crust, the observed pulse period will suddenly increase (Pines & Alpar, 1985). For a recent review of pulsar glitch theory, see Haskell & Melatos (2015).

Magnetars, like rotation-powered pulsars, experience sudden changes in their spin-frequency known as glitches (see e.g. Kaspi et al., 2000; Dib et al., 2008). While similar in observed size distribution to glitches in RPPs, magnetar glitches are unique in that they are sometimes accompanied by radiative changes including short soft-γ-ray bursts, pulse profile changes, and long-term (months to years) X-ray flux enhancements (see Dib & Kaspi, 2014, for a review). In a study of 22 glitches and candidate glitches in 5 magnetars, only 6 had accompanying radiative changes including a flux increase, a pulse profile change, or the detection of magnetar-like bursts (Dib & Kaspi, 2014). As will be further discussed in Chapter 7, magnetars have also been seen to have a class of net spin-down glitches that are not seen from the bulk of the pulsar population.

TIMING NOISE

Timing noise refers to unexplained low-frequency modulations found in the residual phase wander unaccounted for by a pulsar's spin frequency and frequency derivative (Arzoumanian et al., 1994). Timing noise in radio pulsars has been observed to be spectrally 'red', that is, having most power at low frequencies (i.e. months to years) (Arzoumanian et al., 1994).

The power spectral density (PSD) of timing noise is often modelled as

$$\Phi_{TN}(f) = A\left(1 + \frac{f^2}{f_c^2}\right)^{-q/2}, \tag{2.2}$$

where A is the spectral density amplitude, f_c the corner frequency, and q the power-law index (Lasky et al., 2015). A q of 0 represents a white noise power spectrum, whereas indices of 2, 4, and 6 represent random walks in pulse arrival phase, the pulsar spin frequency, and frequency derivative, respectively. This framework was first put forth to explain the timing noise observed in the Crab pulsar (Boynton et al., 1972). Observationally, however, the PSD of timing noise does not conform to any of these exact values (Cordes & Downs, 1985).

The strength of the timing noise in a pulsar is often quantified by the Δ_8 parameter:

$$\Delta_8 = \log\left(\frac{1}{6\nu}|\ddot{\nu}|t_8^3\right) \tag{2.3}$$

where t_8 is a reference time interval of 10^8 s (Arzoumanian et al., 1994). This amounts to quantifying the number of pulsar phase turns not accounted for by ν and $\dot{\nu}$ alone. Using this quantification, the amount of timing noise is highly correlated with the spin-down rate of a pulsar, with a best-fit of $\Delta_8 = 5.1 - 0.5\log(\dot{\nu}/\nu^2)$ (Hobbs et al., 2010). As well, timing noise is correlated with a pulsar's characteristic age, with younger pulsars displaying more timing noise (Hobbs et al., 2010).

The physical origin for timing noise is unknown. A possible origin of timing noise is superfluid turbulence (Melatos & Link, 2014). In this model, the neutron superfluid component of the neutron star, introduced in § 1.2.1, is turbulent. This turbulence causes a random pinning and unpinning of vortices, transferring angular momentum between the superfluid and the solid components of the crust.

Timing noise has also been proposed to be caused by residuals of unresolved glitches. However, at least for the case of the Crab pulsar, it has been shown that pulsar glitches have a minimum size (Espinoza et al., 2014) which is an argument against this origin.

Another possible origin for at least some of the observed timing noise is a mode-switching magnetosphere. In some pulsars we can observe at least two distinct emission modes, and these modes have been observed to have different spin-down rates (Kramer et al., 2006; Lyne et al., 2010). If this mode switching is unresolved in some pulsars, spending time in two different spin-down modes would manifest itself similarly to timing noise.

Pulsars with high magnetic fields, above $\sim 10^{12.5}$ G, display a higher level of timing noise than lower magnetic field pulsars (Tsang & Gourgouliatos, 2013). It has been proposed that this could be do to to variations in the moment of inertia of the pulsar's magnetosphere (Tsang & Gourgouliatos, 2013). Indeed, as we shall see in Chapter 6, in some magnetars, the spin-down rate can change by order unity which is most likely indicative of changes in the external magnetic field configuration, as discussed in Chapters 6 and 7.

PULSAR TIMING

In order to find and characterize the spin behaviour of a pulsar well enough to find glitches and see timing noise, a technique known as phase-coherent timing in used. Phase-coherent timing is the keystone technique in pulsar science. This technique accounts for the exquisite precision that allows for tests of general relativity (e.g. Lyne et al., 2004), the future detection of nanoHertz frequency gravitational waves (e.g. Arzoumanian et al., 2016), the first detection of extra-solar planets (Wolszczan & Frail, 1992), as well as many other science results including the detection of pulsar glitches described above. The idea behind phase-coherent timing is straight forward – one simply has to account for every single rotation of a pulsar between the first and final observation. In order to do so, one must take into account each source of time delay which may occur between the emission of a photon from the pulsar, to that photon's measurement at an observatory. These time delays include the geometric variation in the distance from the Earth to the pulsar as the Earth orbits the Sun, and as our telescopes orbit the Earth. In this work, we use `barycorr`, part of the standard X-ray analysis software `HEASOFT`[i] to accomplish this.

Once we have corrected the photon arrival times to the Solar System barycentre, we can determine the time of the emission of that photon from the pulsar itself, and begin to time the pulsar. As this thesis deals with timing in the X-ray and Gamma-ray bands, I shall talk about the arrival time of individual photons. For radio data, the techniques are similar, but the signal arrives continuously instead of in discrete

---

[i] Available from http://heasarc.nasa.gov/lheasoft/

photons. In either case, we wish to know the relative rotational phase of the pulsar at the time of that photons emission. For isolated pulsars, under the assumption that the pulse phase varies smoothly, the phase, ϕ is calculated via a Taylor expansion:

$$\phi(t) = \phi_0 + \nu_0(t - t_0) + \frac{1}{2}\dot{\nu}_0(t - t_0)^2 + \frac{1}{6}\ddot{\nu}_0(t - t_0)^3 + \cdots \qquad (2.4)$$

where ν_0, $\dot{\nu}_0$ and $\ddot{\nu}_0$ are the spin parameters at the epoch t_0, and ϕ_0 the phase at t_0.

At this stage, we have a list of photons tagged with the pulsar's predicted phase. As described in the following sections, these individual photon phases are used to eventually measure the average pulse time-of-arrival (TOA) for a given observation. Further effects must be taken into account when timing binary pulsars but these are not discussed in this thesis.

Maximum Likelihood Phase Alignment

The timing technique described below, as well as the standard cross-correlation technique typically used in timing radio pulsars, rely on the observation that a pulsar's integrated pulse profile is stable over time, and that this emission is tied exactly to the rotation of the neutron star itself. We need this to be true as, in the vast majority of cases, we do not observe enough photons during one pulsar rotation in order to detect the pulsed signal. In order to detect a pulsed signal, we then must 'fold' a pulsar, i.e. take $\phi \bmod 1$, over hundreds to millions of individual rotations. When this is done, the pulse profile will emerge from the noise, with the signal increasing as the square root of the observing time, as we are dominated by photon counting statistics.

For the maximum likelihood technique, we first create a normalized high signal-to-noise pulse profile template by fitting the folded phases from many observations to a Fourier series, and determining the optimal number of harmonics using the H-test (de Jager et al., 1989; Archibald et al., 2015a). This template is then normalized to become a probability distribution function for that pulsar's emission. A sample template-profile is found in Figure 2.2. Note that the counts are binned for visualization purposes only; the template is fit to unbinned photon phases.

After the creation of a normalized pulse profile template, $I(\phi)$, the phase offset of an individual observation can be determined. In this work, this is done using the maximum likelihood method, first proposed in Livingstone et al. (2009). This method avoids the loss of information caused by binning a profile. To do this, the rotational phase (ϕ_i) of every individual photon in the observation is calculated, assuming the best prior timing model. For each possible offset $0 \leq \delta < 1$, the relative probability of that offset being the optimal offset is given by

$$P(\delta) = \prod_{i=1}^{N} I((\phi_i - \delta) \mod 1). \tag{2.5}$$

Uncertainties on the optimal phase are determined by integrating this probability curve. A sample profile, folded individual observation, and phase-alignment posterior probability distribution are found in Figure 2.2. Again, the counts are binned for visualization purposes only. This phase offset is then converted to an average pulse time-of-arrival (TOA) by:

$$TOA = t_0 + \delta_{best} \nu(t_0)^{-1} \tag{2.6}$$

where t_0 is the reference epoch used to fold the data, usually the closest integer pulse turn to the centre of the observation and δ_{best} is the offset with maximum probability.

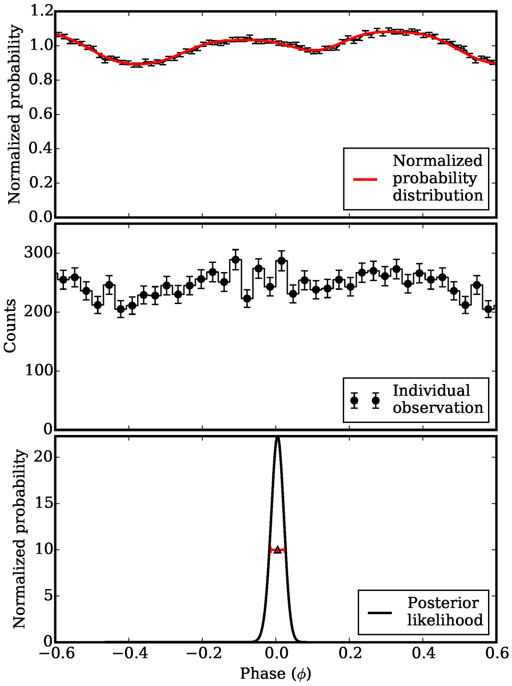

Figure 2.2 The top panel shows the standard template profile for 4U 0142+61, in the 0.7–10 keV range. The middle panel shows the folded profile for a single observation in the same energy range. The bottom panel shows the posterior likelihood distribution for the phase alignment of these two profiles, with the measured 68% confidence interval indicated by a red triangle.

INITIAL PERIOD FINDING & REFINEMENT

In the above description of pulsar timing we worked under the assumption that we already knew the pulsar spin parameters to an adequate precision. Here, adequate precision means knowing the spin parameters to better than the needed phase accuracy times $(T\nu)^{-1}$, where T is the length of the observation. If this criteria is not met, the pulse profile will be smeared out, leading to a decreased signal-to-noise ratio.

If the spin parameters are completely unknown, the case in searching a supernova remnant for a new pulsar, the spin frequency can be found by taking a fast Fourier transform of the observed time series[ii]. In the case where we know the approximate spin parameters, the case when starting to observe a pulsar after a long gap, or after a large suspected glitch, the period can be refined using the H-test (de Jager et al., 1989).

After we have the refined spin-parameters, we can make TOAs, and begin the phase coherent timing. To start a new phase-connected timing solution requires a series of closely spaced observations. Specifically, the gap between each successive observation is constrained by the condition that $(d\nu \times t) < 0.3$, where $d\nu$ is the current uncertainty on the spin frequency, and t the time between two observations. In other words, for each new observation, we need to be able to predict the pulse phase at the epoch of the new observation to better than ∼one third a rotation. If this condition is met, then we can count the exact number of pulsar rotations which occurred between our observations, and have established an unambiguous phase connected solution.

In this thesis, the establishment of phase connected solutions was done using the

---

[ii] For the case of pulsars in binaries, more complicated search techniques are needed; see e.g. Ransom et al. (2002).

`TEMPO2` software package (Hobbs et al., 2006). `TEMPO2` was developed by George Hobbs and Russell Edwards as part of the Parkes Pulsar Timing Array project (Hobbs et al., 2006). It was based on the original `TEMPO` [iii] software package written by J. H. Taylor, R.N. Manchester, D. J. Nice, and others. `TEMPO2` takes the spin parameters of a pulsar, as well as the measured TOAs as an input, and performs a weighted χ^2 minimization on the timing residuals to find the optimal spin parameters and uncertainties. Timing residuals are the difference between the phase of the measured TOAs and those predicted by a pulsar timing model, such as Equation 2.4. They are defined as:

$$R = (\phi_o - \phi_p) \text{modulo } 1 \tag{2.7}$$

where ϕ_o is the observed pulse phase, and ϕ_p the predicted pulse phase.

Errors in different timing parameters manifest themselves differently in residual space. For example a change in ν will result in a linear trend, and a change in $\dot{\nu}$ will result in a parabolic trend.

[iii] http://www.atnf.csiro.au/people/pulsar/tempo/

But yet the light that led astray Was light from Heaven.

Robert Burns

3

X-ray Astronomy

X-rays are photons with energies of 0.1–500 keV. In the X-ray regime, the light we observe comes from objects with a temperature greater than 10^6 K, or from the acceleration of relativistic particles in strong magnetic or electric fields. As the Earth's atmosphere is optically thick to X-rays, astrophysical X-rays can only be observed by going above the atmosphere, either via sounding rocket, stratospheric balloon, or by placing the telescope in space on a satellite.

Even above the atmosphere, softer X-rays (those below $\sim$ 2 keV) are vulnerable to photoelectric absorption. Photoelectric absorption is an effect caused by atomic absorptions in the K and L electron shells. The amount of absorption depends on the relative abundances of heavy elements, which change the cross section of interaction (see e.g. Verner et al., 1996), as well as the column depth between the emission of an X-ray photon and our telescope. We quantify this effect into an equivalent neutral hydrogen column density, denoted N_H (e.g. Wilms et al., 2000). The total absorption can be calculated by $F_o = F_e e^{-N_H \sigma(E)}$, where $\sigma(E)$ is the energy dependent cross section of interaction, F_o is the source flux observed, and F_e is the source flux before absorption. As this effect is highly energy dependent, and preferentially absorbs softer (lower energy) X-ray photons, photoelectric absorption makes it more difficult to detect soft sources which are at a higher column depth, and makes X-ray sources appear harder (i.e. having a higher average energy).

Spectrum files are created which contain the number of photons which arrived in an energy channel during the observation. To fit X-ray spectra, spectral models are then fit observed photon energy distribution, taking into account the exposure times, and effective areas of the source and background regions, as well as the photoelectric absorption discussed above.

All spectral fitting in this work was done using the `xspec` software package (Arnaud, 1996). In `xspec`, theoretical models (e.g. blackbody radiation) are convolved with the instrument response files, and spectral parameters are adjusted to optimize a goodness of fit parameter, via a minimization of χ^2, or the Cash statistic (Cash, 1979).

TELESCOPES USED IN THIS WORK

In this section, I will introduce the X-ray (and one gamma-ray) telescopes used to collect data in this work, as well as briefly explain the principle types of detectors used therein.

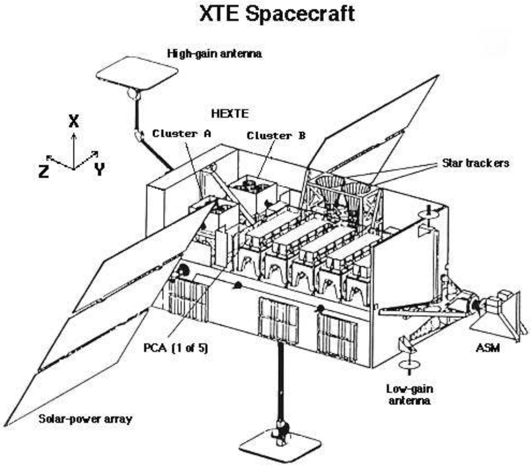

Figure 3.1 A schematic of *RXTE*. Image from the *RXTE* image gallery, `heasarc.gsfc.nasa.gov/docs/xte/xte_images.html`.

The *Rossi X-ray Timing Explorer*

The *Rossi X-ray Timing Explorer (RXTE)* was launched in December of 1995 and was in operation until January of 2012. A schematic diagram of *RXTE* can be seen in Figure 3.1. The main science instrument, and the one used in this work, was the Proportional Counter Array (PCA), with 6500 cm^2 of collecting area split between five proportional counter units (PCUs), sensitive from 2–60 keV (Jahoda et al., 1996). *RXTE* had two other science instruments - an All Sky monitor (ASM), and the High Energy X-ray Timing Explorer (HEXTE), but as they are not used in this work, they will not be further discussed. The PCA achieves this large collecting area at the expense of having no spacial resolution, being a collimated rather than a focusing instrument, giving it $\sim 1^\circ$ field of view with no resolving elements.

Proportional counters are chambers of inert gases, with electrodes throughout. When an X-ray enters the chamber, the X-ray will ionize a molecule of the inert gas.

The electron freed in this interaction will possess kinetic energy, proportional to the energy of the incident X-ray photon, and can ionize then a number of other gas molecules in the chamber, again proportional to the energy of the incident X-ray photon. These electrons are then attracted to the charged electrodes in the detector, which results in a current that can be read off, which will give the approximate energy on the original X-ray photon. *RXTE* was uniquely capable of time domain science having microsecond time resolution. Science enabled by *RXTE* will be presented in Chapters 4 and 6.

THE *Swift* GAMMA-RAY BURST MISSION

The *Swift* Gamma-Ray Burst Mission (Burrows et al., 2005) is the principal observatory used in this work. As the name implies the principal purpose of the *Swift* mission is to be able to respond quickly to the transient X-ray sky, and in particular to study gamma-ray Bursts (GRBs) and their afterglows. The *Swift* mission was launched into a low-Earth orbit on the 20^{th} November 2004, and is still in operation.

The *Swift* mission consists of three instruments: the Burst Alert Telescope (BAT), the Ultra Violet Optical Telescope (UVOT), and the X-Ray Telescope (XRT). A rendering of *Swift* can be seen in Figure 3.2a.

BAT (Barthelmy et al., 2005) is a non-focusing hard X-ray telescope, sensitive to photons having energies between 15-150 keV. The BAT has a wide field of view, 1.4 sr, and for a bright burst, can localize a source to a 1–4 arcminutes error circle. The BAT uses a coded aperture mask, whereby a source at any point in the field of view of the telescope will project a unique pattern on the detectors. When a burst is detected by the BAT, *Swift* is designed to slew to the burst position within 75 s. It has

(a) **(b)**

Figure 3.2 (a) A schematic of the three co-aligned instruments on the *Swift* satellite: the XRT, BAT, and UVOT.
(b)The *Swift* XRT mirrors. Note the individual nested layers. Both images are from the *Swift* mission website (`swift.gsfc.nasa.gov`).

proved an invaluable resource for detecting and following up bursts from other astrophysical sources; see e.g Chapter 7 and Chapter 8.

The *Swift* X-Ray Telescope (XRT) (Burrows et al., 2005) is sensitive in the 0.2 - 10 keV range with an effective area of 110 cm^2 at 1.5 keV. Like all the focusing X-ray telescopes used in this work, it uses a Wolter-I telescope, in this case one with a 3.5-m focal length with 12 nested layers.

In the Wolter I mirror design, each layer of the mirror contains two focusing elements; a paraboloid followed by a hyperboloid. This design is used as unlike visible light, X-rays can only be reflected at small angles, approximately < 1 degree relative to the reflection surface for X-rays between 0.1-10 keV. Each of these layers, however, can only focus light from a small area, the cross section of the parabolic mirror when viewed from above, so multiple layers are nested to order to increase the effective area. An image of the XRT mirrors can be seen in Figure 3.2b.

The XRT has a field of view of 23.6 arcminute by 23.6 arcminute with angular resolution of 18 arcseconds. This field of view was designed, in part, to cover the error circle of a BAT detected burst in order to better localize GRB afterglows.

The XRT detector is a 600 by 600 pixel *XMM-Newton* EPIC-MOS CCD22 detector, a Charge-Coupled Device (CCD) detector with an effective area at 1.5 keV of $\sim$110 cm^2 (Burrows et al., 2005).

CCDs are solid state semiconductors devices. Inside the device a matrix of potential wells are set up to divide the CCD into pixels. These wells are moved to transfer the electrons to read off the CCD, after a fixed exposure time. When an X-ray photons hits one of these pixels, it frees electrons from the semiconductor, proportional to the energy of the X-ray ($\sim$ 1 electron per 3 eV of energy) (Tsunemi et al., 2001). One downside of CCDs is that they experience pile-up when exposed to bright sources.[i] Pileup occurs when more than one photon reach a pixel during the same read-out time. This leads to the apparent detection of one photon with high energy, instead of two lower energy photons, leading to inaccurate flux and spectral measurements.

Initially, the XRT could operate in four modes: image mode, photon counting mode, windowed timing mode, and photodiode mode. Image mode is designed for fast localization of GRBs. It produces an image of the sky, with no spectral information. This mode is principally used to promptly refine the position of a BAT detected GRB. Photon counting mode (PC) has the best spectral, and spatial information of all operational modes available to the XRT. This optimal spectral and spatial resolution is obtained by reading off each pixel of the CCD individually, at the cost of time resolution. It has time resolution of 2.5 s, and is useful for sources dimmer than $\sim$ 1 mCrab,

---

[i] In this case 'bright' means any source that has a count rate such that two photons will reach the detector in a readout time.

as sources brighter than this will lead to pile-up.

Windowed timing mode (WT) collapses the read-out of the CCD into one dimension, giving better time resolution than PC mode, 1.76 ms, at the cost of a dimension of spatial information, and slight loss of spectral information. As much of this thesis deals with the timing of pulsars, the vast majority of data analysed in this work was taken in WT mode.

Photodiode mode was optimized for time resolution with 0.14 ms, at the cost of all spatial resolution, as the entire CCD is read off at once, reacting as a single pixel detector, and losing much of the spectral information. Photodiode mode was disabled shortly after launch when *Swift* was damaged by a micrometeorite on the 27^{th} of May, 2005.

The UVOT (Roming et al., 2005) is designed to see photons with wavelengths between 170-600 nm. It has a limiting sensitivity of 24^{th} magnitude in 1 ks. It can achieve a positional accuracy of 0.3 arcseconds.

Science enabled by *Swift* will be presented in Chapters 4, 6, 7, and 8.

NuSTAR

NuSTAR, the *Nuclear Spectroscopic Telescope Array* is the first focusing telescope in the hard X-ray band, $3-78.4$ keV (Harrison et al., 2013). *NuSTAR* has two coaligned Wolter I mirrors with 133 shells, and a focal length of 10 m. Due to this focal length, the mirrors are separated from the focal plane by an extended mast. These twin telescopes focus to two identical focal plane modules, known as FPMA and FPMB. *NuSTAR* has a field-of-view of 10 arcminute by 10 arcminute. An artist's impression of *NuSTAR* is shown in Figure 3.3.

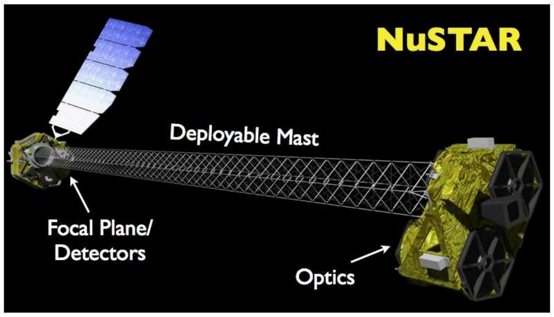

Figure 3.3 An artist's impression of *NuSTAR*. Image from `heasarc.gsfc.nasa.gov/docs/nustar/`.

NuSTAR's detector design is unique among X-ray telescopes in that it does not use traditional CCD read-off techniques. Rather, each time a photon hits the detector, it is immediately read out, leading to a 2.5 ms processing time where no other photon can be registered on that focal plane module. This avoids the problem of pile-up, unless a source reaches a brightness of $\sim 10^5$ counts s^{-1} pixels^{-1}. This does, however, limit the throughput of the telescope, and this maximal countrate must be taken into account when looking at bright sources, especially if they vary on a similar time scale. *NuSTAR* is especially suited to observations of pulsars as it combines a temporal resolution of $2\,\mu s$, and the ability to focus with a point-spread function of $\sim 1'$. *NuSTAR* data are used for the work described in Chapter 5.

Chandra

The *Chandra* X-ray telescope (Weisskopf et al., 2000) has the highest angular resolution of any X-ray telescope to date, with a resolution of 0.5 arcsecond. *Chandra* was launched on 23^{rd} July 1999 by the Space Shuttle *Columbia* and further propelled into a elliptical orbit with an apogee of 140 000 km and a perigee of 10 000 km. Once again, it makes use of four nested Wolter I mirrors, with a diameter of 1.4 m and a focal length of 10 m. *Chandra* achieves its angular resolution at the cost of effective area by having precisely shaped, but heavy, glass mirrors. *Chandra* has two instruments that can be placed at the focal plane – the high-resolution camera (HRC) and the advanced CCD imaging spectrometer (ACIS).

The HRC is a microchannel plate detector which has the largest field of view (30 arcminutes by 30 arcminutes) of any other detector on *Chandra*. HRC also has the best spatial resolution of any X-ray detector at ~ 0.3 arcseconds, and higher time resolution (16 ms) in imaging mode than ACIS. However, HRC has much lower energy resolution than ACIS, with a resolution of $E/\Delta E \sim 1$.

ACIS, like *Swift* XRT, is a CCD-based detector. In total, ACIS consists of 10 CCDs – 4 in a two by two array which make up ACIS-I, and 6 in a one by six grid that compose ACIS-S. It has much higher energy resolution than the HRC with $E/\Delta E \sim 10$ and comparable spatial resolution ($\sim$ 1 arcseconds) and a smaller field of view at 16.9 by 16.9 arcminutes for an ACIS-I image. In a standard full imaging mode, the native time resolution is 3.2 s. ACIS can achieve a higher time resolution, and reduce pile-up for bright sources by operating in a windowed mode, with the highest time resolution (2.85 ms) being achieved in continuous clocking (CC) mode where, similar to the WT mode for *Swift*, a subset of the array is compressed into a one-dimensional image. *Chandra* also has transmission gratings for high-resolution X-ray spectroscopy. *Chandra* data are used for the work presented in Chapter 6.

XMM-Newton

The X-ray Multi-Mirror Mission (*XMM-Newton*) was launched into orbit on the 10^{th} of December, 1999 (Jansen et al., 2001). *XMM* has three co-aligned telescopes, each being made of 58 Wolter I mirrors with a focal length of 7.5 m.

XMM, in contrast to *Chandra*, uses many thin nested mirrors to maximize collecting area at the expense of angular resolution. So while it has an effective area of $\sim 2500\,\mathrm{cm}^2$ between the three detectors compared to *Chandra*'s $600 - 800$ depending on if ACIS or the HRC is used[ii], *XMM* has an angular resolution of $\sim\ 6$ arcseconds, large compared to *Chandra*'s ~ 0.5 arcseconds.

At the focal plane of the three telescopes of *XMM* are three detectors – two European Photon Imaging Camera (EPIC)-MOS imaging detectors (Turner et al., 2001), and one European Photon Imaging Camera (EPIC) pn-CCD camera (PN) (Strüder et al., 2001). Both MOS and PN are CCD detectors the PN being composed of 12 individual CCDs, and each MOS being 6 CCDs. Again, like XRT and ACIS, *XMM*'s detectors have a variety of 'windowed' read-out modes. The full-frame read out time is 4.6 s and 2.6 s for the PN and MOS cameras respectively, with the best timing resolution being in PN's burst mode of $7\,\mu$s, at the expense of all spatial resolution.

Half of the light that enters the telescopes which focus on the MOS chips is diverted to a reflection grating spectrometer (den Herder et al., 2001), which can be used for high resolution spectroscopy ($E/\Delta E$ $100 - 500$).

XMM-Newton data are used in the work presented in Chapter 8.

[ii] These effective areas are quoted at 1.5 keV. Note that effective area is a strong function of energy.

Figure 3.4 An artist's impression of *Fermi*. The large silver rectangular prism on the top is the LAT, and the yellow cylinders in the bottom are the GBM. Image from `heasarc.gsfc.nasa.gov/mission_pages/GLAST/multimedia/`.

THE *Fermi* LARGE AREA TELESCOPE

Fermi was launched on the 11^{th} of June 2008. It has two primary science instruments: the Large Area Telescope, and the gamma-ray Burst Monitor. An artist's impression of *Fermi* is shown in Figure 3.4.

The *Fermi* Large Area Telescope (LAT) is a gamma-ray telescope sensitive in the 20 MeV to 300 GeV band. LAT has a field of view of $\sim$ 8000 square degrees and, in standard operating mode, surveys the entire sky once every three hours (Atwood et al., 2009). LAT is a pair production telescope wherein an incoming gamma-ray hits a layer of Tungsten, creating an electron positron pair. These pairs are then tracked through a series of silicon detectors, until they enter a calorimeter. These tracks are used to reconstruct the incoming gamma-rays' sky position and energy.

The calibration of LAT is continuously being improved as the knowledge of the detector and its operating environment improves. As of the writing of this thesis, the most up-to-date calibration is known as Pass 8 (Atwood et al., 2013). *Fermi* LAT data are used in the work presented in Chapter 8.

The Gamma-ray Burst Monitor (GBM) is an all sky monitor sensitive in the 8 keV–

30 MeV range with a field of view that covers the entire sky not occulted by the Earth Meegan et al. (2009). It consists of twelve sodium iodide (NaI) scintillation detectors, sensitive from 8 keV–1 MeV and two bismuth germanate (BGO) scintillation detectors, sensitive from $\sim$ 200 keV–$\sim$ 40 MeV. GBM is not a focusing instrument, and determines source location based on the relative time of arrival of a burst at each of the individual detectors which make up the instrument. While I do not directly use GBM data in this thesis, the GBM is sensitive to magnetar-like bursts, as we shall see in Chapter 8.

4

On the Braking Index of the Unusual High-B Rotation-Powered Pulsar PSR J1846−0258

The contents of this chapter were first published with the same title in Archibald et al. (2015b).

PSR J1846−0258 is a ∼800 year old pulsar located in the Kesteven 75 supernova remnant, and powers a bright pulsar wind nebula (Gotthelf et al., 2000). It has a rotation period of ∼327 ms and is one of the youngest known pulsars. For the majority of its observed lifetime, PSR J1846−0258 behaved as if it were a typical rotation-powered pulsar, with its X-ray emission being much less than the luminosity explainable by its spin-down power. Curiously, however it has no detectable radio emission (Archibald et al., 2008). PSR J1846−0258 is also one of the eight pulsars with a measured braking index, observed to be 2.65±0.01 from 2000 to 2006 (Livingstone et al., 2006). For more information on braking indices, see § 1.4.1.

In 2006, PSR J1846−0258 underwent a rare event - its pulsed X-ray flux increased dramatically, it had a large glitch, and emitted several magnetar-like bursts (Gavriil et al., 2008; Kumar & Safi-Harb, 2008; Kuiper & Hermsen, 2009). PSR J1846−0258 remains the only seemingly rotation-powered pulsar to display such distinctly magnetar-like behaviour, making it an interesting transition object between the two classes[i].

After this magnetar-like outburst, PSR J1846−0258 went back to manifesting itself as a rotation-powered pulsar (Livingstone et al., 2011). However, after timing the source for more than two years post-outburst, Livingstone et al. (2011) measured a braking index of $n = 2.16 \pm 0.13$ during this period, a value inconsistent with the braking index measured prior to the outburst. While the braking index is expected to change on a time scale of thousands of years, e.g. due to a gradual change in magnetic-field strength due to the Hall effect (see e.g. Contopoulos & Spitkovsky, 2006; Gourgouliatos & Cumming, 2015), such a sudden change is unexpected in the

---

[i] This is no longer true; see Chapter 8.

standard models.

Here we report a further five years of X-ray timing observations of PSRJ1846−0258, for a total of seven years after the magnetar-like outburst. We show that the braking index is consistent with the post-outburst measurement of Livingstone et al. (2011), and inconsistent with that prior to the outburst. This indicates that the 2006 magnetar-like outburst resulted in a persistent change in the braking index in the source.

OBSERVATIONS AND ANALYSIS

RXTE

In this work, we analyse observations of PSR J1846−0258 from the PCA aboard *RXTE* from January 2008 until the decommissioning of *RXTE* in 2011 December. For information on *RXTE*, please refer to § 3.2.

Observations were obtained from the HEASARC archive and barycentered to the location of PSR J1846−0258, $RA = 18^h46^m24.94^s$, $DEC = -02°58'30.1''$ (Helfand et al., 2003) using the `barycorr` tool in `HEASOFT` v6.16. Observations were filtered to remove non-astrophysical events using `xtefilt`. In order to maximize the signal-to-noise ratios of pulse profiles so as to minimize uncertainties on resulting TOAs (see §4.3),we used events from all layers of the then-operational PCUs.

In total 363 *RXTE* observations providing $\sim$ 0.9 Ms of exposure time were analysed in this work spanning January 2008 to December 2011. Observations taken within 2 days of each other were merged, resulting in 177 TOAs for a typical exposure time of 5 ks per TOA.

Swift XRT

We began observing PSR J1846−0258 with the *Swift* XRT on 2011 July 25 as part of a campaign to monitor several magnetars (see e.g. Archibald et al., 2013; Scholz et al., 2014a; Archibald et al., 2015c). For information on *Swift*, please refer to § 3.3. Level 1 data products were obtained from the `HEASARC` *Swift* archive, reduced using the `xrtpipeline` standard reduction script, and corrected to the Solar System barycentre using the location of PSR J1846−0258, with `HEASOFT` *v*6.16. Individual exposure maps, spectra, and ancillary response files were created for each orbit and then summed. We selected only Grade 0 events for spectral fitting as higher Grade events are more likely to be caused by background events (Burrows et al., 2005). To maximize the signal-to-noise ratios of pulse profiles so as to minimize uncertainties on resulting pulse times-of-arrival (see §4.3), only photons from 2.7–10 keV were used.

To investigate the flux and spectral evolution of PSR J1846−0258, a circular region having a 10-pixel radius centred on the source was extracted. As well, an annulus of inner radius 75 pixels and outer radius 125 pixels centred on the source was used to extract background events.

In total 66 XRT observations totalling 541 ks of exposure time were analysed in this work. Observations taken less than 5 days apart were grouped to extract a single TOA yielding 47 TOAs, with a typical exposure time of 10 ks per TOA.

TIMING ANALYSIS

PHASE-COHERENT TIMING ANALYSIS

TOAs for all *RXTE* and *Swift* observations were extracted using a Maximum Likelihood (ML) method as described in § 2.4. In order to create the continuous model of the pulse profile, first we create a high signal-to-noise template profile by folding many observations together using a whitened timing solution (i.e. a solution which produced residuals consistent with gaussian or 'white' noise). For *RXTE*, the template was derived from folding all pre-outburst observations, and for *Swift*, using all the observations. Separate templates were used for the *RXTE* and *Swift* observations to account for differences in the responses of the telescopes. In both cases, a continuous model of the profile was created by fitting the high signal-to-noise template with a Fourier model using the first two harmonics. Two harmonics were chosen to optimally describe the pulse shape, as determined by the H-test (de Jager et al., 1989; Archibald et al., 2015a).

These TOAs were fitted to a timing model in which the phase as a function of time t can be described by a using the method described in Chapter 2.

In Figure 4.1 we show the timing residuals in the range MJD 54492 to 56880, the period after the magnetar-like outburst and glitch recovery have relaxed. For details about the glitch and subsequent recovery, see Kuiper & Hermsen (2009) and Livingstone et al. (2010).

Finding a single phase-coherent solution over the entire seven-year post-outburst data set is not possible due to a phase ambiguity during the Sun constraint period from MJD 56246 to 56338. This is indicated in Figure 4.1 by a dashed vertical line. We were able to find two phase-coherent solutions, one before this Sun constraint and

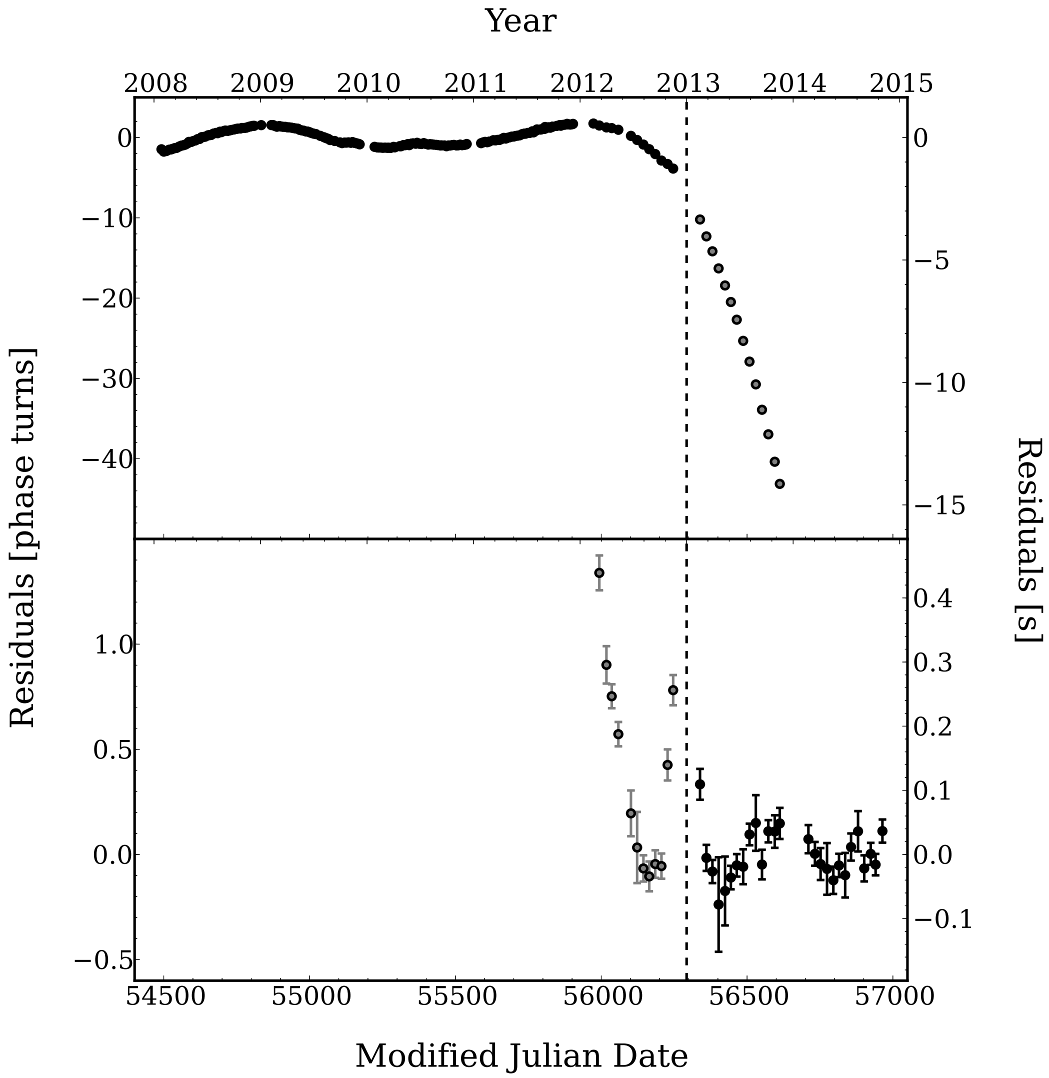

Figure 4.1 Timing residuals of PSR J1846−0258 from MJD 54492-56880 (post-outburst) for the solutions presented in Table 8.1. The top panel shows the residuals of Solution 1. The bottom panel shows the residuals of Solution 2. The vertical dashed line indicates where there is a phase ambiguity; see §4.3 for details. Note that Solution 1 is fitted only to data before the phase ambiguity, and Solution 2 only to those after.

one after. The two timing solutions are presented in Table 8.1.

This loss of phase coherence could be due either to a glitch, or to timing noise. Fitting for a glitch during the Sun-constraint period using a timing solution up to $\ddot{\nu}$ yields $\Delta\nu/\nu = 5.7 \pm 0.5 \times 10^{-8}$ and $\Delta\dot{\nu}/\dot{\nu} = -2.5 \pm 0.4 \times 10^{-4}$ over the *Swift* campaign. Fitting using both the *RXTE* and *Swift* data sets gives glitch parameters ranging from $\Delta\nu/\nu$ of -9×10^{-8} to 1.7×10^{-7}. We note that these values vary based on the time-span fit and the number of frequency derivatives used in the fit. Finally, we note that fitting a continuous solution over the gap yields comparable residuals to the glitch fits. Thus we do not need to invoke a sudden glitch to explain the timing behaviour of PSR J1846−0258 at this epoch.

Partial Phase-Coherent Timing Analysis

Measurements of $\ddot{\nu}$ can be susceptible to contamination from timing noise (e.g. Hobbs et al., 2010, and § 2.2). To mitigate this effect, we fit small segments of data to make local measurements. For all methods presented below, relative pulse numbers were fixed to those given by the fully phase-coherent timing solution. No timing solution was fit overlapping the phase ambiguity.

For each small segment of data, using the established pulse numbers, TOAs were fit to a timing solution consisting of only ν and $\dot{\nu}$. The time spans were determined by allowing a maximum χ^2_ν of $\sim$1 and the condition that there was no apparent-by-eye red-noise signal in the residuals. When this condition was met, we moved over by half the number of TOAs in that solution, and fit again until the criteria were met. We did not allow a solution to span over a Sun-constraint period.

In Figure 4.2, we show these measurements of $\dot{\nu}$ over the data set. The top panel shows $\dot{\nu}$ over time. The middle panel shows $\dot{\nu}$ over time subtracting a constant slope

Table 4.1 Phase-Coherent Timing parameters for PSR J1846−0258.

First Phase-coherent Solution	
Dates (MJD)	54492.0-56246.7
Dates	2008 Jan 27 - 2012 Nov 15
Epoch (MJD)	55369.00000
ν (s^{-1})	3.059 040 903(4)
$\dot{\nu}$ (s^{-2})	$-6.65131(1) \times 10^{-11}$
$\ddot{\nu}$ (s^{-3})	$2.937(8) \times 10^{-21}$
rms residual (ms)	304.4
rms residual (phase)	0.931
Braking index, n	2.031(6)
Second Phase-coherent Solution	
Dates (MJD)	56338.7-56964.20
Dates	2013 Feb 15 - 2014 Nov 03
Epoch (MJD)	56651.00000
ν (s^{-1})	3.051 693 972(3)
$\dot{\nu}$ (s^{-2})	$-6.61349(2) \times 10^{-11}$
$\ddot{\nu}$ (s^{-3})	$3.30(4) \times 10^{-21}$
rms residual (ms)	32.4
rms residual (phase)	0.099
Braking index, n	2.30(3)

Note: Figures in parentheses are the nominal 1σ TEMPO2 uncertainties in the least-significant digits quoted.

consisting of the pre-outburst braking index, 2.65±0.01 (Livingstone et al., 2011). Note the clear linear trend in the middle panel indicating that the pre-outburst braking index does not describe the data well.

We fit a slope to the post-outburst $\dot{\nu}$ in order to obtain a measurement of $\ddot{\nu}$, and thus a braking index. The $\dot{\nu}$ measurements of PSR J1846−0258 have a scatter larger than would be suggested by their formal errors, therefore we use a bootstrap method. The bootstrap method is robust for error estimation when only a small number of measurements are available (Efron, 1979) and the formal uncertainties are thought to not fully describe the data.

For the full post-outburst data set, this yielded a measurement of $\ddot{\nu} = 3.17 \pm 0.05 \times 10^{-21}$ s^{-3} corresponding to a braking index of $n = 2.19 \pm 0.03$ for the bootstrap method. The residuals of this fit can be seen in the bottom panel of Figure 4.2.

In order to verify that the phase ambiguity between the two timing solutions presented in Table 8.1 does not affect our result, we split the data into the corresponding two segments. Fitting from MJD 54492.0-56246.7 gives a braking index of $n = 2.09 \pm 0.05$. Fitting MJD 56338.7-56880.5 gives $n = 2.23 \pm 0.07$. These two segments gave consistent slopes at the 1.4σ level, and are both inconsistent with the pre-outburst braking index. This gives us confidence that the measured post-outburst braking index of $n = 2.19 \pm 0.03$ represents a long-lived change in the braking index of $\Delta n = -0.46 \pm 0.03$, a 14.5$\sigma$ difference.

TIMING NOISE

In order to quantify the effect of timing noise that could be contaminating the measurement of the braking index, we fit a timing solution consisting of a frequency and three frequency derivatives for each year, ending a solution at times of a glitch, or the

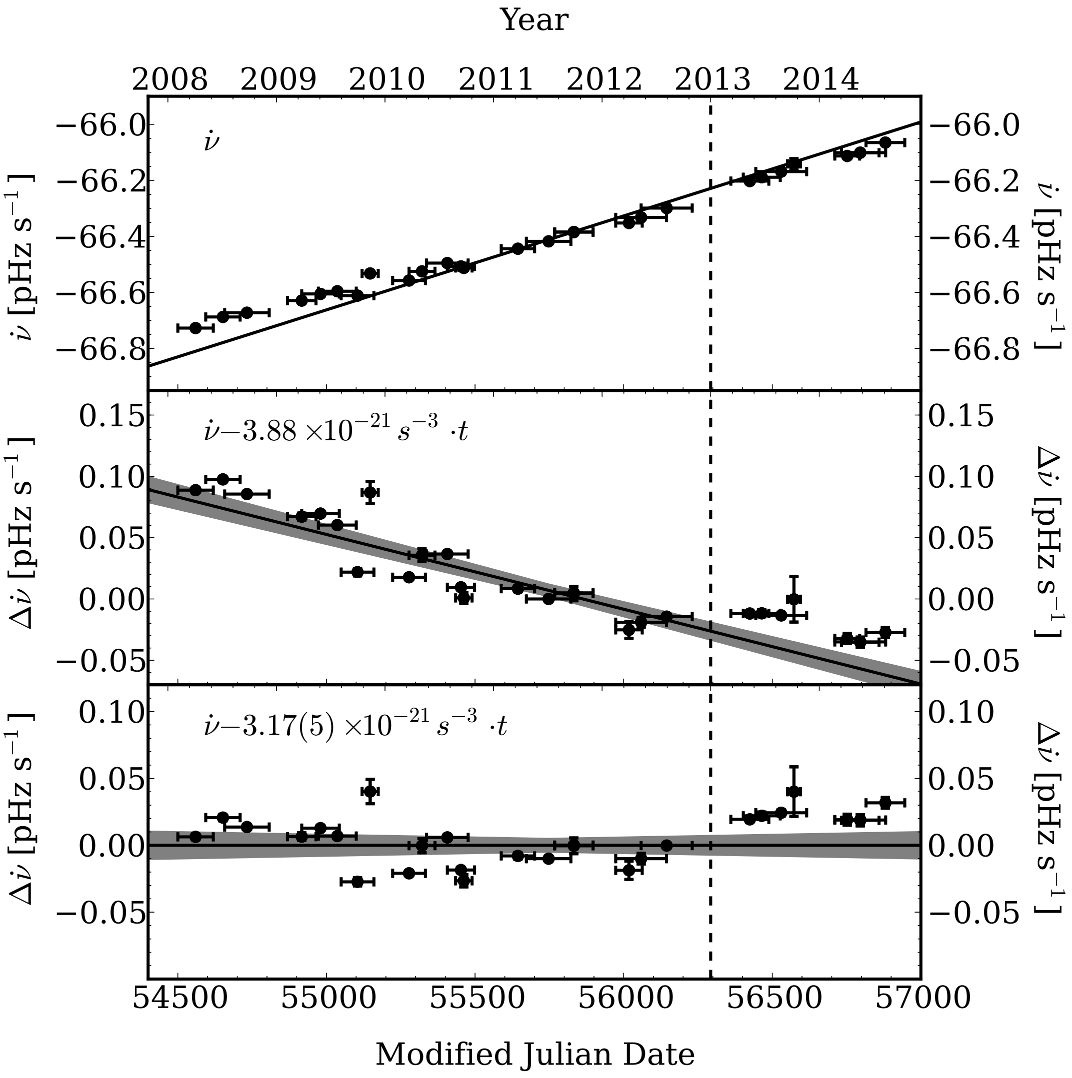

Figure 4.2 $\dot{\nu}$ measurements for PSR J1846−0258 from MJD 54492-56880. The top panel shows the measured $\dot{\nu}$. The solid black line shows the pre-outburst $\ddot{\nu}$ of 3.88×10^{-21} s^{-3}. The middle panel shows the same data subtracting the pre-outburst $\ddot{\nu}$. The black line in this panel shows the difference between the pre-outburst measurement, and the best-fit post-outburst $\ddot{\nu}$ of $3.17\pm0.05\times10^{-21}$ s^{-3}. The grey shaded region shows the 1σ bounds on this determined from a bootstrap analysis to the full data set as described in the text. The bottom panel shows the $\dot{\nu}$ residuals after subtracting the best-fit slope from above. The vertical dashed line indicates where there is a phase ambiguity; see §8.3.1 for details.

start of Sun-constraint.

Following the method of Livingstone et al. (2011), we measure the quantity

$$\Delta_{\ddot{\nu}} \equiv \log\left(\frac{1}{24}\frac{|\ddot{\nu}|\, t^4}{\nu}\right) \tag{4.1}$$

where t is the length of time over which the solution was fit, $\sim 2.5 \times 10^7$ s. This is analogous to the Δ_8 parameter of Arzoumanian et al. (1994) where Δ_8 is used as an estimation of the contributions of $\ddot{\nu}$ to the accumulated phase deviation of the pulsar. As $\ddot{\nu}$ is physically relevant in timing measurements of PSR J1846−0258, we use $\Delta_{\ddot{\nu}}$ as an estimate of the phase contamination from $\dddot{\nu}$ and higher order effects.

In Figure 4.3, we show $\Delta_{\ddot{\nu}}$ over the 15 years of timing of this source. While the scatter is high, $\Delta\ddot{\nu}$ shows a possible increase for the period following the magnetar-like outburst in 2006.

Before the outburst, e.g. from 2000 to 2006, the weighted mean was $\Delta_{\ddot{\nu}} = 0.1 \pm 0.2$. For the first period after the outburst, 2007, $\Delta_{\ddot{\nu}} = 1.16 \pm 0.03$, substantially higher than at any other time. After this, the timing noise decreased to a level that is marginally higher than the pre-outburst noise, with the weighed mean of $\Delta_{\ddot{\nu}} = 0.6 \pm 0.2$ from 2008-2014. Thus, the level of timing noise clearly increased following the magnetar-like outburst but appears to be relaxing back to the pre-outburst level on a time scale of several years.

RADIATIVE PROPERTIES

SPECTRAL ANALYSIS

Swift XRT spectra were extracted from the selected regions using `extractor`, and fit

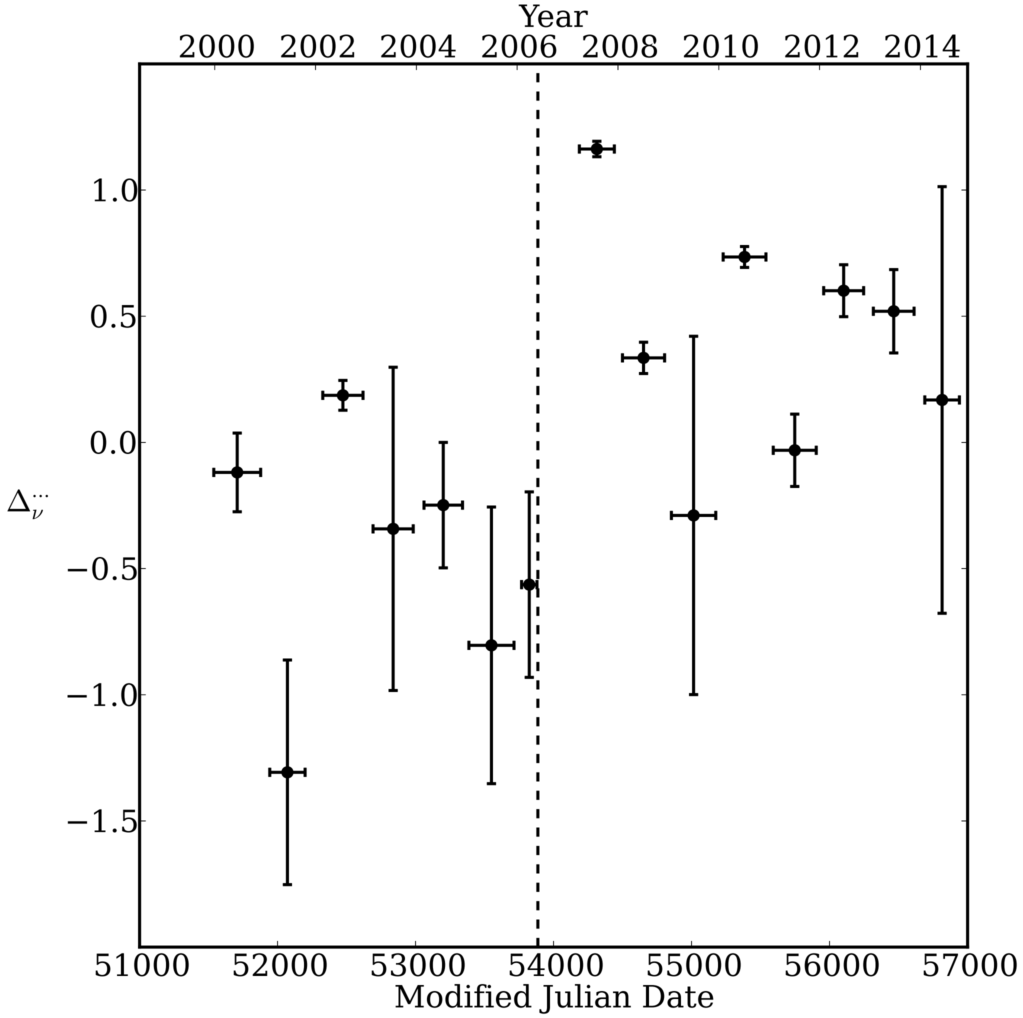

Figure 4.3 Timing noise in PSR J1846−0258 over 15 years of X-ray timing as described by the $\Delta_{\ddot{\nu}}$ parameter; see equation 4.1. The vertical dashed line indicates the epoch of the outburst.

using `XSPEC` package version 12.8.2[ii]. Spectral channels were grouped to 1 count per bin, and fitted using C-stat minimization (Cash, 1979). The spectrum was fit with a photoelectrically absorbed power law. Photoelectric absorption was modelled using `XSPEC` `tbabs` with abundances from Wilms et al. (2000), and photoelectric cross-sections from Verner et al. (1996). Due to both the nature of the windowed timing read-out mode of the XRT, and the fact that the XRT point spread function is comparable to the size of the bright, central region of the nebula, we are unable to separate the flux coming from the pulsar itself from the bulk of the pulsar wind nebula which surrounds it.

As all of the *Swift* observations had consistent flux and spectral parameters, we co-fit all observations simultaneously. This yielded a best-fit model with $N_H = (4.43 \pm 0.05) \times 10^{22}$ cm^{-2} and $\Gamma = 1.80 \pm 0.02$. We note that the best-fit power-law index is consistent with that of the pulsar wind nebula reported by Kumar & Safi-Harb (2008) and Ng et al. (2008), as well as that reported in the 20–300 keV range using *INTEGRAL* (Kuiper & Hermsen, 2009).

The absorbed 0.5–10 keV X-ray flux measured over the *Swift* campaign of the combined pulsar and pulsar wind nebula was $(2.04 \pm 0.02) \times 10^{-11}$ erg cm^{-2} s^{-1}. In *Chandra* observations taken 2000 (Ng et al., 2008) and 2009 (Livingstone et al., 2011), the absorbed 0.5–10 keV flux from the combined pulsar and pulsar wind nebula were $(1.81 \pm 0.03) \times 10^{-11}$ erg cm^{-2} s^{-1} and $(1.73 \pm 0.07) \times 10^{-11}$ erg cm^{-2} s^{-1} respectively. While formally, our measured *Swift* flux and the archival *Chandra* fluxes are inconsistent, the cross-calibration between X-ray instruments is only accurate to the ~10% level; see Tsujimoto et al. (2011). Therefore we find no evidence of a changing flux for the system to the level of instrumental uncertainties.

[ii] http://xspec.gfsc.nasa.gov

PULSE PROFILE ANALYSIS

To look for changes in the pulse profile, we folded each observation using 16 phase bins. Each profile was compared to the high signal-to-noise-ratio pulse template described in §8.3.1 by subtracting a fitted DC offset, and using a multiplicative scaling factor to minimize the difference between the template and scaled profile as determined by a χ^2 minimization. For both *RXTE* and *Swift*, all profiles are consistent with the respective telescope's standard template.

It has been shown previously that PSR J1846−0258 exhibited no significant change in its X-ray pulse profile during the magnetar event (Kuiper & Hermsen, 2009; Livingstone et al., 2010). For *RXTE* we now have comparable data from both before and after the magnetar-like outburst. This allowed us to search for long-term lower-level changes in the pulse profile. To do so, we combined all observations for which we had a valid timing solution into a two high signal-to-noise-ratio profiles with 64 phase bins representing the pulse profile before and after the magnetar-like outburst. To do this, we fitted each year of TOAs to a timing solution, using as many frequency derivatives as necessary to whiten the residuals. Each year of data was then folded into a 64-bin profile, and aligned with other years' profiles using cross-correlation. This resulted in two high signal-to-noise-ratio profiles: the first using 918 ks of exposure time from January 2000 to March 2006, and the second using 871 ks from January 2008 to December 2011. These two normalized, DC-subtracted, high signal-to-noise profiles are shown in Figure 4.4, as well as the difference between them. The residuals have $\chi^2_\nu/(dof) = 0.988/(62)$ indicating the profiles are statistically identical. This is consistent with the lack of profile change reported by Kuiper & Hermsen (2009) and Livingstone et al. (2011).

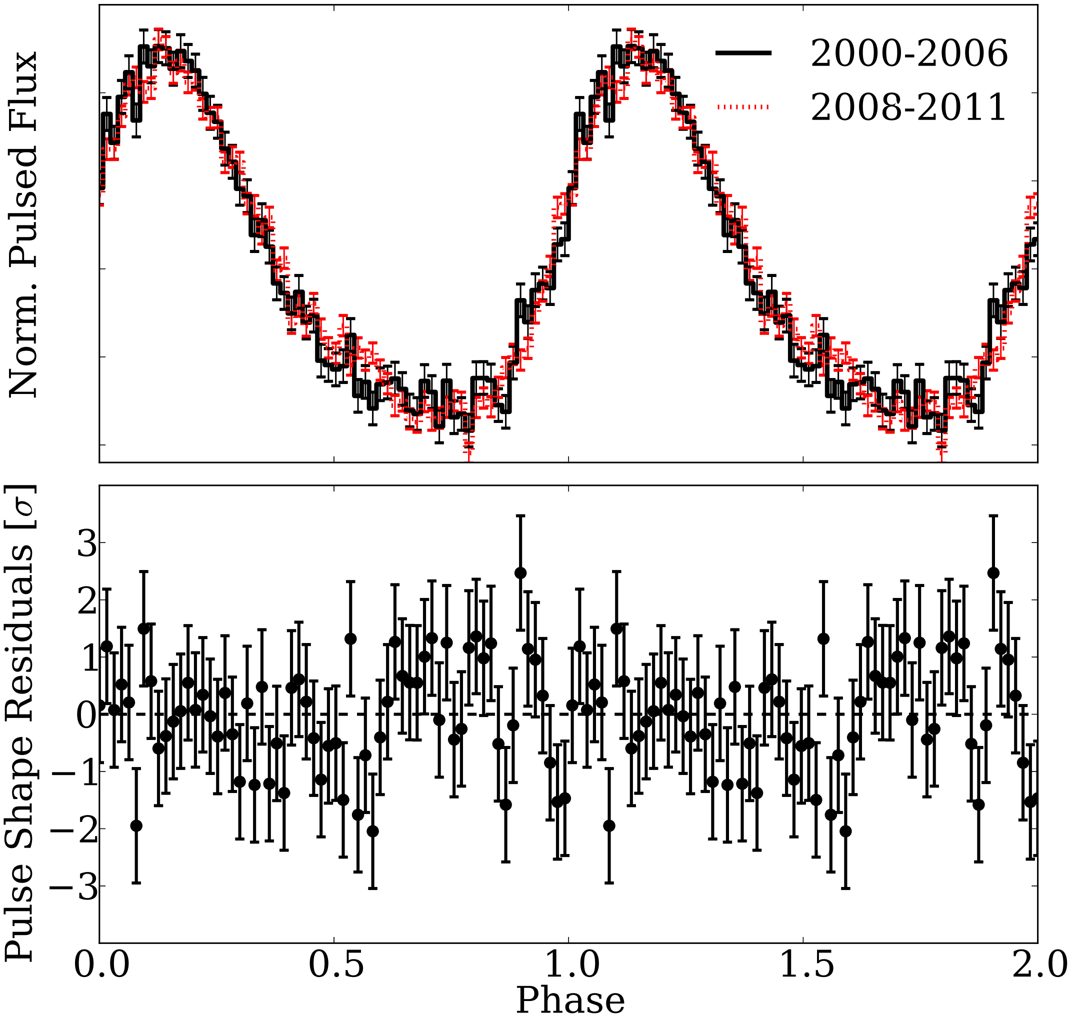

Figure 4.4 Normalized *RXTE* pulse profiles of PSR J1846−0258. The solid black profile shows the profile from January 2000 to March 2006, just before the 2006 outburst. The red dotted profile shows the profile from 2008 January to 2011 December. The bottom panel shows the residual difference between the two profiles. The residuals have $\chi^2_\nu/(dof) = 0.988/(62)$ indicating the profiles are statistically identical.

BURST SEARCH

All *Swift* observations were searched for magnetar-like bursts by binning the source region light curves into 0.01-s, 0.1-s, and 1.0-s bins. The counts in each bin were compared to the mean count rate of its Good Timing Interval (GTI), assuming Poisson statistics, similar to the methods described by Scholz & Kaspi (2011). We found no significant bursts in the *Swift* observations.

For the *RXTE* PCA, due to the background being highly variable, each 60-second interval was treated in a similar manner to a *Swift* GTI. An additional constraint was placed on the PCA data that a putative burst must be detected in all operational PCUs to be considered real. We find a previously unreported burst on MJD 55070, 27 August, 2009. This burst has a T_{90}, the time duration in which 90% of a burst's fluence is collected, of 7 ± 1 ms and a fluence of 12 ± 3 counts per PCU (24 ± 5 total counts). This corresponds to a false alarm probability of $\sim 10^{-20}$ for the observation. The burst is shown in Figure 4.5.

We note, however, that the field of view contains other known magnetars including AX J1845.0−0300 (Torii et al., 1998) located 0.38° from the centre of the pointing, and 1E 1841−045 (Vasisht & Gotthelf, 1997), located 2.3° from the centre of the pointing. As 1E 1841−045 is an active and frequent burster (e.g. Lin et al., 2011; An et al., 2015), it is possible that the burst originated from this source. While we cannot exclude the possibility that this burst originated from PSR J1846−0258, we note that there is no change to either the radiative properties, or timing behaviour at these epochs to within our measurement uncertainties.

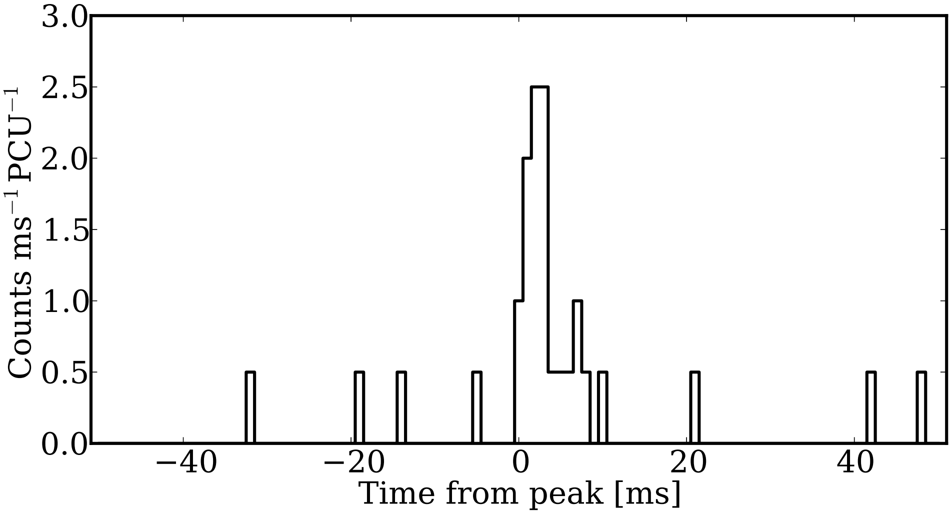

Figure 4.5 Burst from the direction of PSR J1846−0258 on MJD 55070. The time series is binned with 1-ms time resolution and covers the full 2–60 keV range of the PCA of both operational PCUs.

DISCUSSION

We have presented seven years of post-outburst timing of PSR J1846−0258 in which we measure the braking index to be $n = 2.19 \pm 0.03$. This is discrepant at the 14.5σ level from the pre-outburst braking index of $n = 2.65 \pm 0.01$ (Livingstone et al., 2006). We note that this measurement is made over a comparable span of time to that over which the pre-outburst braking index was measured.

Only one other rotation-powered pulsar has had a radiative change associated with a glitch: PSR J1119−6127 [iii]. Following a glitch in 2007, the radio pulse profile changed from single- to double-peaked. This double-peaked profile was only seen once, during the first post-glitch observation of the pulsar, and had returned to the single-

---

[iii] See Chapter 8 for a new radiatvely loud glitch from this source.

peaked profile by the next observation (Weltevrede et al., 2011). It appears that PSR J1119−6127 may have undergone a change in braking index of similar magnitude following this radiatively loud glitch, with a $\sim 15\%$ reduction in n at the time of the glitch (Antonopoulou et al., 2015). However, only formal phase-connected timing errors are given for this possible change in the braking index, and this method is susceptible to timing noise, (e.g. Hobbs et al., 2010; Livingstone et al., 2011). Given this, and the large non-white residuals seen after the fitting, the true significance of this result is currently unknown.

It is interesting that the only two nominally rotation-powered pulsars which have been observed to have radiatively loud glitches are two of those with the highest dipole-inferred magnetic field; see Chapter 8. In both cases the observed braking indices were consistent with being constant through radiatively quiet glitches and decreased following their loud glitches. This decrease in braking index effectively has the pulsars moving faster towards the magnetar population on the P-$\dot{P}$ diagram. This, together with radiatively loud glitches being a defining characteristic of magnetars (e.g. Dib & Kaspi, 2014) is suggestive that the large magnetic field in these two seemingly rotation-powered pulsars is responsible for their unusual activity.

There was also a change in $\ddot{\nu}$ in the high-magnetic-field rotation-powered pulsar PSR J1718−3718 following a large glitch (Manchester & Hobbs, 2011). While the implied $\ddot{\nu}$ both before and after this pulsar's glitch gives nonphysical braking indices, $n \sim -17(5)$ and $n \sim -146(2)$, the measured $\ddot{\nu}$ were consistent over ~ 3000 days before the glitch, and for the ~ 700 days after it. Again, while the implied braking indices seem nonphysical, it is interesting that $\ddot{\nu}$ changed with a glitch in yet another high-magnetic-field pulsar.

A possible change in the braking index was seen in the Crab pulsar, where for a

$\sim$ 11-yr span the measured braking index was $\sim 8\%$ lower than the long-term average braking index. This period of low braking index occurred during a period of higher-than-normal glitch activity, and Lyne et al. (2015) note that this possible change is most likely due to unmodelled glitch parameters.

One possibility to explain a substantial change in a braking index, such as the one we observe in PSR J1846−0258, would be contamination due to a long-term glitch recovery. If this is the case, one would expect a bias towards a higher $\ddot{\nu}$, and thus a higher n (Lyne et al., 2000). This is due to the typical glitch behaviour of an exponentially decaying ν, which leads to a decrease in the magnitude of the measured $\dot{\nu}$ as a function of time, and thus to an artificially larger braking index. This is the opposite of what we observe.

There are several theoretical models to explain the observation that all measured braking indices are less than the canonical $n = 3$ of a magnetic dipole in a vacuum. As yet, the change in braking index observed in PSR J1846−0258 is unique[iv] – it is larger than ever before seen, and appears to be constant following the magnetar-like event. Here we will discuss the consequences of a changing braking index in the context of these models.

In particle-wind models (see e.g. Harding et al., 1999; Tong et al., 2013), one can explain any braking index between $n = 1-3$ by combining spin-down effects from both the standard magnetic dipole radiation ($n = 3$) with that of angular momentum loss from an outflowing particle wind ($n = 1$). As shown in Lyne et al. (2015), one can express the fraction of spin-down power due to a particle wind, compared to the magnetic dipole as:

$$\epsilon = \frac{3-n}{n-1}. \tag{4.2}$$

[iv] This is no longer true; see Chapter 9.

This would imply that before 2006, the wind spin-down was 21±1% of PSRJ1846−0258's dipolar spin-down and 68 ± 4% after 2006. This model predicts a relation between the braking index and the luminosity of the particle wind (Harding et al., 1999; Livingstone et al., 2011):

$$L_p = (3-n)^2 \left(\frac{\dot{\nu}}{\nu}\right) \frac{6I^2c^3}{B^2R^6} \tag{4.3}$$

where I is the moment of inertia, B the magnetic field, and R the pulsar's radius. Assuming neither the magnetic field nor moment of inertia changed substantially, the luminosity of the pulsar wind nebula might have been expected to increase by a factor of approximately 5. Such a significant flux change was ruled out by deep *Chandra* observations by Livingstone et al. (2011), as well as by the consistency of the flux during the *Swift* campaign with the pre-outburst flux reported by Kumar & Safi-Harb (2008) to within the telescopes' cross calibration uncertainties, ∼10%.

One can also obtain a braking index different from 3 by relaxing the assumption of a constant magnetic dipole in a vacuum, allowing the dipole to change over time, (see e.g. Gunn & Ostriker, 1969; Manchester et al., 1985; Blandford & Romani, 1988). This is expressed in a convenient form by Lyne et al. (2015):

$$n_{obs} = n_{dip} + \frac{\nu}{\dot{\nu}} \left(-\frac{\dot{I}}{I} + 2\frac{\dot{\alpha}}{\tan\alpha} + 2\frac{\dot{M}}{M} \right). \tag{4.4}$$

To explain a braking index lower than n_{dip} of 3, either the moment of inertia I is decreasing, or either the magnetic dipole moment M or the angle of mis-alignment between the spin and magnetic axis α are increasing. Furthermore, this implies that at the epoch of the magnetar outburst, the fractional rate of change of the magnitude of either $\dot{I}/I$, $\dot{\alpha}/\tan\alpha$, or $\dot{M}/M$ increased by a factor of 2.3±0.2. It does not seem physically plausible to have so large a change in either $\dot{I}/I$ nor $\dot{M}/M$, especially given the lack of change of the flux of the pulsar wind nebula. Such a change in either $\dot{\alpha}$ or α also seems improbable, given the lack of any detected change in the pulse profile (see §4.4.2).

One could also change the braking index by altering the geometry of the magnetosphere (see e.g. Thompson et al., 2002; Contopoulos & Spitkovsky, 2006). In the twisted neutron-star magnetosphere model of Thompson et al. (2002), the braking index of a pulsar is given by $n = 2p + 1$, where p is the radial index. The observed change in braking index in this model implies that for PSR J1846−0258, the "twist" between the north and south hemispheres increased by $\sim$ one radian at the time of the outburst, which should lead to a corresponding increase in the X-ray luminosity of $\sim 50\%$. This is not seen. Additionally, in any magnetospheric origin for a change in braking index, one would need to modify the magnetosphere in such a way as to maintain a constant pulse profile over the magnetar-like event, which seems challenging.

Beloborodov (2009) has a modified version of this model in which instead of a global twist in the magnetosphere, the twist is concentrated into a localized region known as a "j-bundle." This j-bundle will increase the dipole moment of the neutron star, leading to an increased spin-down rate. As the j-bundle shrinks, the effective dipole moment should decrease with time, leading to a positive contribution to $\ddot{\nu}$ and thus the braking index. While this model can be used to explain the glitch behaviour of PSR J1846−0258 associated with the magnetar-like event (Livingstone et al., 2010), it does not immediately explain our observed long-term decrease in braking index.

Conclusions

The observed braking index of PSR J1846−0258 has significantly changed following its period of magnetar-like behaviour. This long-term change in n is, to within measurement errors, unaccompanied by any corresponding long-lived change in the flux of the source, or any change in its pulse profile. This is in contrast to most of the models discussed above where a correlated change in the X-ray luminosity is expected for both wind-based models (Harding et al., 1999) and global magnetospheric twist based models (Thompson et al., 2002). As well, models which modify the assumptions of a constant magnetic dipole require far too high a change in I or M to be physically plausible, or a change in α or $\dot{\alpha}$ which seem unlikely given the stable pulse profile.

The most plausible explanation for a changed braking index appears to be due to some form of change in magnetospheric configuration, but this change is constrained by our observations to be unaccompanied by any large-scale change in flux, spectrum or pulse profile. One possible way to probe the magnetosphere of pulsars, and therefore test this hypothesis, is by means of X-ray polarimetry. Measurements of polarization fractions and angles are very sensitive to viewing geometries, as well as twists in the magnetosphere (e.g. van Adelsberg & Lai, 2006; Taverna et al., 2014). In the near future (∼2020), this will be possible as the *Imaging X-ray Polarimetry Explorer (IXPE)* has been selected as a NASA Small Explorer class mission (Weisskopf et al., 2016).

5

A High Braking Index for a Pulsar

The contents of this chapter were first published with the same title in Archibald et al. (2016c).

Introduction

PSR J1640–4631 was discovered as a pulsating X-ray source in a *NuSTAR* survey of the Norma region of the Galactic plane (Gotthelf et al., 2014). It has a rotation period of ∼206 ms, and a spin-down rate of $\sim 9.7 \times 10^{-13}\,\mathrm{s\,s^{-1}}$ implying a surface magnetic field of $B \sim 1.4 \times 10^{13}$ G. The pulsar is located in the centre of the supernova remnant G338.1−0.0, and powers the pulsar wind nebula (PWN) HESS J1640−465, first detected in very high-energy gamma-rays and thought to be the most luminous TeV source in our Galaxy (Gotthelf et al., 2014). We undertook X-ray timing observations of PSR J1640–4631 starting shortly after discovery with the aim of measuring its braking index.

OBSERVATIONS AND ANALYSIS

All X-ray observations presented in this chapter were taken using *NuSTAR*. See § 3.4 for details about *NuSTAR*.

NuSTAR observations of PSR J1640–4631 were typically 20–50 ks, and the observation cadence can be seen in Figure 5.1. Level 1 data products were obtained from `HEASARC` and reduced using `nupipeline v0.4.4`. Photons from a circular region having a 30″ radius centred on the source were extracted. To maximize the signal-to-noise ratio of the pulse, we used only photons with energies in the 3.0–55 keV range.

Photon arrival times were corrected to the Solar System barycentre using the *Chandra* position of PSR J1640–4631, RA= $16^h40^m43.52^s$ DEC=$-46^\circ31'35.4''$ (Lemiere et al., 2009) using `barycorr` from `HEASOFT v6.17` and `v052` of the *NuSTAR* clock file.

Photon arrival times were used to derive an average TOA for each observation. The TOAs were extracted using a Maximum Likelihood method as described in § 2.4. To create the template, all observations were folded into a high signal-to-noise profile. This high signal-to-noise profile was then fitted to a Fourier model using the first two harmonics. Two harmonics were chosen to optimally describe the pulse shape, as determined by use of the H-test (de Jager et al., 1989).We verified that TOAs extracted using a cross-correlation method give consistent results. *NuSTAR*'s absolute timing calibration is accurate to ±3 ms (Madsen et al., 2015), smaller than our measurement uncertainties.

The TOAs were fitted to a standard timing model as described in § 2. This was done using the `TEMPO2` (Hobbs et al., 2006) pulsar timing software package. In Table 5.1 we present a fully phase-coherent timing solution for PSR J1640–4631 over the *NuSTAR* observation campaign. This is the only solution which provides a statistically acceptable fit, i.e. we have verified there are no pulse counting ambiguities. The residuals, the difference between our timing model and the observed pulse phases, can be seen in Figure 5.1. In the top panel, we show these residuals accounting only for ν and $\dot{\nu}$. The bottom panel shows the residuals for the full timing solution, accounting for $\ddot{\nu}$. Fitting for an extra frequency derivative, $\dddot{\nu}$ does not significantly improve the fit with the F-test indicating a 52% probability of the improvement of χ^2 being due to chance. We measure $\ddot{\nu} = (3.38 \pm 0.03) \times 10^{-22}\ \mathrm{s}^{-3}$ corresponding to a braking index of $n = 3.15 \pm 0.03$, where the uncertainty represents the 68% confidence interval.

This measured braking index is 5σ higher than that expected in the standard magnetic dipole scenario. In Figure 5.2, we show all measured braking indices; note how PSR J1640–4631 is the only measurement greater than the canonical $n = 3$ magnetic dipole line.

Timing Noise Simulations

A possible way to explain such a large measured braking index is contamination from timing noise. Timing noise refers to unexplained low-frequency modulations found in the timing residuals of many, particularly young, pulsars (Arzoumanian et al., 1994). For more information on timing noise, see § 2.2. The power spectral density (PSD) of

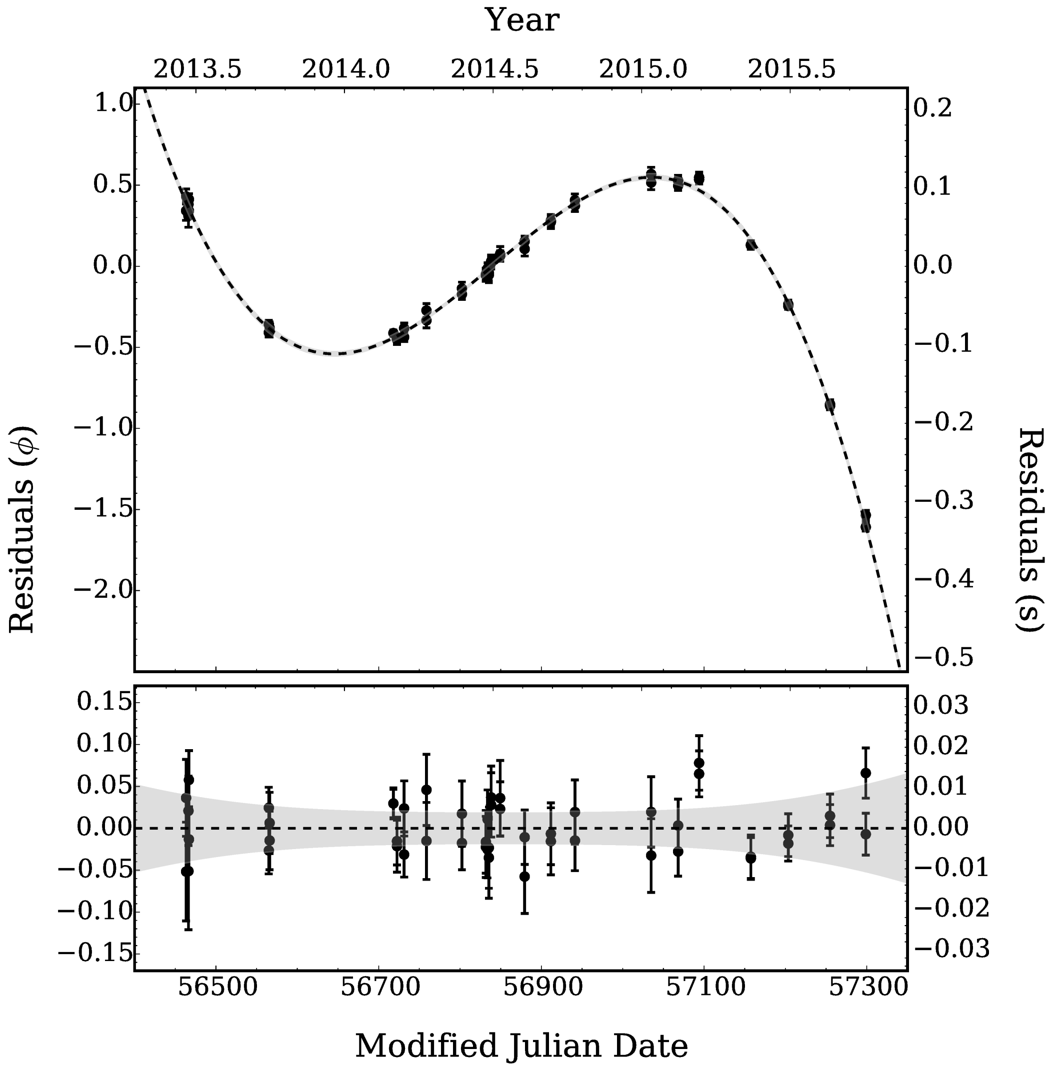

Figure 5.1 Timing residuals of PSR J1640–4631 from MJD 56463 to 57298, 29 September 2013 to 3 October 2015, for the solution presented in Table 5.1. The top panel shows the timing residuals subtracting only the contributions from ν and $\dot{\nu}$ with the dashed black line showing the fitted $\ddot{\nu}$ of $(3.38 \pm 0.03) \times 10^{-22}$ s^{-3}. The bottom panel shows the residuals after accounting for $\ddot{\nu}$. The gray bands in both panels indicate the 1-σ timing model uncertainties.

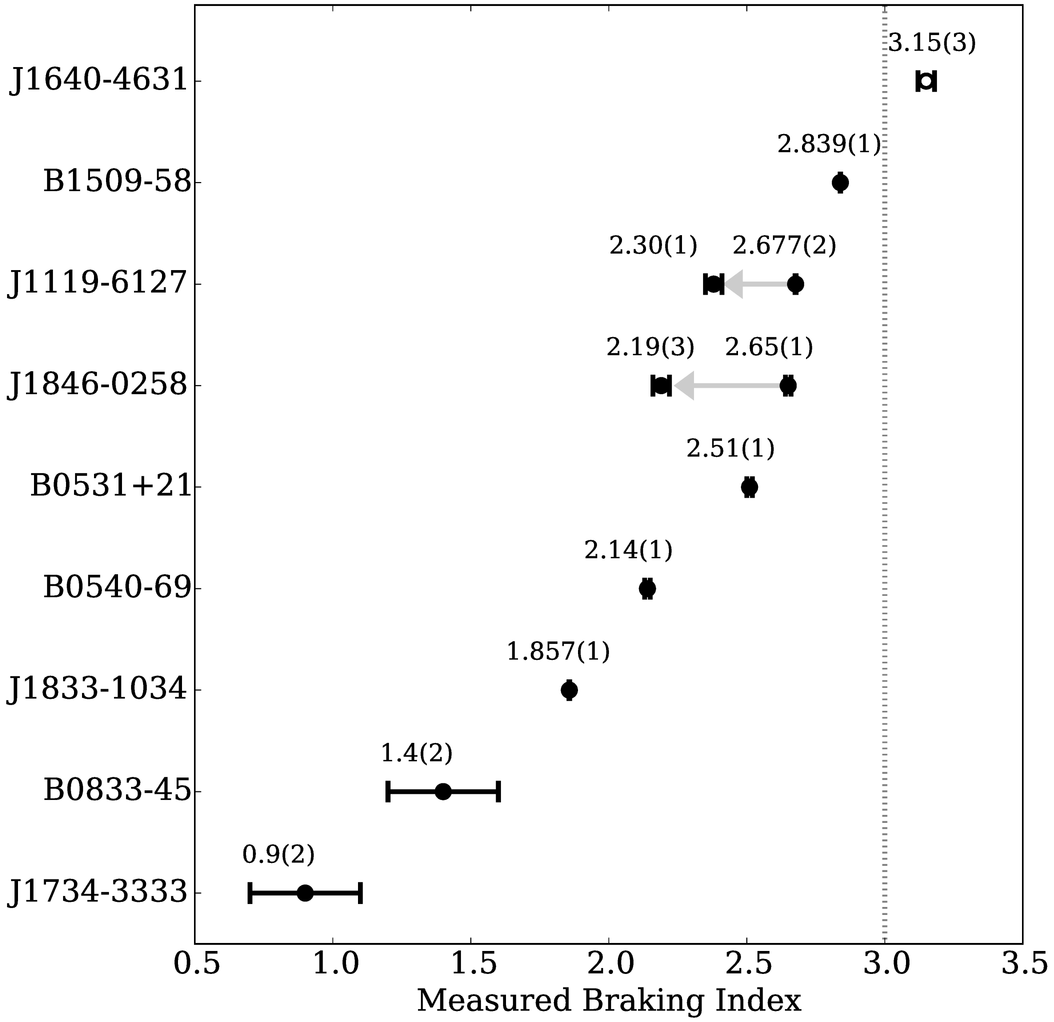

Figure 5.2 All measured braking indices. The gray dotted line indicates a braking index of three, that which is expected for a pure magnetic dipole. For PSR J1846−0258 (Archibald et al., 2015b) and PSR J1119−6127 (Antonopoulou et al., 2015), where the braking index changed following glitches, the gray arrows indicate the direction of change following the glitch. All other braking indices are from Lyne et al. (2015) and references therein.

Table 5.1 Phase-Coherent Timing Parameters for PSR J1640–4631.

Dates (MJD)	56463.0–57298.8
Dates	29 September 2013 – 3 October 2015
Epoch (MJD)	56741.00000
ν (s^{-1})	4.843 410 287 0(5)
$\dot{\nu}$ (s^{-2})	$-2.280\,830(4)\times10^{-11}$
$\ddot{\nu}$ (s^{-3})	$3.38(3) \times 10^{-22}$
$\lvert\dddot{\nu}\rvert$ (s^{-4})	$< 1.4 \times 10^{-30}$
rms residual (ms)	6.17
rms residual (phase)	0.030
χ^2_ν/dof	0.98/46
Braking index, n	3.15(3)

Note: Figures in parentheses are the nominal 1σ TEMPO2 uncertainties in the least-significant digits quoted. Upper limits are quoted at the 2σ level. The source position was held fixed at the *Chandra* position.

timing noise is often modelled as

$$\Phi_{TN}(f) = A\left(1 + \frac{f^2}{f_c^2}\right)^{-q/2}, \tag{5.1}$$

where A is the spectral density amplitude, f_c the corner frequency, and q the power-law index (Lasky et al., 2015). A q of 0 represents a white noise power spectrum, whereas indices of 2, 4, and 6 represent random walks in pulse arrival phase, the pulse frequency, and frequency derivative, respectively.

To quantify the probability of timing noise biasing our measurement of the braking index, we conducted a series of simulations that aimed to determine whether any reasonable form of red noise artificially results in a measurement of $n > 3$, given the observed (i.e. white) noise properties of the resulting timing residuals. As timing noise in real pulsars can have PSDs with many indices we created 10^5 realizations of red noise and injected them into simulated pulsar TOAs, with TOA uncertainties, ν, and $\dot{\nu}$ identical to that of the pulsar, but with a braking index of $n = 3$.

To do this we used the `simRedNoise` plug-in of `TEMPO2`. We simulated parameters on a grid, drawing 10 iterations from each set of parameters. We simulated A ranging from 10^{-20}–10^{-18} $\mathrm{s}^2\mathrm{yr}^{-1}$ with 20 log-spaced steps, q between 0–6 with 25 linear steps, and f_c from 10^{-3}–$10^{0.5}$ yr^{-1} in 20 log-space steps. The upper bound on A was chosen to ensure phase connection was possible, as larger values of A precluded phase connection more that 50% of the time, and hence are ruled out by our observations.

After the noise injection, the new TOAs were fitted to the full timing model to measure n, allowing ν, $\dot{\nu}$, and $\ddot{\nu}$ to vary. We considered any iterations where the χ^2 value indicated that a probability of less than 1% ruled out by our measured residuals, as this would indicate unaccounted for noise. After this, only in 0.01% of all the simulations could produce a braking index greater than three with the measured significance. The parameter regime which gave this highest probability of artificially producing a high braking index was when f_c was of order the observing length with the highest values of A. There is only a weak dependence on q, with larger values producing more false positives.

Another way to check for the possible contamination of our measured value of n by timing noise is by considering the third frequency derivative. In our data, the third frequency derivative is consistent with zero at the 1σ level, We ran another suite of simulations within the parameter space described above wherein we fitted up to a third frequency derivative. We note that there is a covariance, with the second and third frequency derivatives being anti-correlated. Only in 0.008% of simulated sets of residuals can we reproduce a braking index significantly greater than three without having a detectable third frequency derivative.

These simulations indicate that only a very low level of timing noise can be present in our data, and the measured braking index of $n = 3.15 \pm 0.03$ is highly unlikely to be due to timing noise. We note that the assumed value of $n = 3$ in our simulations is conservative, since when assuming $n < 3$, it is even less likely for timing noise to result in a measured $n > 3$.

PARKES OBSERVATIONS

In order to search for radio pulsations from PSR J1640–4631, we undertook observations with the 64-m Parkes Telescope[i]. Observations were performed in two sessions totalling 14.96 hours in order to search for pulsations at the position of PSR J1640–4631 (Lemiere et al., 2009). Data were taken by observing with the central beam of the 21 cm Multi-beam receiver, using the BPSR pulsar backend. These observations were taken on 2014 April 18 and 2014 April 27 (MJDs 56765 and 56775, respectively) at centre frequency 1382 MHz over 400 MHz of bandwidth, divided into 1024 channels. The data from each channel were detected and the two polarizations summed to form a time series with 64-μs samples.

We searched these data using the known pulsar spin frequency and frequency derivative from the phase-coherent timing analysis found in this article. We searched over 4704 dispersion measures between 0 and 1600 pc cm^{-3}. No signal was found in these data, and so we quote an upper limit to the pulsar flux at this frequency, using the

---

[i] E. F. Keane performed the Parkes observations, and R. D. Ferdman searched the Parkes data for pulsations.

radiometer equation for the rms noise from the observing system:

$$\sigma_{\rm rms} = \frac{T_{\rm sys}}{G\sqrt{n_p t_{\rm obs} \Delta f}}, \tag{5.2}$$

where $T_{\rm sys}$ is the system temperature in Kelvin, G is the receiver gain in K/Jy, n_p is the number of polarizations, $t_{\rm obs}$ is the total integration time in seconds, and Δf is the observing bandwidth in Hz. From this, we calculate a 3σ upper flux limit of 0.018 mJy at 1.4 GHz. This upper limit assumes a 50% duty cycle, with the upper limit scaling as $\sqrt{DC/(1-DC)}$, where DC is the duty cycle. This flux limit is low, but not unusually so, especially when one considers that the estimated distance to the source is ∼12 kpc.

Discussion & Conclusions

Measurements of braking indices could be contaminated by uncertainties in the pulsar's position, or proper motion (Bisnovatyi-Kogan & Postnov, 1993). The position of PSR J1640–4631 is well determined by *Chandra* to a 3σ error radius of 0.6" (Lemiere et al., 2009). This positional error at the ecliptic latitude of PSR J1640–4631 would add a 1.0 ms root-mean-square signal to our timing residuals, far smaller than our measurement uncertainties. For PSR J1640–4631's estimated distance of 8–13 kpc (Lemiere et al., 2009), and a typical pulsar kick velocity of $300\,\mathrm{km\,s^{-1}}$ (Hansen & Phinney, 1997), an unmodeled proper motion would change the measured braking index by less than one part in a million. Thus neither of these effects can account for our measured braking index.

Another possible contaminant to the measured braking index is a long-term recovery from an unseen glitch prior to our monitoring. If such a glitch occurred, a typical exponential recovery would, in general, cause an artificially high value for $\ddot{\nu}$ to be measured (e.g. Johnston & Galloway, 1999; Hobbs et al., 2010). If we assume an exponentially recovering glitch contaminating a constant braking index we can, from our upper limit of $\ddot{\nu}$, place a lower limit on the decay time scale for such a glitch to be $\tau = 250\sqrt[3]{\Delta\nu_d/10^{-8}\mathrm{Hz}}$ days, where $\Delta\nu_d$ is the size of the unseen decaying glitch. In Yu et al. (2013), of the 107 glitches detected, 27 had a detected exponential recovery. Of those, only 3 were longer than 200 days. We also note that Yu et al. (2013) found that following these 107 glitches, a $\Delta\ddot{\nu}$ was detected in 66 of these and was, within errors, equally likely to be positive or negative. Thus to explain the high braking index as glitch recovery requires an unseen event, an atypically long recovery, and the right sign for the observed n; we cannot rule this out, however it does not seem to us extremely probable, and ultimately this hypothesis can be tested by continued monitoring.

The pulsar's high luminosity PWN has been argued to be powered by a relativistic outflow or wind from the neutron star. Under this assumption, predictions for the pulsar's spin-down history and hence braking index have been made (Gotthelf et al., 2014). The 0.2–10 TeV luminosity of the PWN powered by the source represents $\sim 6\%$ of the pulsar's current spin-down luminosity (Gotthelf et al., 2014). A pulsar whose spin-down is driven solely by a particle wind would result in a braking index of one (Michel, 1969; Manchester et al., 1985). Furthermore, a combination of magnetic dipole radiation and wind braking would result in a braking index with value between one and three. In this case, the braking index as a function of ϵ, the fraction of spin-down power due to a particle wind compared to that from dipole radiation, is given by (Lyne et al., 2015)

$$n = \frac{2}{\epsilon + 1} + 1. \tag{5.3}$$

This implies a maximal expected braking index of n=2.89 for PSR J1640–4631. Indeed, a more thorough modeling of the pulsar and PWN system suggested an even smaller braking index, $n \approx 1.9$ (Gotthelf et al., 2014), clearly at odds with our result.

A changing magnetic field has also been put forth as a possibility for a braking index that is different from three by the growth or decay of the field (Blandford & Romani, 1988; Gourgouliatos & Cumming, 2015), or a change in the angle between the magnetic and rotation axes (Lyne et al., 2013). In this case, n is given by:

$$n = 3 + 2\frac{\nu}{\dot{\nu}}\left(\frac{\dot{B}}{B} + \frac{\dot{\alpha}}{\tan\alpha}\right). \tag{5.4}$$

For the decaying field case, this would imply a magnetic field decay rate of ~ 200 MG per century. This decay rate is very close to that predicted in some magneto-thermal evolutionary models (Viganò et al., 2013), and in this interpretation might be providing direct observational evidence of a decaying magnetic field. On the other hand, population synthesis studies find no strong evidence for field decay in the radio pulsar population as a whole (Faucher-Giguère & Kaspi, 2006).

If a change in the alignment angle between the magnetic and rotational axes is the cause of the anomalous braking index then either α is less than $\pi/2$ and the rotation and magnetic axes are moving towards alignment, or α is greater than $\pi/2$ and the rotation and magnetic axes are counter-aligning. If α is changing on order of the rate of the Crab pulsar (Lyne et al., 2013), the only pulsar for which such a change has been measured, at $\sim 1^\circ$ per century, this would imply that α is $\sim 5^\circ$ away from being an orthogonal rotator. This is at odds with the pulse profile being single peaked, since an orthogonal rotator would typically be seen to have emission as each pole enters our line of sight. In general, the value of α for pulsars can be independently determined by modelling of the gamma-ray or radio pulse profiles. PSR J1640–4631, however, is radio quiet, see §5.2.2. There are also no detected gamma-ray pulsations from PSR J1640–4631 (Gotthelf et al., 2014), and so the value of α remains unconstrained for this source.

Another possibility to explain a braking index greater than three is to invoke higher order multipoles (Pétri, 2015). A pure quadrupole, either a magnetic quadrupole, or a mass quadrupole leading to gravitational radiation (Blandford & Romani (1988), § 1.4.2), would yield a braking index of 5, and could coexist with the magnetic dipole to give a braking index between 3 and 5. Analogous to the case of a wind, the fraction of spin down due to a quadrupole versus a dipole, ϵ_Q is (Palomba, 2000):

$$\epsilon_Q = \frac{n-3}{5-n}. \tag{5.5}$$

In our case, this implies the quadrupolar spin down represents $\sim 8\%$ of the dipolar spin down. In the case of a mass quadrupole, this would imply that the pulsar has an ellipticity of ~ 0.005, which cannot be reproduced by theoretically proposed dense matter equations of state, for a neutron star rotating at 4.84 Hz (Owen, 2005). If such an ellipticity did exist, it would produce gravitational waves having a maximum strain of $\sim 4 \times 10^{-26} \left(\frac{12\mathrm{kpc}}{d}\right)$ at twice the spin-period of the pulsar (Palomba, 2000), which is far below the detection sensitivity of current technology.

The existence of a magnetic quadrupole is in principle testable with future X-ray polarimeter missions. X-ray polarization measurements of neutron stars are in principle sensitive to the magnetospheric configuration, (van Adelsberg & Lai, 2006; Taverna et al., 2014) be it a quadrupolar field structure or a change in the alignment of the spin and magnetic poles. The specific magnetic field structure of pulsars has a strong impact on the inferred magnetic field strength, as well as predicted radio and gamma-ray pulse profiles (Pétri, 2015). Thus X-ray polarimetric observations of PSR J1640–4631 could help us understand the origin of the pulsar's high n, and shed light on the range of possibilities of neutron-star magnetic field structure.

Since the first measurement of the Crab's braking index in 1972 (Boynton et al., 1972), we have known that various physical mechanisms, such as angular momentum loss due to a wind, can result in a pulsar braking index less than the canonical dipole value. Our results for PSR J1640–4631 now show that other physics, such as the quadrupole moment of the magnetic field, affect the evolution of this source, and likely rotation-powered pulsars, in general. Given that two other young, high-magnetic field pulsars have experienced glitches that resulted in a significant drop in the braking index (Archibald et al., 2015b; Antonopoulou et al., 2015), it is clear that continuous study of braking indices provide an important window into additional physical processes at work in the youngest and most energetic of neutron stars.

6

Repeated, Delayed Torque Instabilities Following X-ray Flux Enhancements in the Magnetar 1E 1048.1-5937

The contents of this chapter were first published with the same title in Archibald et al. (2015c).

INTRODUCTION

The X-ray pulsar 1E 1048.1−5937 is part of a small class of neutron stars known as magnetars. 1E 1048.1−5937 has a spin period of $\sim 6.5\,\mathrm{s}$ and a quiescent spin-down rate of $\sim 1\times10^{-11}\,\mathrm{s\,s^{-1}}$ implying a surface magnetic field of $B\sim 3\times10^{14}\,\mathrm{G}$. For more on magnetars, see § 1.5. 1E 1048.1−5937 was monitored regularly with the *Rossi X-ray Timing Explorer* (*RXTE*) from 1998 until its decommissioning in December of 2011 (Dib & Kaspi, 2014). During this monitoring, the source exhibited three long-term flux outbursts; one in 2001, followed by a second in 2002, and a third in 2007 (Dib et al., 2009; Dib & Kaspi, 2014). The first flux outburst was accompanied by magnetar-like bursts from the source (Gavriil et al., 2002). Following both the second and third outbursts, order-of-magnitude variations in $\dot{\nu}$ were reported, but their origin was a mystery (Gavriil & Kaspi, 2004; Dib et al., 2009; Dib & Kaspi, 2014).

Here we report an additional flux outburst in 1E 1048.1−5937 as observed in X-ray timing observations obtained using the *Swift* X-ray Telescope in December of 2011. We show that again, roughly 100 days following the outburst, the pulsar's spin-down rate began showing large variations that are still on-going. We also show evidence of a quasi-periodicity in the torque during these increased spin-down periods. This strongly suggests that such outbursts and long-term torque changes are causally related, and repeatable in this source. In addition, we report on a radio non-detection of the source during this torque enhanced period.

Table 6.1 Summary of observations of 1E 1048.1−5937 used in this work

Telescope	Target ID	Observation Dates	Cadence (days)	Exposure (ks)	No. Obs.
Swift XRT	31220	2011-07-26 – 2013-10-16	14[1]	1.5[2]	188
Chandra ACIS-S	14139	2012-02-23	N/A	6	1
Chandra ACIS-S	14140	2012-04-10	N/A	12	1
ATCA	N/A	2013-03-08	N/A	18	1

[1] This separation was shortened to every 7 days near the maximal torque variations. After each separation, 3 closely spaced observations were taken. See Section 6.2.2 for details.

[2] This is the typical exposure time. Individual observations ranged from 1.1 ks to 7 ks.

OBSERVATIONS AND ANALYSIS

SWIFT XRT

In July 2011, we began a monitoring campaign with the *Swift* XRT (Burrows et al., 2005) of 1E 1048.1−5937, along with five other magnetars. This campaign is a continuation of a long-term monitoring of magnetars conducted with *RXTE* (Dib & Kaspi, 2014). For information on the XRT, please see § 3.3. The XRT was operated in Windowed-Timing (WT) mode for all observations. This gave a time resolution of 1.76 ms. Observations, typically 1.5 ks long, were taken in groups of three, with the first two observations within 8 hours of each other and the third a day later. This observation strategy was adopted due to the source's prior unstable timing behaviour, where maintaining phase coherence using a longer cadence was only possible for several-month intervals (Kaspi et al., 2001; Dib et al., 2009). In all, 188 observations totalling ∼300 ks of observation time were analysed These observations are summarized in Table 6.1.

Level 1 data products were obtained from the `HEASARC` *Swift* archive, reduced using the `xrtpipeline` standard reduction script of `HEASOFT` $v6.16.$, and corrected to the Solar System barycentre using the location of 1E 1048.1−5937, $RA = 10^h50^m07.13^s$, $DEC = -59°53'23.3''$ (Wang & Chakrabarty, 2002). Individual exposure maps, spectrum, and ancillary response files were created for each orbit and then summed. We selected only Grade 0 events for spectral fitting as higher Grade events are more likely to be caused by background events (Burrows et al., 2005).

To investigate the flux and spectra of 1E 1048.1−5937, a 40-pixel long region centred on the source was extracted. As well, a 40-pixel long strip positioned away from the source was used to extract background events.

Timing Analysis

Barycentered events were used to derive a pulse time-of-arrival (TOA) for each observation. The TOAs were extracted using a Maximum Likelihood method as described in § 2.4. The template was derived from taking aligned profiles of all the pre-outburst *Swift* XRT observations and creating a profile composed of the first five Fourier components.

These TOAs were fitted to a timing model as described in § 2.4. To ensure that phase-coherence was maintained over the periods of extreme torque variation, overlapping short-term ephemerides spanning 50 to 100 days were created, and `tempo2` was used to extract pulse numbers. Overlapping segments were compared to ensure that the same number of phase turns existed in overlapping segments between any two consecutive observations. Each of these short, overlapping segments was fitted using `tempo2` to a timing solution with just ν and $\dot{\nu}$, the results of which are presented in Figure 6.1.

This also allowed the extraction of an absolute pulse number for each TOA, allow-

Table 6.2 Timing Parameters for 1E 1048.1−5937

RAJ	10:50:07.13
DECJ	−59:53:23.3
MJD Range	55768-56581
Epoch (MJD)	56000
ν (s^{-1})	0.154782124(9)
$\frac{d\nu}{dt}$(s^{-2})	$-2.43(2) \times 10^{-13}$
$\frac{d^2\nu}{dt^2}$(s^{-3})	$-1.62(8) \times 10^{-20}$
$\frac{d^3\nu}{dt^3}$ (s^{-4})	$-3.6(2) \times 10^{-27}$
$\frac{d^4\nu}{dt^4}$ (s^{-5})	$-1.0(6) \times 10^{-34}$
$\frac{d^5\nu}{dt^5}$ (s^{-6})	$9(2) \times 10^{-41}$
$\frac{d^6\nu}{dt^6}$ (s^{-7})	$5(2) \times 10^{-48}$
$\frac{d^7\nu}{dt^7}$ (s^{-8})	$-2(1) \times 10^{-54}$
$\frac{d^8\nu}{dt^8}$ (s^{-9})	$-1(2) \times 10^{-61}$
$\frac{d^9\nu}{dt^9}$ (s^{-10})	$3(2) \times 10^{-68}$
RMS Residual (s)	1.28
χ^2/dof	10750.85/177

All errors are TEMPO2 reported 1σ errors.

ing the fitting of one phase-coherent solution for the entire data set. This solution is presented in Table 6.2, with the residuals in Figure 6.2. Note that this solution is not a complete description of the spin of the source, as can be seen by the substantial residuals in Figure 6.2, and by the high χ^2/dof in Table 6.2.

As is evident in Figure 6.1, at the time of the flux outburst, we find no evidence for a glitch in ν. The data, however, are consistent with a change in the spin-down

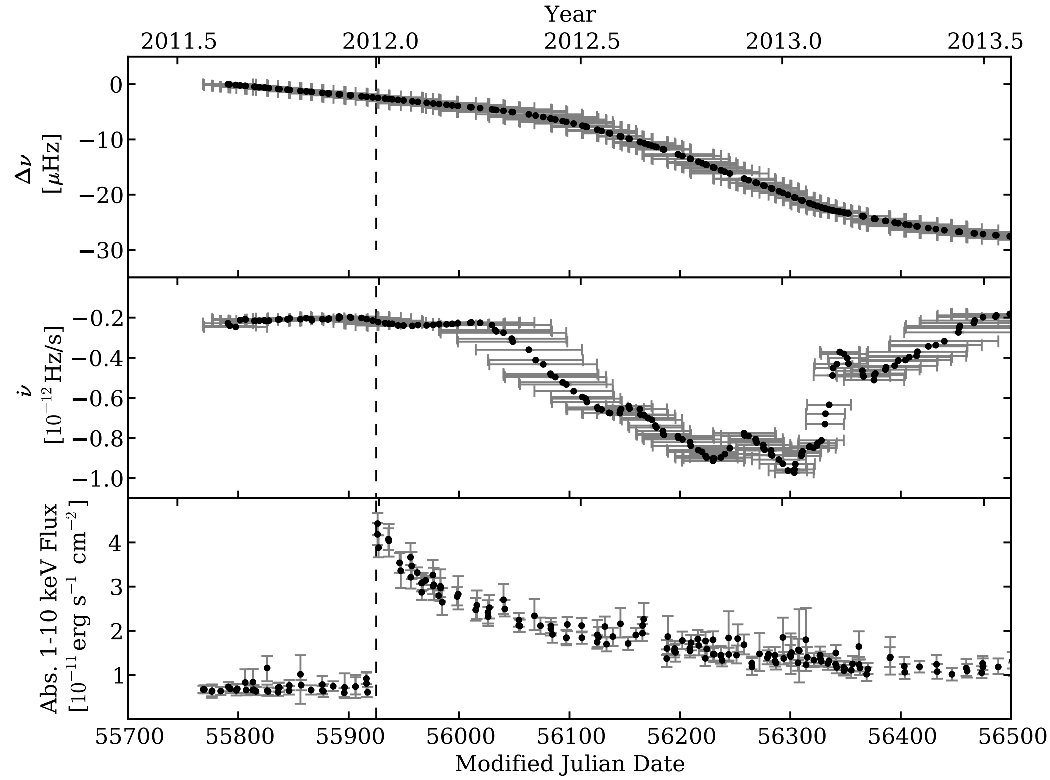

Figure 6.1 Short-term timing parameter evolution of 1E 1048.1−5937 surrounding the December, 2011 outburst. The top panel shows $\Delta\nu$ from the start of the *Swift* monitoring. The second panel shows $\dot{\nu}$. In the top two panels, the horizontal error bars indicate the epoch over which ν and $\dot{\nu}$ were fit. The bottom panel shows the total absorbed 1–10 keV flux. The vertical dashed line indicates the start of the flux outburst.

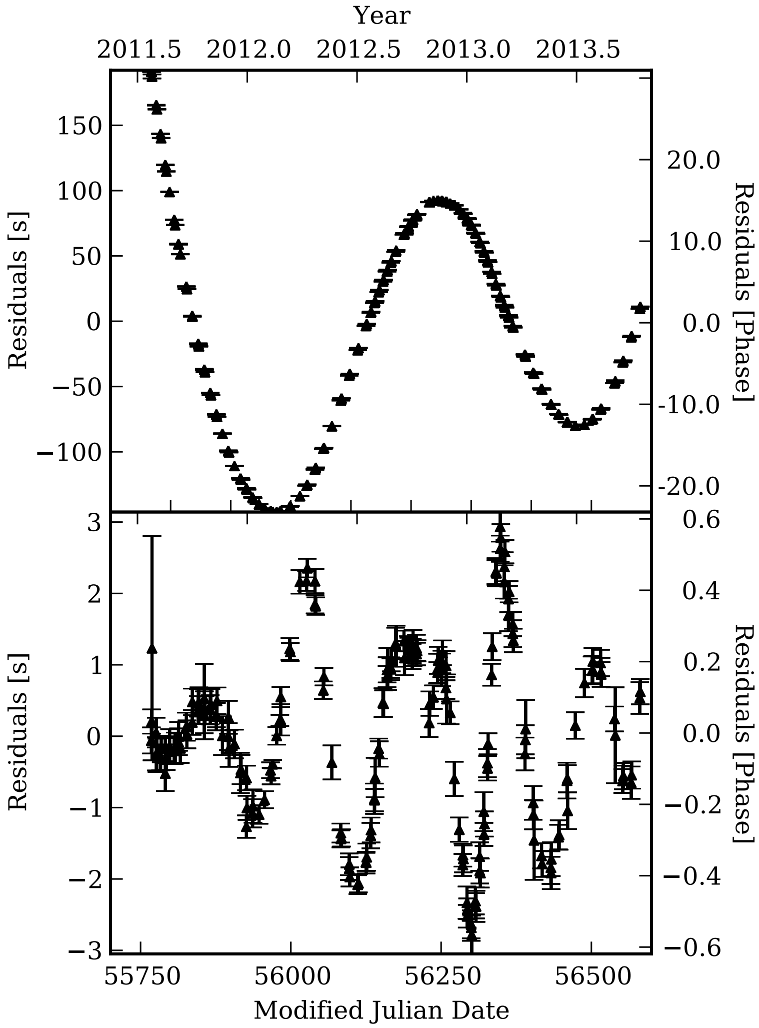

Figure 6.2 Timing residuals of 1E 1048.1−5937 from MJD 55768-56581. The top panel shows residuals with only ν and $\dot{\nu}$ fitted. The bottom panel shows the residuals with 9 frequency derivatives fitted.

rate, $\Delta\dot{\nu} \sim 4 \times 10^{-14}$Hz s^{-1}, a $\sim$ 10% change in torque. The exact amplitude of this change depends strongly on the length of the data span fit, and we are therefore unable to constrain this $\Delta\dot{\nu}$ to a single sudden event.

Approximately 100 days following the peak of the flux outburst, the magnitude of $\dot{\nu}$ began to increase at a rate of $\sim -3 \times 10^{-14}$ Hz s^{-1} day^{-1} for the following 200 days, as seen in the middle panel of Figure 6.1. The spin-down rate continued to fluctuate on weeks to months time scales, with $\dot{\nu}$ changing by up to a factor of 5 in this time frame.

FLUX AND PULSE PROFILE EVOLUTION

Spectra were extracted from the selected regions using `extractor`, and fit using `XSPEC` package version 12.8.2[i]. The spectra were fit with a photoelectrically absorbed power law. We chose to use a single power law in place of the more commonly used power law and blackbody as for a given short observation, the statistics did not warrant a two-component model. Photoelectric absorption was modelled using `XSPEC tbabs` with abundances from Wilms et al. (2000), and photoelectric cross-sections from Verner et al. (1996). A single N_H was fit to all pre-outburst spectra which yielded a best-fit value of $N_H = (1.98 \pm 0.08) \times 10^{22}$ cm^{-2}. For all the fluxes shown in Figures 6.1 and 6.3, N_H was held constant at this value while fitting the spectra. Co-fitting all pre-burst observations (MJDs 55768-55917) yielded $\Gamma = 3.04 \pm 0.07$ with a 1–10 keV absorbed flux of $7.0^{+0.1}_{-0.2} \times 10^{-12}$erg cm^{-2}s^{-1}, with $\chi^2/dof = 505.11/501$.

On MJD 55926 (2011 December 31) the measured 1–10 keV total absorbed flux increased sharply to $(4.4 \pm 0.15) \times 10^{-11}$ erg cm^{-2}s^{-1}, a factor of 6.3±0.2 increase, as seen in Figure 6.1 and 6.3. The source also became harder, with $\Gamma = 2.75 \pm 0.06$

---

[i] http://xspec.gfsc.nasa.gov

for this observation. Between the set of observations on MJD 55926 (2011 December 31) and the next set on MJD 55936 (2012 January 6), the flux fell to $(3.8 \pm 0.2) \times 10^{-11}$ erg cm^{-2}s^{-1}. After this initial decay, the 1–10 keV flux decay is well described ($\chi^2/dof = 132.3/132$) by an exponential decay: $F = [0.7^{+0.1}_{-0.2} + (2.8 \pm 0.3)e^{-(t-t_0)/(260\pm30)}] \times 10^{-11}$ erg s^{-1}cm^{-2} where t and t_0 are in units of days. t_0 was held fixed at MJD 55926, the peak of the outburst. The pulsed fraction displayed in Figure 6.3 is the root mean squared (RMS) pulsed fraction, as described in Woods et al. (2004). The clear correlation between the power law index and the measured 1–10 keV total absorbed flux apparent in Figure 6.3 is typical for magnetar outbursts; see e.g. Scholz & Kaspi (2011).

For the 9 days between the prior *Swift* monitoring observation on MJD 55917 and the observation on MJD 55926 which had an enhanced flux,we detect no significant emission in the *Swift* Burst Alert Telescope. We can place an upper-limit on the 15-50 keV emission of 7.5×10^{-5} counts s^{-1} cm^{-2} ($\sim 7 \times 10^{-12}$ erg cm^{-2}s^{-1}).[ii] This limit indicates that the majority of the energy of this outburst is in the long exponentially decaying tail, rather than in a missed sharp peak.

In Figure 6.5, the pulsed component of the flux of 1E 1048.1−5937 is presented for the three long-term flux outbursts observed from this source. The pulsed flux does not follow the fast rise seen in the total flux; instead we see a several weeks long rise in the pulsed flux before it begins to decay. The *Swift* observations, where we can measure both pulsed and total flux, suggest that the slow rise times in the prior outbursts observed with *RXTE* (Dib et al., 2009) are a result of *RXTE* being only sensitive to the pulsed flux from the source. An anti-correlation between total flux and pulsed fraction has been reported for this source during previous outbursts (Tiengo

---

[ii] Hans Krimm, private communication.

et al., 2005; Tam et al., 2008). In particular Tam et al. (2008) fit the relation to a power law $P_F \propto F_x^n$ with index -0.46 ± 0.02. While this provides an adequate description of the pulsed fraction at most epochs, it overestimates the pulse fraction at the peak epoch by a factor of ~ 3.

To monitor for changes in the pulse profile of 1E 1048.1−5937, we created a high signal-to-noise 16-bin template by aligning all quiescent *Swift* XRT observations using the TOA offsets from the ML procedure described above. For each observation, a phase-aligned profile was created using the current timing ephemeris. The best-fit DC level was then subtracted from each profile, and the latter was scaled to match the template using a multiplicative scaling factor which minimized the reduced χ^2 of the difference between the scaled profile and the template. The reduced χ^2 values are presented in Figure 6.4. We note that the first observation following the outburst is inconsistent with the template profile at the $3\,\sigma$ level. All other individual profiles are consistent with the template at the $3\,\sigma$ level, however there is a marked increase in the average reduced χ^2 at the time of the flux increase.

Motivated by the increase in the average reduced χ^2 near the outburst, we looked for lower-level changes in the pulse profiles. Nearby observations were combined to create higher signal-to-noise profiles. These background-subtracted normalized 1–10 keV profiles can be seen in Figure 6.4. With these higher signal-to-noise profiles, we note low-level changes in the pulsed profiles, however the dominant change apparent is the large change in the pulsed fraction.

Chandra

Following the detection of the flux increase with the *Swift* monitoring campaign, a set of two *Chandra* Target of Opportunity observations were triggered in Continuous

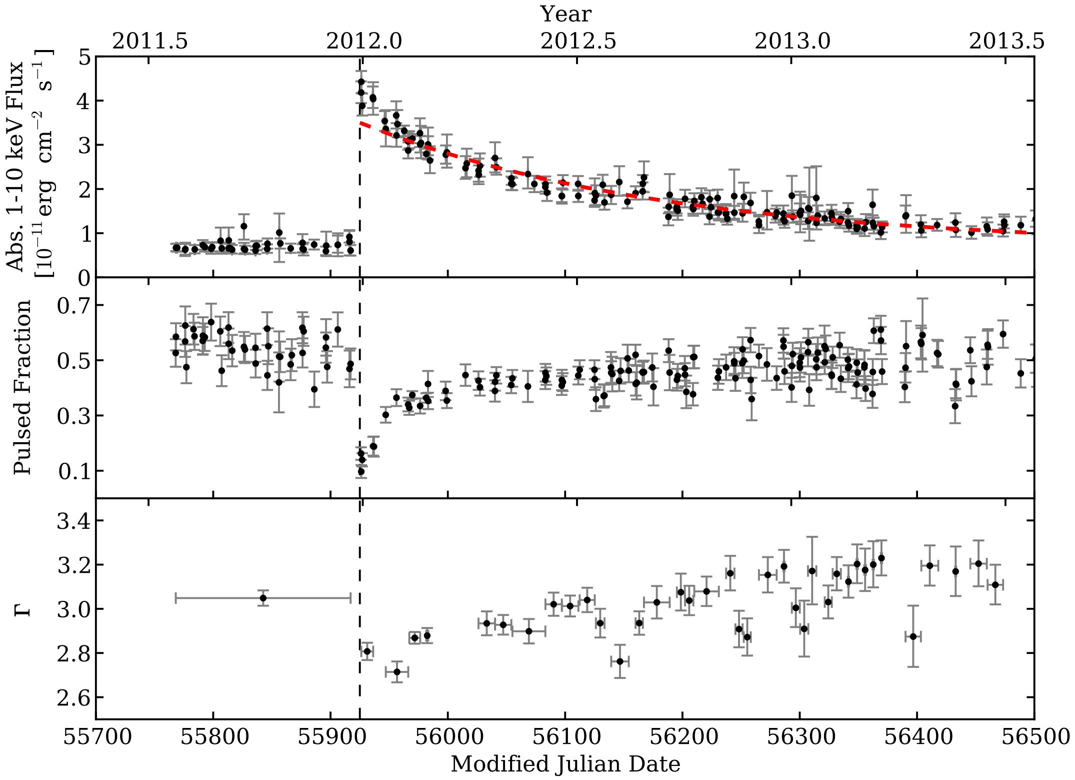

Figure 6.3 Flux evolution of 1E 1048.1−5937. The top panel shows the total absorbed 1–10 keV flux, with the dashed line the fit to the post-burst flux decay, $F = [0.7^{+0.1}_{-0.2} + (2.8 \pm 0.3)e^{-(t-t_0)/(260\pm30)}] \times 10^{-11}$ erg s^{-1}cm^{-2}, where t is in days. The middle panel shows the RMS pulsed fraction, and the bottom panel, the power law index Γ, fit to the epochs indicated by the horizontal error bars. The vertical dashed line indicates the start of the flux outburst.

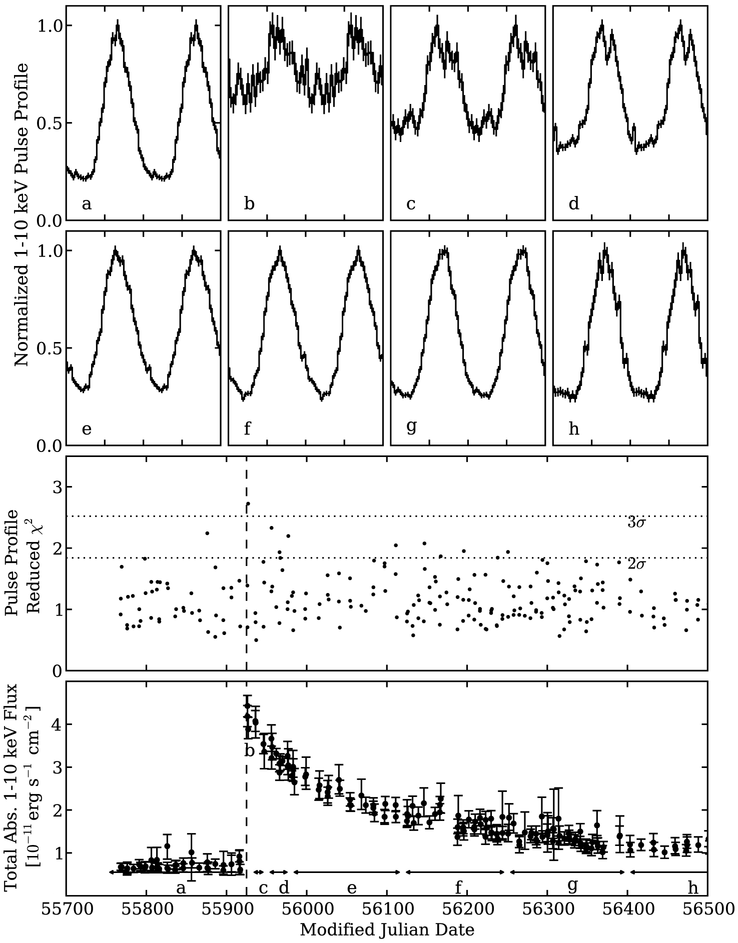

Figure 6.4 Normalized 1-10 keV pulse profiles for 1E 1048.1−5937 around the 2012 outburst. The lettered panels at the top are the normalized background-subtracted pulse profiles summed over the time spans indicated by the arrows in the bottom panel. The profile b is from the observations at peak flux on MJD 55926. The middle panel shows the reduced χ^2 statistic calculated after subtracting the scaled and aligned profiles of the individual observations from a high signal-to-noise template. The lower and upper dotted lines correspond to $2\,\sigma$ and $3\,\sigma$ significance, respectively. In the lower two panels, the vertical dashed lines indicated the start of the flux outburst. To calculate the flux, N_H was held constant at $1.98 \times 10^{22}\,\mathrm{cm}^{-2}$; see § 6.2.3.

Table 6.3 *Chandra* spectral fits of 1E 1048.1−5937[1].

Date	Exposure (ks)	kT (keV)	Γ	Abs. 1-10 keV Flux (10^{-12} erg cm^{-2} s^{-1})
2012-02-23	6	0.624 ± 0.007	$2.47^{+0.17}_{-0.22}$	$27.5^{+0.3}_{-1.7}$
2012-04-10	12	$0.573^{+0.06}_{-0.07}$	$2.29^{+0.17}_{-0.22}$	$23.4^{-0.4}_{-1.6}$

[1] N_H was co-fit to both observations simultaneously, yielding $N_H = 1.29^{+0.09}_{-0.1} \times 10^{22}\,\mathrm{cm}^{-2}$

Clocking mode using *ACIS-S*. The data were processed using CIAO 4.5 and CALDB 4.5.7. Data were reprocessed using `chandra_repro` and corrected to the Solar System barycentre using the `axbary` tool.

To study the flux and spectra, a 6" long-strip centred on the source was extracted as well as a background strip of total length 400"-located away from the source. For the *Chandra* data, the two spectra were co-fit with a single N_H, with all other parameters free. The results of this fit can be seen in Table 6.3. We note that the N_H presented here appears inconsistent with that of Mereghetti et al. (2004) and Tam et al. (2008). This is due to a difference in the model used for photometric absorptions, as well as the values used for solar abundances and cross sections. We can obtain a N_H consistent with the previously reported values by fitting with the solar abundances and cross sections used by Tam et al.

The pulse profiles obtained from the *Chandra* data are consistent with those presented from the *Swift* data.

AUSTRALIA TELESCOPE COMPACT ARRAY

We performed a search for radio emission using the Australia Telescope Compact Array (ATCA)[iii]. The observation was made on 2013 Mar 4 in the 6A array configura-

---

[iii] C.Y. Ng proposed for & analysed the Australia Telescope Compact Array data.

tion with a total integration time of 5 hr. The central frequency was 2.1 GHz with a bandwidth of 2 GHz. The flux density scale was set by observations of the primary calibrator, PKS B1934−638. A secondary calibrator, PKS B1049−53, was observed every 40 min to determine the antenna gains.

We carried out all data reduction with the MIRIAD package[iv]. After standard flagging and calibration, an intensity map was formed using the multi-frequency synthesis technique with natural weighting, then deconvolved using a multi-frequency CLEAN algorithm (`mfclean`), and restored with a Gaussian beam of FWHM $7.5'' \times 5.1''$. The final image has rms noise of 0.06 mJy beam^{-1}. We note that this is a few times higher than the theoretical limit of 0.015 mJy beam^{-1}, due to the side-lobe of an extended extragalactic source G288.27−0.70 (Brown et al., 2007) $10'$ to the south west We found no source at the position of 1E 1048.1−5937. This yields a 3σ flux density limit of 0.2 mJy at 2.1 GHz. This corresponds to a $L_{2.1GHz}/L_{1-10keV} < 4 \times 10^{-7}$ at the epoch of the observation. Magnetars are highly variable in the radio, for example, in the case of the magnetar XTE J1810−197 $L_{1.4GHz}/L_x$ varies from 7×10^{-3} to less than 7×10^{-5} (Camilo et al., 2007). Other magnetars also show orders of magnitude variations in their radio luminosity; see Olausen & Kaspi (2014) and references therein.

Previous searches for radio emission from this source have also resulted in non-detections. A 3σ flux density limit of 0.11 mJy at 1.4 GHz (Burgay et al., 2006) in 1999 was found when the source was spinning down steadily. Also the source was not detected in a pulsation search ∼15 days after the 2007 glitch, for a period-averaged flux density limit at 1.5 GHz of 0.1 mJy (Camilo & Reynolds, 2007).

[iv] `http://www.atnf.csiro.au/computing/software/miriad/`

DISCUSSION

We have presented *Swift* XRT and *Chandra ACIS-S* observations of 1E 1048.1−5937 which show a sudden factor of 6.3 ± 0.2 increase in the total $1-10$ keV X-ray flux on MJD 55926 (2011 December 31). This flux showed different evolution in the pulsed versus total flux, with the total flux rising sharply, and the pulsed flux showing a slow rise on a ∼weeks time scale. This flux increase was followed, after a ∼ 100 day delay, by a months-long torque increase. We also report an upper limit of 0.2 mJy at 2.1 GHz using the Australia Telescope Compact Array during this period of torque enhancement.

1E 1048.1−5937 displays a strong anti-correlation between the total X-ray flux, and the pulsed fraction, as can be seen in Figure 6.3. Similar anti-correlations between X-ray flux and pulsed fraction have been reported during other several magnetar outbursts (e.g. Israel et al., 2007; Ng et al., 2011; Rea et al., 2013). This suggests that at the time of outbursts, energy is being injected into the magnetar isotropically, eg. across the entire surface or magnetosphere rather than being injected at one point.

1E 1048.1−5937 has shown similar behaviour in the past, with large pulsed flux outbursts in 2001, 2002, and 2007 (Gavriil & Kaspi, 2004; Dib et al., 2009; Dib & Kaspi, 2014). All of these pulsed flux outbursts have similar increases in the 2-10 keV pulsed flux with a factor of 2.3 ± 0.2, 2.9 ± 0.1, 3.1 ± 0.1, and 3.3 ± 0.2 for the four outbursts. We note that for the three outbursts which are followed by extreme torque variation, the pulsed flux increases are consistent with each other, and are larger than in the outburst in 2001. In Figure 6.5, we show these outbursts along with the most recent flux outburst reported here. For the 4500 days of data examined in this work, 42 ± 6 % of the pulsed X-ray emission from the source has been due to these pulsed

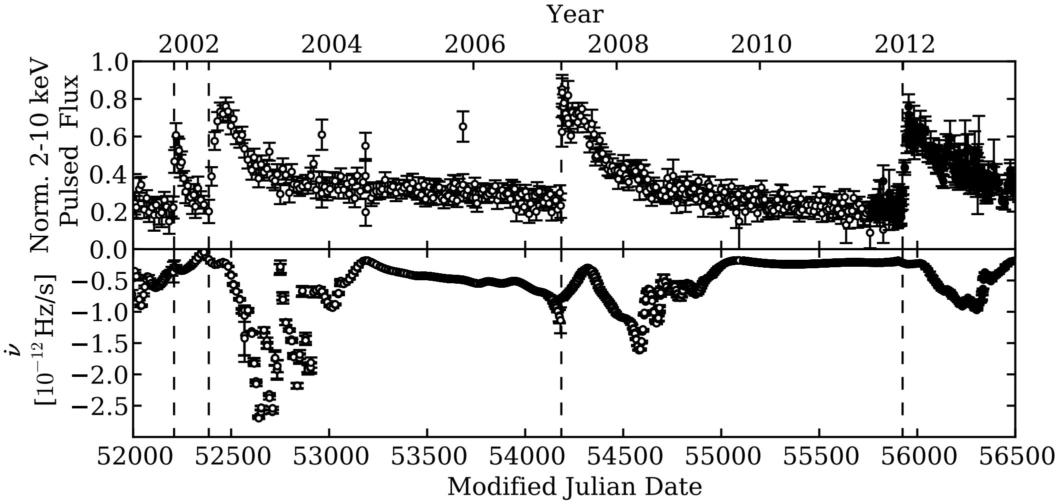

Figure 6.5 Pulsed flux and $\dot{\nu}$ evolution for 1E 1048.1−5937. The top panel shows the normalized 2–10 keV pulsed flux. The bottom panel shows $\dot{\nu}$. The dashed lines indicate the start times of the pulsed flux outbursts. In both panels, *RXTE* data are hollow points, and *Swift* data are solid points. *RXTE* data are from Dib & Kaspi (2014).

flux flares, and the remainder due to its baseline flux.

The possible hint of periodicity in the three largest flux enhancements, is not strict: the times between the pulsed flux outbursts are 180 ± 10, 1800 ± 10, and 1740 ± 10 days, respectively. This variation by $\sim$3% after just 3 cycles immediately precludes a binary-companion-related origin, wherein a strict periodicity would be expected. On the other hand, the reality of the possible periodicity is supported by its being observed independently in the flux evolution and in the torque evolution.

The extreme variation in $\dot{\nu}$ has become smaller with each subsequent outburst: reaching minimum values of $(-2.70 \pm 0.01) \times 10^{-12}$ Hz s^{-1}, $(-1.61 \pm 0.01) \times 10^{-12}$ Hz s^{-1}, and $(-0.97 \pm 0.01) \times 10^{-12}$ Hz s^{-1} for the three outbursts. For comparison, the longest pseudo-stable spin-down rate is -2.2×10^{-13} Hz s^{-1}. In all three cases

$\dot{\nu}$ does not evolve symmetrically, rather it seems to increase nearly monotonically then decay back to the nominal spin-down value in an oscillatory manner. This can seen more clearly in Figure 6.6, where the $\dot{\nu}$ variations are shown in days from the detected flux increase. To characterize the oscillations visible in $\dot{\nu}$ following the pulsed flux increases, we calculated a power spectrum of the observed $\dot{\nu}$, shown in Figure 6.7. We note broad peaks at 64 ± 4, 96 ± 10, and 200 ± 20 days.

The origin of the observed possibly periodic flux enhancements and subsequent spin-down rate variations is puzzling. A periodicity in spin period on comparable time scales was predicted by Melatos (1999) for this source in particular; this was suggested to result from the deformation of the neutron star from sphericity due to the high B field, causing Eulerian precession. Thompson et al. (2000) also considered magnetar precession; they and Melatos (1999) predicted strictly periodic behaviour, not the more intermittent nature observed in 1E 1048.1−5937 wherein the pulsar goes for several years with relatively stable spin down. Apart from the only approximately periodic nature of the behaviour not agreeing with the precession models, X-ray outbursts are similarly not predicted in such models, and certainly no clear phase delay in a quasi-cycle between spin and flux behaviour was predicted. Moreover, Shaham (1977) suggested that neutron-star precession with period τ_p requires that the moment of inertia of any pinned crustal superfluid, such as that invoked to explain glitches like those seen ubiquitously in magnetars (e.g. Dib et al., 2008; Dib & Kaspi, 2014), not exceed a fraction P/τ_p of that of the neutron star – far smaller than has been inferred for both magnetars and radio pulsars. No such long-term quasi-periodicities have been predicted or discussed in any other magnetar paper, nor in any disk model, to our knowledge.

However we note that quasi-periodicities in spin-down rate have been reported

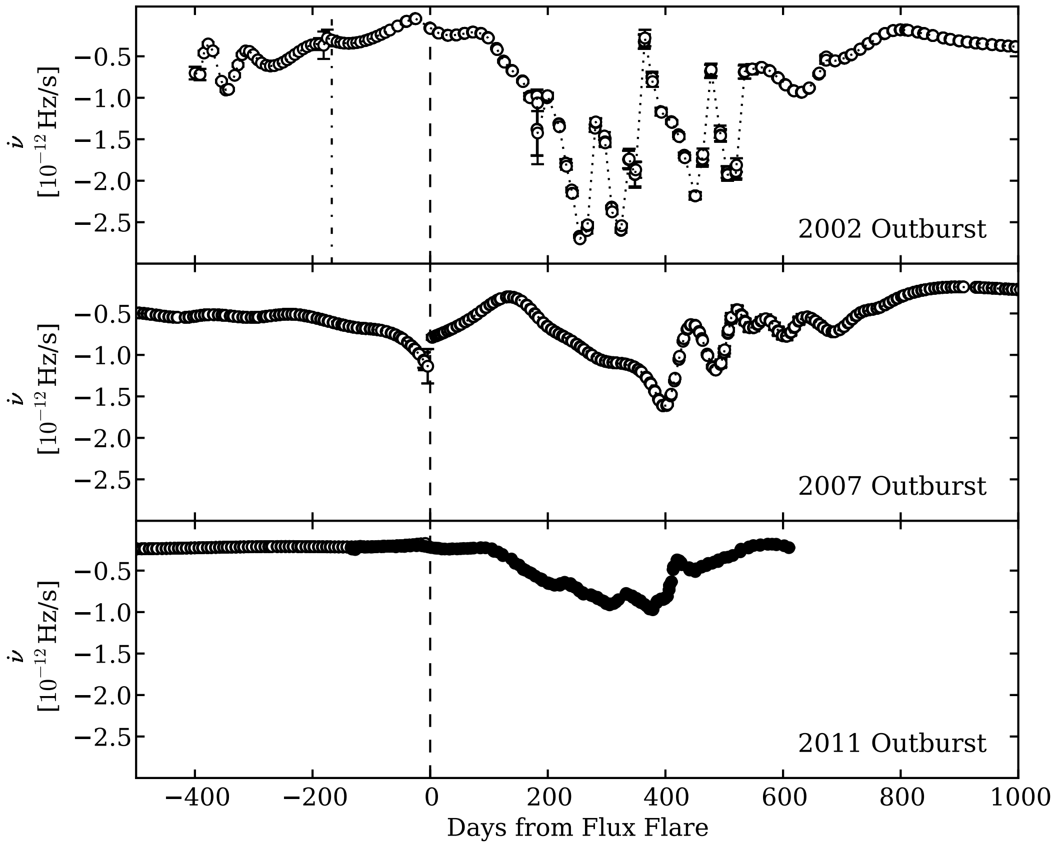

Figure 6.6 $\dot{\nu}$ evolution for 1E 1048.1−5937 following each flux increase. The dashed lines indicate the start times of the pulsed flux outbursts, with the dot-dash line in the top panel indicating the precursor flare in 2001. *RXTE* data are hollow points, and *Swift* data are solid points. *RXTE* data are from Dib & Kaspi (2014).

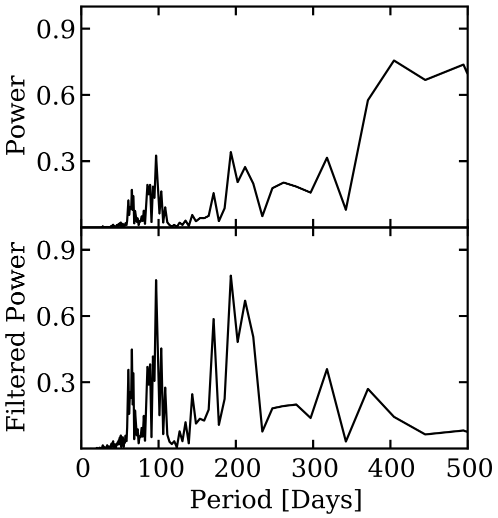

Figure 6.7 Normalized power spectrum of $\dot{\nu}$ for 1E 1048.1−5937 over 12 years. The top panel is red-noise unfiltered, and the bottom panel has been passed through a high-pass filter. See Section 6.3 for details.

on very similar time scales in radio pulsars by Lyne et al. (2010). Those authors reported on long-term monitoring of 366 radio pulsars using the Lovell Telescope at Jodrell Bank, finding at least 17 sources to show clear, substantial and generally quasi-periodic changes in $\dot{\nu}$ in data sets over 20 years long. The quasi-periodicities ranged in time scale from months to years depending on the source, and in at least six cases, were clearly correlated with changes to the radio pulsars' average profiles. Notably, Lyne et al. (2010) observed that in those six cases, the $\dot{\nu}$ and the pulse morphology, appeared in two or more distinctly preferred 'states.' Because of the strong correlation between the spin-down evolution and radio pulsar shape changes, Lyne et al. (2010) concluded the behaviour must have its origin in the stellar magnetosphere, and observationally ruled out previous suggestions that it could be free precession (Stairs et al., 2000), which again, appeared challenging to understand theoretically (Shaham, 1977). Moreover, apparent evolution in the magnetic field structure has also been seen in the Crab pulsar (Lyne et al., 2013), further suggesting this behaviour is ubiquitous in radio pulsars.

In 1E 1048.1−5937, we find behaviour that appears in many way similar to that of the radio pulsars studied by Lyne et al. (2010): quasi-periodic spin-down on time scales of several years, with two apparently distinct 'states,' one fairly steady, and one quasi-oscillatory. These are clearly correlated with radiative changes, in this case in the form of enhanced X-rays, whose origin can be explained by magnetospheric twists which result in enhanced return currents that cause the observed spectrum to harden with increased flux (Thompson et al., 2002; Beloborodov & Thompson, 2007; Beloborodov, 2009).

The magnitude of the spin-down-rate changes in 1E 1048.1−5937 is much larger than in the Lyne et al. (2010) objects. In those cases though typical values of $\Delta\dot{\nu}/\dot{\nu}$ were ∼1%, although a value of 45% was observed in one source (see also Kramer et al., 2006). The latter is still much smaller than the factor of > 10 changes we have observed in 1E 1048.1−5937 (Gavriil et al., 2004). However given independent conclusions about the greatly enhanced activity in magnetar magnetospheres, on the basis of their radiative behaviour overall (bursts, long-term flux enhancements, etc), it is perhaps unsurprising that the magnitude of the analogous $\dot{\nu}$ effect in a magnetar should be much larger than that in conventional radio pulsars. This suggests there could be a greater tendency for higher-B radio pulsars to show magnetospheric evolution as manifested by radio pulse variations and/or spin-down fluctuations. However, in the 18 pulsars presented by Lyne et al. (2010), there is no such correlation seen between magnetic field strength and $\dot{\nu}$ variation.

In the case of 1E 1048.1−5937, these epochs of extreme torque variability dominate the average spin-down of the magnetar. If we take the difference in the spin frequency at the start and end of the data presented in this work, MJD 52000-56500, we measure an average spin-down rate of approximately $-5.5 \times 10^{-13}\,\mathrm{Hz\,s^{-1}}$. This is a factor of ~ 2.5 higher than the quiescent spin-down of $-2.2 \times 10^{-13}\,\mathrm{Hz\,s^{-1}}$ measured during the least active period in 2010 and 2011.

The apparent absence thus far of similar behaviour in other magnetars could possibly be understood as being due to the same mechanism that causes such a variety of periodicity time scales in the Lyne et al. sources. Longer-term quasi-periodicities may eventually become apparent in other magnetars. If radio pulsations were one day to be observed from 1E 1048.1−5937 in spite of strong upper limits as reported both here and elsewhere (Burgay et al., 2006; Camilo & Reynolds, 2007), we would predict correlated changes with spin-down rate. However, this may never be observed, if only due to unfortunate beaming (e.g. Lazarus et al., 2012).

The observed delay between the X-ray outbursts and $\dot{\nu}$ 'state' changes has already been considered by Beloborodov & Thompson (2007). As also discussed by Timokhin (2010) but in the context of conventional radio pulsars, a time delay is expected between when the twist forms near the neutron-star crust, and when it reaches the outer magnetosphere, where the impact on the spin-down rate manifests. This time delay is suggested by Beloborodov & Thompson (2007) to be due to the spreading time of twist current across magnetic field lines, a result of magnetospheric coronal resistivity, and its value is predicted to be highly geometry-dependent. This argues that the events that trigger the flux enhancements in 1E 1048.1−5937 must consistently be in the same approximately region of the neutron-star surface, and likely far from the poles, where little delay is expected. Likely then the monotonic decline in the amplitude of the torque variations seen in the three cycles observed so far is a coincidence, and future cycles may yet again exhibit order-of-magnitude torque changes.

Indeed if the apparent quasi-periodicity is real, we expect the next X-ray flux outburst cycle to occur in late 2016, with the next cycle of $\dot{\nu}$ oscillations a few months later. Future X-ray telescopes will easily observe this behaviour, should it occur. Moreover, continued long-term monitoring of other magnetars may yet reveal similar behaviour, though the Jodrell Bank work underscores the need for systematic monitoring over decades.

Conclusions

We have reported on long-term systematic monitoring of the magnetar 1E 1048.1−5937 using the *Swift* X-ray Telescope. This monitoring has revealed:

(1) Evidence for quasi-periodic X-ray outbursts, each of comparable amplitude, roughly a factor of $\sim$ 3 above the typical pulsed level, with approximate recurrence time scale $\sim$1800 days. Considering three events observed thus far, the difference in separation between the first and second two was $\sim$3% smaller than between the second and third[v].

(2) Similar periodicity is seen in the evolution of $\dot{\nu}$ on the same time scale; every $\sim$1800 days, $\dot{\nu}$ commences fluctuating with quasi-oscillatory behaviour on time scales of $\sim$100 days, with amplitude changes as large as an order of magnitude, such that the neutron star is always spinning down. The fluctuations at each cycle are not identical but are similar in time scale.

(3) Though the flux and $\dot{\nu}$ both appear periodic with the same repetition rate, there is a clear delay between the two such that the $\dot{\nu}$ variations begin $\sim$100 days after the

---

[v] We have since detected a new outburst of this source that is consistent with this quasi-periodicity; see Chapter 9.

flux outburst begins.

(4) The maximum amplitude of the $\dot{\nu}$ oscillations has declined monotonically over the observed three cycles.

(5) The spin-down is relatively stable between episodes of $\dot{\nu}$ fluctuation.

(6) Aside from the extreme variation in $\dot{\nu}$ always beginning after an X-ray outburst, there is no correlation between the X-ray luminosity and $\dot{\nu}$.

Although similar quasi-periodic radiative and torque behaviour has not yet been reported in other magnetars, similar, though lower amplitude, behaviour has been seen in radio pulsars (Lyne et al., 2010), and appears to implicate processes in the stellar magnetosphere rather than, for example, precession. Continued long-term monitoring of both source classes is warranted, to see if, for example, there is a greater tendency for such phenomena in more highly magnetized objects.

7

Swift observations of two outbursts from the magnetar 4U 0142+61

The contents of this chapter were first published with the same title in Archibald et al. (2017b).

INTRODUCTION

4U 0142+61 has the highest persistent X-ray flux of the known magnetars. For more on magnetars, see § 1.5. It was discovered as a point-source by the *Uhuru* mission (Giacconi et al., 1972), and later revealed to be a ∼8.7 s pulsar (Israel et al., 1994).

With a spin period of $\sim 8.7\,\mathrm{s}$ and a quiescent spin-down rate of $\sim 2 \times 10^{-12}\,\mathrm{s\,s^{-1}}$, 4U 0142+61 has an inferred dipole surface magnetic field of $1.3 \times 10^{14}\,\mathrm{G}$.

4U 0142+61, along with several other magnetars, was monitored regularly with the *Rossi X-ray Timing Explorer (RXTE)* in 1997, and from 2000 until the decommissioning of *RXTE* in 2011 December (Dib & Kaspi, 2014). During this campaign 4U 0142+61 showed a slow rise in pulsed flux accompanied by pulse profile changes from 2000–2006 (Dib et al., 2007). Most notably, in 2006, 4U 0142+61 entered an active phase – emitting at least six short magnetar-like bursts, and exhibiting a glitch with an over-recovery, leading to a net spin-down of the neutron star (Gavriil et al., 2011a). On 2011 July 29, 4U 0142+61 had large spin-up glitch (Dib & Kaspi, 2014). This glitch was accompanied by a short hard X-ray burst detected by the *Swift* Burst Alert Telescope (BAT) (Gavriil et al., 2011b).

Compared to the other long-term *RXTE*-monitored magnetars, 4U 0142+61 is relatively quiet in terms of timing behaviour Aside from the aforementioned glitches, the rotational evolution is well described by a low-order polynomial, a statement which cannot be made for any of the other sources in the *RXTE* monitoring campaign (Dib & Kaspi, 2014).

Here we present the results of a continued monitoring campaign of 4U 0142+61 using the *Swift* X-ray Telescope from 2011 July to 2016 June. We report on two X-ray outbursts on 2011 July 29 and 2015 February 28, both associated with timing anomalies. We find that the timing anomaly associated with the X-ray outburst on 2015 February 28, similar to the 2006 event, led to a net spin-down of 4U 0142+61. We also find a long-term X-ray flux decay following both timing events, as well as 12 XRT-detected magnetar-like bursts which occurred coincident with the second timing event.

OBSERVATIONS AND ANALYSIS

Swift X-RAY TELESCOPE

We began observing 4U 0142+61 with the *Swift* XRT on 2011 July 26 as part of a campaign to monitor several magnetars (see e.g. Scholz et al., 2014a; Archibald et al., 2015c).

For information on the XRT, please refer to § 3.3. The XRT was operated in Windowed-Timing (WT) mode for all observations, having a time resolution of 1.76 ms, at the expense of one dimension of spatial resolution.

Level 1 data products were obtained from the `HEASARC` *Swift* archive, reduced using the `xrtpipeline` standard reduction script, and time corrected to the Solar System barycentre using the position of 4U 0142+61 (Hulleman et al., 2004), and `HEASOFT v6.17`. Individual exposure maps, spectrum, and ancillary response files were created for each orbit and then summed. If, in an individual orbit, the centre of the source was within three pixels of a dead column, or the edge of the chip, that orbit was excluded from flux and spectral fitting. We selected only Grade 0 events for spectral fitting as other event Grades are more likely to be caused by background events (Burrows et al., 2005). We also removed many detected soft X-ray bursts which appear in both the source and background region, as these bursts must be instrumental in origin.

To investigate the flux and spectral evolution of 4U 0142+61, a 10-pixel radius circle centred on the source was extracted. As well, an annulus of inner radius 75 and outer radius 125 pixels centred on the source was used to extract background events.

Swift XRT spectra were extracted from the selected regions using `extractor`, and fit using `XSPEC` version 12.8.2[i]. Photons were grouped to ensure one photon was in each spectral bin. As the background dominates the source below 0.7 keV, we use photons from only the 0.7–10-keV band for spectral fitting. In total, 127 XRT observations totalling 475 ks of observing time were analysed in this work.

Timing Analysis

Following the processing described in §7.2.1, we derived an average pulse time-of-arrival (TOA) for each observation. To maximize the signal-to-noise ratio for obtaining TOAs for the source, photons from 0.7-10 keV were used in the timing analysis. The TOAs were extracted using a Maximum Likelihood (ML) method as described in § 2.4. The ML method compares a continuous model of the pulse profile to the photon arrival phases obtained by folding a single observation.

These TOAs were fitted to a standard pulsar timing model as described in § 2. This was done using the `tempo2` (Hobbs et al., 2006) pulsar timing software package.

As we have only one *Swift* observation before the 2011 glitch on MJD 55771.19 (Dib & Kaspi, 2014) we present a timing solution starting at MJD 55771.9, the first XRT observation following the aforementioned glitch. We note that the timing solution presented by Dib & Kaspi (2014) accurately describes our measured TOAs in the overlapping region.

We present a fully phase-coherent timing solution in Table 7.1. The basic timing solution provides an accurate description of the TOAs until MJD 57079.7. At this date we require a change in the spin parameters to accurately describe the TOAs. We fit for a glitch with both permanent and decaying parameters wherein the spin

---

[i] `http://xspec.gfsc.nasa.gov`

Table 7.1 Phase-Coherent Timing Parameters for 4U 0142+61.

Dates (MJD)	55771.54 - 57551.22
Dates	29 July 2011 - 12 June 2016
Epoch (MJD)	57000.00000
ν (s^{-1})	0.115 085 312 4(3)
$\dot{\nu}$ (s^{-2})	$-2.621(2)\times10^{-14}$
$\ddot{\nu}$ (s^{-3})	$8(3) \times 10^{-25}$
Glitch Parameters	
Glitch Epoch	57081.21605 (fixed)
$\Delta\nu$ (s^{-1})	$-3.7(1) \times 10^{-8}$
$\Delta\nu_d$ (s^{-1})	$5.1(5) \times 10^{-8}$
τ_d (days)	57(9)
rms residual (s)	0.118
rms residual (phase)	0.014

Figures in parentheses are the nominal 1σ TEMPO2 uncertainties in the least-significant digits quoted.

frequency after the glitch epoch, t_g, can be described as:

$$\nu(t) = \nu_t + \Delta\nu + \Delta\nu_d e^{-(t-t_g)/\tau_d} \tag{7.1}$$

where ν_t is the predicted spin frequency pre-glitch, $\Delta\nu$ is a permanent change in the spin frequency, and $\Delta\nu_d$ is an exponentially decaying change in the spin frequency decaying with a time scale of τ_d days. This glitch is coincident with the 2015 February 28 BAT detection, and short-term X-ray flux increase (see Barthelmy et al., 2015) and § 7.4.2.

Due to pulse shape variations, for the three observations immediately following the 2015 outburst –those occurring on MJDs 55782.6, 57084.1, and 57087.5, our ML TOA extraction method indicated that these 3 TOAs were 0.43 phase turns out of phase with all the surrounding TOAs. The profiles can be seen in Figure 7.1. This offset is consistent with the distance between the two peaks in the standard profile. We therefore exclude these three TOAs from our timing analysis. The full timing solution is presented in Table 7.1. The timing residuals, the difference between the modelled and observed TOAs, can be seen in Figure 7.2. We note that these three suspect TOAs are in phase with each other, and that if we shift them by the time between the two profile peaks, and include them in our glitch fitting procedure, they have little effect ($\sim 1\sigma$) on the reported parameters.

We emphasize that the net spin-*down* glitch properties are most affected by the TOAs long after the outburst, far away from the period of strong profile changes. To illustrate the difference in the inclusion of the suspect profiles, in Figure 7.2 we present the evolution of ν over the *Swift* campaign. To generate this Figure, we fit splines to the pulse numbers (see Dierckx, 1975), using a method similar to that described in Dib & Kaspi (2014) using piecewise polynomials of degree $n = 3$ weighted by the inverse square error on the pulse number. To generate the error bounds, we added Gaussian noise with standard deviations of the measured TOA uncertainties to these pulse numbers 1000 times, and refit the splines. The plotted error band shows the 68% confidence region. Note that while in this semi-coherent solution a spin-up glitch is not required when excluding the three suspect TOAs, a fully coherent solution requires the spin-up component in either case.

Radiative properties

Long-term Spectral Evolution

Following the data reduction described in § 7.2.1 we fitted each observation using the typical phenomenological two-component model used for magnetar spectra – an ab-

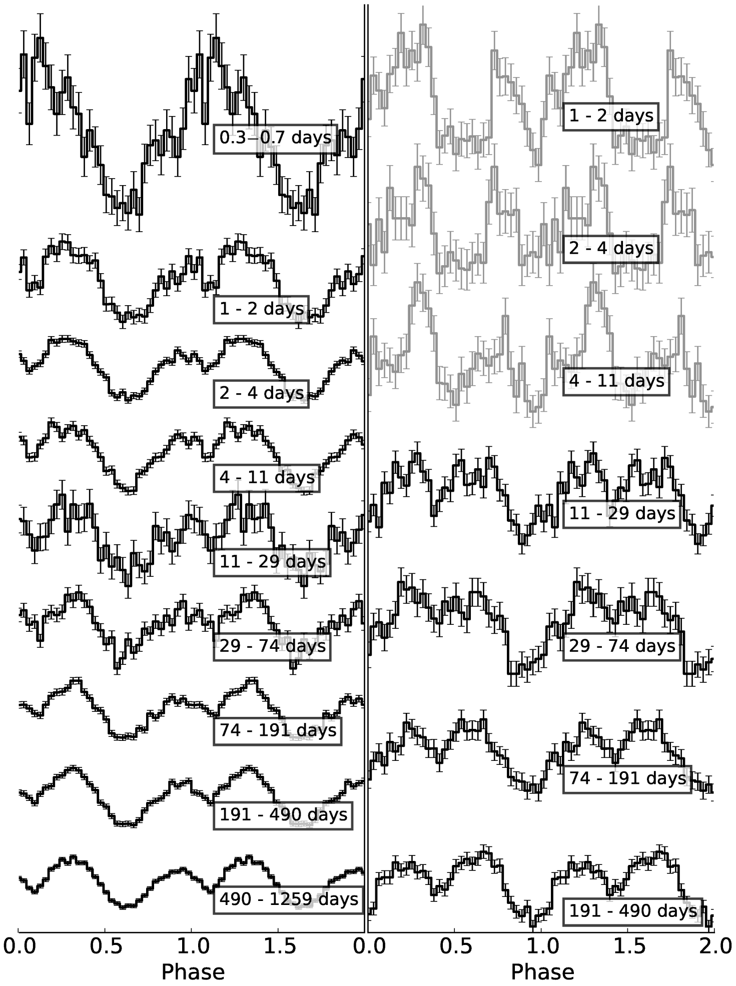

Figure 7.1 Pulse shape evolution of 4U 0142+61. The panels show the total 0.7–10-keV profiles, binned in equal log-time bins. The left panel present profiles following the 2011 outburst, in days from MJDs 55771.19, and the right panel following the 2015 outburst, in days from MJD 57081.2. The profiles have been normalized, and vertically shifted to avoid overlap. The three profiles in grey are those excluded from the timing solution due to profile variations.

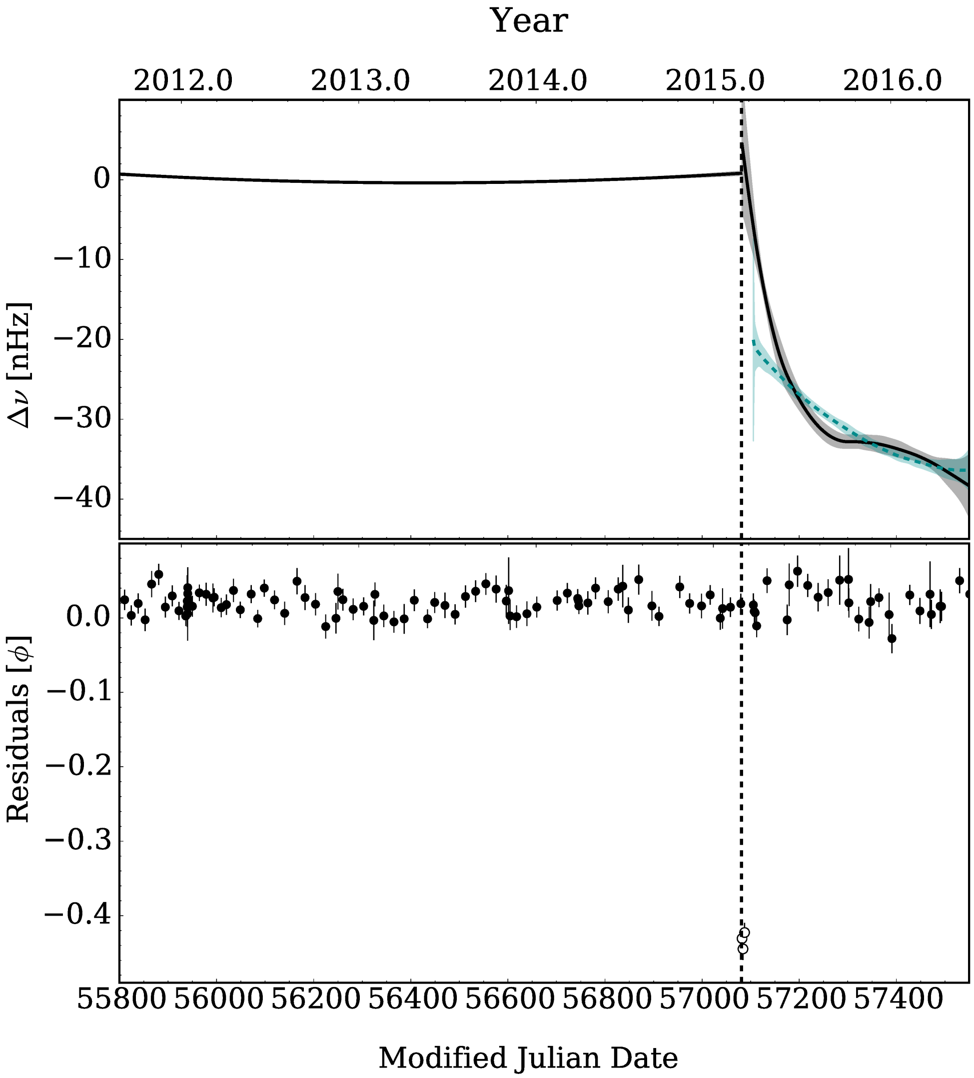

Figure 7.2 Timing evolution of 4U 0142+61 over the *Swift* campaign. The top panel shows ν over time with the average pre-burst $\dot{\nu}$ trend removed. The solid black line with a gray error region uses all TOAs, and the blue dashed line shows the solution excluding TOAs with strong pulse profile changes; see §7.3 for details. The bottom panel shows the timing residuals for the ephemeris presented in Table 7.1. The hollow points denote the TOAs excluded due to profile variations. In both panels, the dashed vertical time indicates the time of the glitch.

sorbed blackbody plus a power law. Photoelectric absorption was modelled using `XSPEC` `tbabs` with abundances from Wilms et al. (2000), and photoelectric cross-sections from Verner et al. (1996).

To determine a self-consistent N_H for 4U 0142+61, we simultaneously fit observations between MJD 56260–56999, i.e. a large set of observations far away from hard X-ray burst detections, and where the flux and spectral parameters of the individual observations were consistent. We fit these to a single absorbed blackbody plus power law and obtained $N_H = (1.11 \pm 0.04) \times 10^{22}$ cm^{-2} at 90% confidence with a C-statistic (Cash, 1979) of 18779.89 for 18553 degrees of freedom. As such, for all other spectral results presented here, we have assumed a constant value of $N_H = 1.11 \times 10^{22}\,\mathrm{cm}^{-2}$.

In Figure 7.3 we show the absorbed 0.5–10-keV flux, the power-law index, Γ, and the blackbody temperature, kT for each observation. We note that these two parameters are highly covariant due to their similar contributions to the flux in this band, and urge caution in interpreting any apparent trend. The epochs where 4U 0142+61 triggered the *Swift* BAT are indicated on the plot with vertical black lines: the dotted black line indicates the BAT trigger without a corresponding glitch, and the dashed lines indicate those associated with glitches. As well, the black arrow on the plot indicates that on MJD 57081.2 the flux was several times higher than the persistent level, decaying within a single orbit and contained several magnetar-like bursts. See § 7.4.2 for further details.

Taken with the marginal pulsed flux increase seen with *RXTE* (Dib & Kaspi, 2014) we can confirm using the XRT data that the 2011 glitch was a radiatively loud event. To characterize this radiative behaviour, we tried fitting the inter-glitch flux decay between MJDs 55771 and 57079 with a power-law, a linear decay, and an exponential decay, all plus a quiescent flux. As none of these single component models provided a statistically acceptable fit, we then fitted models with either two power-law decays ($\chi^2/dof = 90.8/70$), or two exponentials, both plus a constant quiescent flux. The best-fitting of these models, with $\chi^2/dof = 48.0/70$ is the double exponential, as described by the following equation: $F(t) = F_Q + F_1 e^{-(t-t_0)/\tau_1} + F_2 e^{-(t-t_0)/\tau_2}$ where F_Q is the 'quiescent' flux, fixed at $12.4(4) \times 10^{-11}$ erg s^{-1} cm^{-2}, the level measured on MJD 55768.7, the date of the last XRT observation prior to the flux increase. The best-fit parameters are $F_1 = 13(7) \times 10^{-11}$ erg s^{-1} cm^{-2}, $\tau_1 = 0.6(2)$ days, $F_2 = 1.4(1) \times 10^{-11}$ erg s^{-1} cm^{-2}, and $\tau_2 = 510(80)$ days. Note that all values here are absorbed 0.5–10-keV fluxes, and t_0 is held fixed at the time of the *RXTE* reported glitch, MJD 55771.19.

We also fitted the long-term decay in X-ray flux following the 2015 glitch. In this case we required only a single exponential decay, again fixing the quiescent flux at $12.4(4) \times 10^{-11}$ erg s^{-1} cm^{-2}. The best-fit parameters give a flux increase of $F = 1.3(3) \times 10^{-11}$ erg s^{-1} cm^{-2} with a decay time of $\tau = 160(70)$ days with $\chi^2/dof = 13.7/21$. The flux decay can be more clearly seen in Figure 7.4, where the data have been binned.

The X-ray pulse profile of 4U 0142+61 has been shown to evolve over a time scale of years (Dib et al., 2007). As such, we investigated the evolution of the pulse profile by at the time-scales suggested by the decaying total flux. To do so, we folded all aforementioned XRT observations into 32-bin profiles using a timing solution presented in Table 7.1, and created a profile for each equally logarithmically spaced segment of the time series following each of the two timing events. We then transformed these profiles into their respective Fourier representations, allowing us to quantify both the pulse shape, and root mean squared (RMS) pulsed fraction. For details

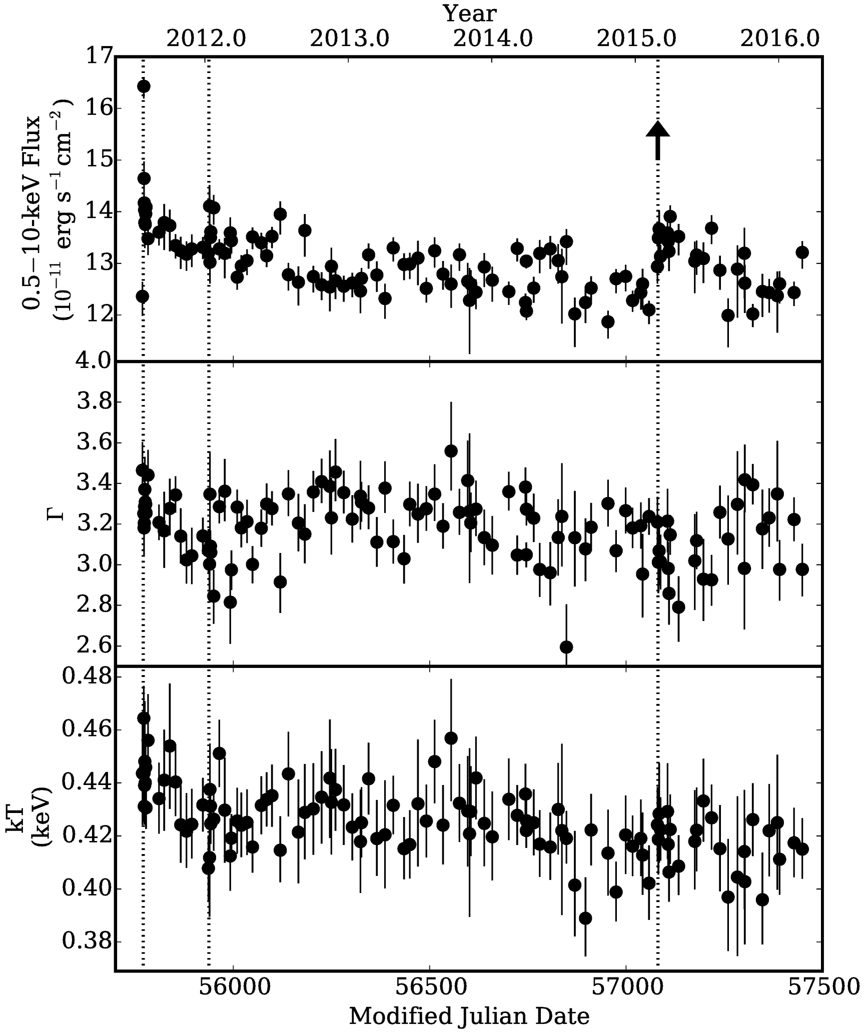

Figure 7.3 Flux and spectral evolution of 4U 0142+61 during *Swift* monitoring. The top panel shows the absorbed 0.5–10-keV flux. The vertical dashed lines indicate *Swift* BAT triggers associated with glitches, and the vertical dotted line indicates the BAT trigger with no associated timing behaviour The black arrow indicates the point at which the flux increases by a factor of ten, and decays on minutes time scales (see §7.4.2 and Fig. 7.5). The central panel shows Γ, the power-law index and the bottom panel shows kT, the blackbody temperature as a function of time.

Table 7.2 *Swift* XRT-detected burst parameters from 4U 0142+61 during the 2015 February event.

Burst time s from start	T_{90} ms	Fluence 1–10 keV Photons	Phase ϕ(0-1)
37.46	103 ± 5	14 ± 4	0.48
66.48	39 ± 14	12 ± 3	0.82
85.60	110 ± 80	19 ± 4	0.02
94.80	450 ± 60	61 ± 8	0.08
104.16	170 ± 50	37 ± 6	0.16
151.81	260 ± 20	56 ± 7	0.64
189.28	110 ± 30	48 ± 7	0.95
217.46	80 ± 50	22 ± 5	0.19
225.50	400 ± 300	17 ± 4	0.12
256.97	500 ± 100	19 ± 4	0.74
301.77	400 ± 300	7 ± 3	0.90
85 866.90	30 ± 20	7 ± 3	0.17

on the RMS pulsed fraction, see e.g. An et al. (2015). In Figure 7.4 we present the pulsed fraction, and power in the first two Fourier harmonics over time. For reference, in the top panel we show the total absorbed 0.5–10-keV flux binned at the same time resolution. The pulse profiles themselves can be seen in Figure 7.1. It is clear that the pulsed fraction of the source decreased rapidly starting from the 2011 glitch, mirroring the behaviour of the total X-ray flux. This was driven primarily by a decrease in the strength of the fundamental. Following both glitches the pulse profile shows variability for approximately ten days following the glitch before reattaining the normal state with both the fundamental and harmonic having equal power, as can be seen in Figure 7.4.

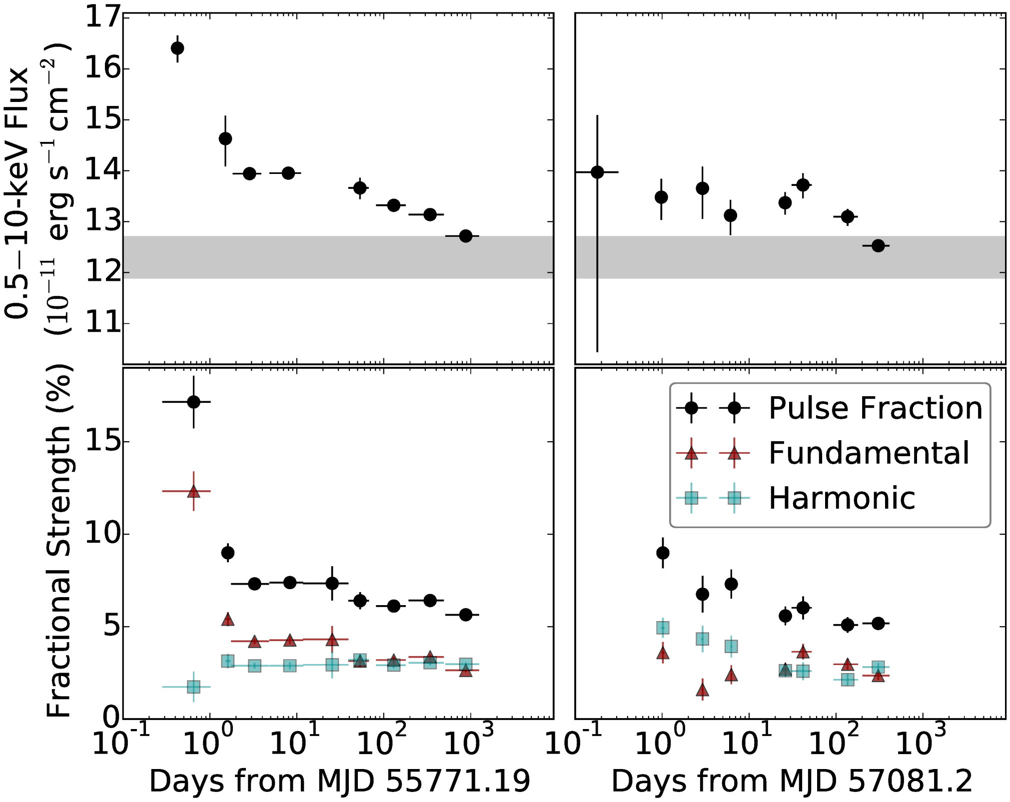

Figure 7.4 Flux & pulse shape evolution of 4U 0142+61. The top panels show the total absorbed 0.5–10-keV flux, binned in equal log-time bins from MJDs 55771.19, and 57081.2. The grey band in the upper panels shows the pre-2011 outburst flux value. The lower panels show the 0.7–10 keV RMS pulsed fraction as black circles, the strength in the fundamental (i.e. at the spin frequency) as red triangles, and first harmonic (i.e. at twice the spin frequency), as blue squares, with the same time binning.

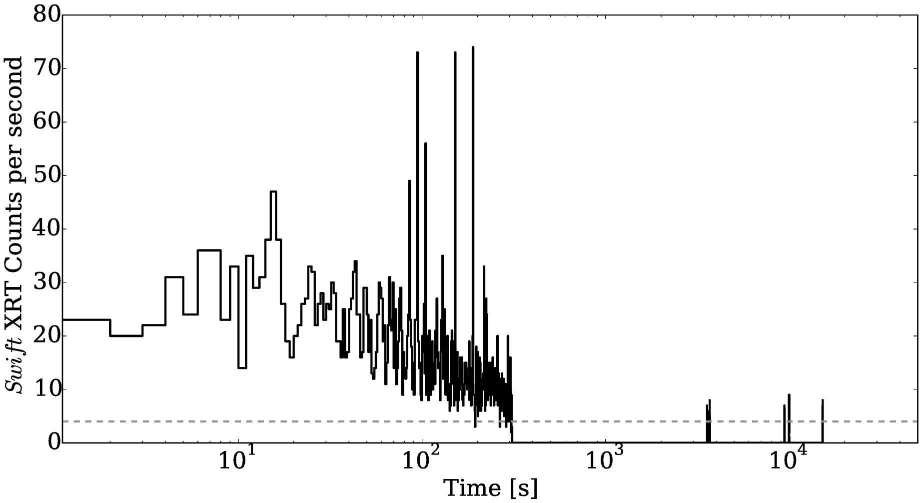

Figure 7.5 *Swift* XRT light-curve in the 0.7–10 keV band for the 2015 February 28 burst observation. The light curve has been binned at 1 s. The grey dashed line represents the average count rate of 4U 0142+61.

Short-term Flux Enhancement & Bursts

Immediately following the BAT trigger on MJD 57081, 2015 February 28 (Barthelmy et al., 2015), the XRT slewed to observe 4U 0142+61. For the first snapshot of observation, the source was significantly brighter, and harder than in the surrounding observations. Fitting an absorbed blackbody plus power law was not warranted, as the spectrum is well fit (C-stat of 904 for 947 degrees of freedom) by an absorbed power law with $\Gamma = 1.68(5)$ and an absorbed 0.5–10-keV flux of $1.06(3) \times 10^{-9}$ erg s^{-1} cm^{-2}. However, we note this is an average flux for this snapshot. The flux evolved on a faster time scale than this, and a more complicated short-term flux evolution is clear. This is evident in the binned light-curve of the XRT snapshot taken after the BAT trigger, shown in Figure 7.5 with a reference line plotted at the average count rate for 4U 0142+61.

We searched all *Swift* XRT observations for magnetar-like bursts at time scales of 1, 0.1, and 0.01 s. This was done following the method of Scholz & Kaspi (2011) wherein for each Good Time Interval (GTI), statistically significant deviations from the mean count rate, assuming Poisson statistics, are flagged. Due to the aforementioned instrumental bursts, the burst search was run only on photons having energies greater than 0.7 keV. We detected significant bursts only in the XRT data in the observations following the 2015 February 28 BAT detection (Barthelmy et al., 2015). Eleven bursts were found in this observation, superimposed on an overall flux decrease with a decay rate on the order 100 s.

As well, one burst was detected in the observation one day later. In Table 7.2 we present the burst times in seconds from MJD 57081.2043746, the total fluences, T_{90} (the time period which contains 90% of a bursts fluence) and the phase at which the peak of the burst occurred. The properties of these bursts are typical for magnetars (Collazzi et al., 2015).

We also note a third BAT detection of 4U 0142+61 on 2012 Jan 12 (Barthelmy et al., 2012). This burst was unaccompanied by any timing event, or long-term radiative change. While this lack of associated timing event is unique among the three BAT detections presented here, this is not atypical behaviour for magnetars. For example 1E 1841−045 has triggered BAT on several occasions with no measurable change in its timing properties (An et al., 2015).

Discussion

In this work, we have presented the evolution of the pulse profile, flux, and timing parameters of 4U 0142+61 from July 2011 to June 2016. Over this monitoring campaign, we report two timing events, both accompanied by changes in the radiative behaviour of the magnetar, as well as a BAT detected burst with no other associated behaviour

The first timing event occurred in 2011, and was characterized by a simple step-like glitch in spin frequency heralded by a BAT detected bright X-ray burst. This glitch was followed by an X-ray flux decay with two time scales – an initial fast decay with $\tau = 0.6(2)$ days and a longer $\tau = 510(80)$ day decay.

The second timing event in the *Swift* campaign occurred in 2015. This glitch had a more complex timing structure requiring a two-component model with a 57(9) day time scale resulting in a net spin down of the pulsar, see Table 7.1. This event was also accompanied by a BAT detected bright X-ray burst, as well as a long lived flux decay with $\tau = 160(70)$ days. This second event bears a striking resemblance to the 2006 outburst from this same source (Gavriil et al., 2011a). Both began with a ~ 100 s time scale X-ray flux increase, accompanied by several, clustered magnetar-like short X-ray bursts and a timing event resulting in a net spin-down of the pulsar. The long-term X-ray flux evolution of 4U 0142+61 is quite typical for a magnetar: the spectrum becoming harder at the time of the outburst; see § 7.4.2.

RADIATIVE EVOLUTION

There are two main classes of models to explain the flux evolution of magnetar outbursts: neutron star cooling and magnetospheric relaxation. Both sets of models can explain the differing time scales for outbursts from the same source, a common feature in magnetar outbursts (e.g. Bernardini et al., 2011; Gavriil & Kaspi, 2004; An et al., 2012).

In neutron star cooling models, the long-term flux evolution following a magnetar outburst is a thermal relaxation of the crust of the neutron star until it reattains thermal equilibrium with the core. In this model, the differing time scales for different events in the same source may be related to energy being injected at different depths in the crust of the neutron star (Brown & Cumming, 2009; Scholz et al., 2012; Deibel et al., 2015), with longer time scales corresponding to deeper layers in the crust.

The other major class of models which describe the flux relaxation of magnetars following outbursts involves the untwisting of the magnetosphere (e.g Beloborodov, 2009). In this model following the outbursts current carrying field lines, j-bundles, have been twisted by crustal motion. These twists are anchored to the surface and bombard the surface with accelerated charged particles, heating the surface. As the twist dissipates, the area affected by the bombardment shrinks, and cools. This has an expected decay time of $t_{ev} \sim 10^7 \, \mu_{32} \, \Phi_{10}^{-1} \, A_{11.5} \, \mathrm{s}$ where μ_{32} is the magnetic moment in units of $10^{32}\,\mathrm{G\,cm^3}$, Φ_{10} is the electric voltage sustaining electron-positron discharge in the magnetosphere in units of $10^{10}\,\mathrm{V}$ and $A_{11.5}$ the area of the j-bundle footprint in units of $10^{11.5}\,\mathrm{cm^2}$. With the parameters of 4U 0142+61, this time scale should be $t_{ev} \sim 10^7 \Phi_{10}^{-1}\,\mathrm{s} \sim 150 \Phi_{10}^{-1}$ days, roughly consistent with the flux decay time scale of the 2015 outburst. In this model, these different time scales would be due to different values of Φ_{10}, as the magnetic moment of the neutron star has not changed, and the blackbody area has only changed at the $\sim 10\%$ level over this campaign.

Glitches in High-B pulsars

Glitches in pulsars often result in both a permanent step in spin frequency and components which decay – typically with the functional form of an exponential. In standard pulsar glitch theory, glitches and their recoveries are an observable of the coupling between the neutron superfluid and non-superfluid components of the crust (e.g.

Table 7.3 Reported net spin-down glitches.

Pulsar	B-field 10^{14} G	Long-term $\Delta\nu$ Hz	Time scale Days	Q	Radiative Behavior	Reference
SGR 1900+14	7.0	$-1.10(3) \times 10^{-4}$	<80	–	giant flare, bursts	Woods et al. (1999)
PSR J1846–0258	0.49	$-9.52(9) \times 10^{-5}$	127(5)	8.7(2.5)	bursts, flux increase	Livingstone et al. (2010)[1]
1E 2259+586	0.59	$-4.5(6) \times 10^{-8}$	<4	–	burst, flux increase	Archibald et al. (2013)[2]
1E 2259+586	0.59	$-1.2(3) \times 10^{-8}$	–	–	flux increase	Içdem et al. (2012); Dib & Kaspi (2014)
4U 0142+61	1.3	$-1.27(17) \times 10^{-8}$	17(1.7)	1.07(2)	bursts, flux increase	Gavriil et al. (2011a)[3]
4U 0142+61	1.3	$-3.7(1) \times 10^{-8}$	57(9)	3.6(4)	bursts, flux increase	This work[4]
†1E 1841–045	7.0	$-4.9(6) \times 10^{-8}$	–	–	–	Şaşmaz Muş et al. (2014)[5]

[†] Disputed event, see the notes below.

[1] Accompanied by decaying spin-up glitch with $\Delta\nu = 10.8(4) \times 10^{-5}$ Hz.

[2] Possibly accompanied by second glitch event.

[3] Accompanied by decaying spin-up glitch with $\Delta\nu = 2.0(4) \times 10^{-7}$ Hz.

[4] Accompanied by decaying spin-up glitch with $\Delta\nu = 5.1(5) \times 10^{-8}$ Hz.

[5] Not seen in analysis of same data by Dib & Kaspi (2014).

Anderson & Itoh, 1975). For typical glitches, which result in a spin-up of the neutron star, the sudden spin-up is explained as a transfer of angular momentum from the superfluid component to the solid components of the crust. This will result in a spin-up of the neutron star as the superfluidic component has more angular momentum than the crust due to the crust suffering external spin-down torque. When the superfluid and solid components become coupled, the superfluid will have a higher angular velocity, and transfer some of this extra angular momentum to the solid crust. For a more thorough review of pulsar glitch theory, see Haskell & Melatos (2015).

In this standard picture, spin-down glitches can occur via the transfer of angular momentum from the inner crust, which may have slower spinning regions due to plastic crustal deformation caused by the extreme magnetic field (e.g. Thompson et al., 2000). The long-term X-ray pulse profile and pulsed fraction evolution, such as that presented in §7.4.1, could be evidence for the slow, plastic deformation of the crust needed to produce slower regions of superfluid (Woods et al., 2004; Thompson et al., 2002).

Alternatively, regions of the outer core could be involved due to the strong magnetic fields. Magnetar strength fields provide a strong pinning of vortices to flux tubes in the outer core, which leads to a rotation lag between the normal and superfluid components which, when relaxed, would lead to a spin-down event (Kantor & Gusakov, 2014).

In typical rotation-powered pulsars, the believed internal nature of these spin-up glitches is argued to be indicated by the lack of observed radiative changes. This 'radiatively quiet' condition does not hold for many glitches in magnetars. Many magnetar glitches are accompanied by drastic changed in their X-ray flux and pulse profiles (e.g. Kaspi et al., 2003; Dib et al., 2009). This could indicate that external forces are at play in radiatively loud glitches, and these external forces may lead to the net spin-down events reported in several magnetars, including the new event reported here.

We have compiled a list of all published confirmed and candidate net spin-down glitches in Table 7.3. In this list, we present the magnitude of the change in spin frequency, $\Delta\nu$. For net spin-down glitches that are due to over-recovering spin-up glitches, the τ_d of the glitch is presented. For events where there is no sign of a recovery, we show an upper limit for the time during which the spin-down had to occur. We also note that six of the eight reported net spin-down glitches are accompanied by radiative changes[ii]. This is a much higher fraction of radiatively activity than seen in spin-up events, where only five of twenty-two timing anomalies were accompanied by radiative changes (Dib & Kaspi, 2014).

For the net spin-down glitches in which the net spin down is measured to be due to an over-recovery, we also report the recovery fraction, Q. Recovering glitches are often classified by their recovery fraction, defined as $Q \equiv \Delta\nu_d/(\Delta\nu_d + \Delta\nu)$. In younger pulsars, when recoveries are observed, Q tends to be larger than in older pulsars (Wang et al., 2000). For the new glitch we report here, we measure $Q = 3.6 \pm 0.4$. Glitches with $Q > 1$ have been seen only twice before: once following the magnetar-like outburst of the high magnetic field rotation powered pulsar PSR J1846−0258 which had $Q = 8.7 \pm 2.5$ (Livingstone et al., 2010), and once during the 2006 outburst of 4U 0142+61 with $Q = 1.07 \pm 0.02$ (Gavriil et al., 2011a). Interestingly, all three of these over-recovering glitches were accompanied by radiative behaviour Indeed, it should be noted that due to the necessary non-continuous monitoring strategies used to study magnetars, all of the net spin-down events, i.e. the ‘anti-glitches’, may be unresolved over-recovering glitches, albeit with a short time scale. The most

---

[ii] This rises to six of six if we ignore the disputed event; see Table 7.3.

constraining limit placed on an unresolved over-recovery time scale is less than four days in the 2012 glitch of the magnetar 1E 2259+586. (Archibald et al., 2013).

The radiatively loud nature of these spin-down glitches could be symptomatic of external changes, e.g. the magnetosphere (Beloborodov, 2009; Parfrey et al., 2012, 2013). However, magnetars also exhibit typical spin-up glitches that are accompanied by similar radiative changes (e.g. Kaspi et al., 2003; Dib et al., 2009), which could indicate that another variable is at play. One possibility for this is the location of the twist in the magnetosphere. The observed radiative properties of magnetars are determined by their closed field, whereas the spin-down properties are dominated by the open field lines (e.g. Beloborodov & Thompson, 2007; Beloborodov, 2009). Therefore, depending on whether or not the closed field line region is affected during a twist event could determine if a glitch is accompanied by a radiative outburst.

Conclusion

We have presented the results of a five-year monitoring campaign of 4U 0142+61 using the *Swift* XRT. Over this campaign, we have shown that 4U 0142+61 has had two X-ray outbursts associated with timing events, one in 2011, and a second in 2015. The 2011 outburst was accompanied by a simple step-like spin-up glitch in spin frequency (Dib & Kaspi, 2014). The 2015 outburst was accompanied by an unusual glitch, starting with a spin-up in the spin frequency which decayed with a 57(9) day time scale, resulting in a net spin down of the pulsar.

As the sample of timing anomalies in magnetars continues to grow, we are detecting more net spin-down events, which have not been seen in the normal radio pulsar population. This strongly implicates the influence of a large magnetic field in spin-down events and, coupled with the radiatively loud nature of the plurality of spin-down events, suggests an origin in the magnetosphere of the star.

8

A Magnetar-like Outburst from a High-B Radio Pulsar

The contents of this chapter were first published with the same title in Archibald et al. (2016a).

Introduction

PSR J1119−6127 is a radio pulsar having spin period $P = 0.407$ s, discovered in the Parkes multibeam 1.4-GHz survey (Camilo et al., 2000). The pulsar's P and spin-down rate $\dot{P} = 4.0 \times 10^{-12}$ imply a characteristic age $\tau < 2$ kyr, making this object one of the youngest pulsars in the Galaxy, consistent with an association with the supernova remnant G292.2−0.5 (Crawford et al., 2001) at a distance of 8.4 kpc (Caswell et al., 2004). Those same spin parameters, under the assumption of vacuum dipole spin-down, imply a dipolar surface magnetic field $B = 4.1 \times 10^{13}$ G, among the highest known among radio pulsars. The pulsar's spin-down luminosity is $\dot{E} = 2.3 \times 10^{36}$ erg s^{-1}. For more on the assumptions that go into these characteristic properties, see § 1.4.1.

Past X-ray observations of the source (Gonzalez & Safi-Harb, 2003; Safi-Harb & Kumar, 2008; Ng et al., 2012) have shown it to be a soft X-ray pulsar, with strong pulsations below 2.5 keV, and none seen above this energy. This emission was well described by a two-component model consisting of a power law of index ∼2.1, with a hot thermal component of blackbody temperature $kT \simeq 0.2$ keV, high compared to lower-field radio pulsars of comparable age (see also Kaspi & McLaughlin, 2005; Zhu et al., 2011; Olausen et al., 2013). Radio pulse profile changes, short radio bursts and unusual timing recoveries were observed near epochs of glitches in this source (Weltevrede et al., 2011; Antonopoulou et al., 2015), reminiscent of radio radiative behaviour (e.g. Camilo et al., 2006) and glitch recoveries (Dib & Kaspi, 2014) following magnetar outbursts. The pulsar is also among the highest-B sources to have been detected in γ-rays by the *Fermi* LAT (Parent et al., 2011).

The *Fermi* GBM and *Swift* BAT (see § 3) both reported short magnetar-like bursts from PSR J1119−6127, on 2016 July 27 (UT 13:02:08; Younes et al., 2016) and 2016 July 28 (UT 01:27:51; Kennea et al., 2016), respectively. Immediately following the BAT burst, the *Swift* XRT found a bright X-ray source at the position of PSR J1119−6127 (Kennea et al., 2016) with pulsations at the rotational period (Antonopoulou et al., 2016). This suggests that this radio pulsar has had a magnetar-like outburst, similar to the 2006 transition of rotation-powered, but radio-quiet, pulsar PSR J1846−0258 (Gavriil et al., 2008). Interestingly, the radio pulsations from PSR J1119–6127 have disappeared (Burgay et al., 2016).

We report here on our Target-of-Opportunity (ToO) X-ray observations of PSR J1119−6127 with the *Swift* XRT and *NuSTAR* during the first few days of the transition, as well as on pre-outburst *Fermi* LAT timing data.

OBSERVATIONS & ANALYSIS

Swift-XRT & *NuSTAR* OBSERVATIONS

The *Swift*-XRT (Burrows et al., 2005) slewed to observe PSR J1119–6127 62.8 s after the BAT trigger (Kennea et al., 2016). XRT was operated in Photon Counting (PC) mode for this 2.2-ks observation (ObsID 00706396000, spanning 2016 July 28 01:28 – 02:07 UT), and in Windowed-Timing (WT) mode for the follow-up observations (ObsID 00034632001/2), spanning July 28 17:20 to July 29 03:11 UT and July 31 04:20 to August 1 20:37 UT for exposures of 9.9 and 4.8 ks, respectively.

As the time resolution of PC mode is 2.5 s (longer than the period of the pulsar), only WT mode observations, with a time resolution of 1.76 ms, were used in the timing analysis.

NuSTAR (Harrison et al., 2013) began ToO observations of PSR J1119–6127 at 2016 July 28, 23:05:12 UT yielding a total exposure time of 54.5 ks (ObsID 80102048002) partially overlapping with XRT observation 00034632001. The data from the two focal plane modules of *NuSTAR* are referred to hereafter as FPMA and FPMB.

The *Swift*-XRT and *NuSTAR* data were processed with the standard `xrtpipeline` and `nupipeline` scripts, respectively, using *HEASOFT* v6.17 and time corrected to the Solar System barycenter from the *Chandra* location of PSR J1119–6127 (Gonzalez & Safi-Harb, 2003).

For *Swift*, we selected only Grade 0 events for spectral fitting as other event grades are more likely to be caused by background events (Burrows et al., 2005). *Swift* spectra were extracted from the selected regions using `extractor`. Source photons were extracted from a 10-pixel radius circular region centred on PSR J1119–6127 with an annular background region with an inner and outer radius of 75 and 125 pixels, respectively.

The WT observations had multiple soft X-ray bursts which appear in both the source and background regions that, from past experience, seem to be instrumental in origin. Hence, for the WT mode data, we excluded all photons below 0.7 keV from our analysis.

For *NuSTAR* the source events were extracted within a 30-pixel ($72''$) radius around the centroid. Appropriate background regions were selected to be on the same detector as the source location. Spectra were extracted using the `nuproducts` script.

Using `grppha`, channels 0–70 (< 0.7 keV) and 700–1023 (> 7 keV) for *Swift* data and channels 0–35 (< 3 keV) and 1935–4095 (> 79 keV) for *NuSTAR* data were ignored and all good channels were binned to have a minimum of one count per energy bin.

Fermi LARGE AREA TELESCOPE OBSERVATIONS

We downloaded Pass 8R2 events of *Fermi* LAT (Atwood et al., 2009) all-sky survey observations from 2008 August 4 to 2016 July 30 from a one degree radius surrounding the *Chandra* position of PSR J1119–6127 and applied the recommended event selection. See § 3.7 for more information on the LAT. In the timing analysis, we used only photons having energy greater that 500 MeV based on the γ-ray pulse profile of PSR J1119–6127 (Parent et al., 2011). We corrected the arrival times of each photon to the Solar System barycentre using the `tempo2 fermi` plug-in (Ray et al., 2011).

Results

Timing Analysis

TOAs of γ-ray pulses were extracted using a maximum likelihood method, described in § 2. We extracted a TOA from photons collected in every 100 day span as a trade-off between TOA spacing and precision. We extended the ephemeris presented by Antonopoulou et al. (2015) using the LAT detected photons until the GBM-detected burst (Younes et al., 2016). We present a phase-coherent ephemeris in Table 8.1 and the timing residuals in the left panel of Figure 8.1.

To determine an ephemeris for the post-outburst *Swift* and *NuSTAR* observations, we folded the soft X-ray photons ($< 10\,\mathrm{keV}$) from each observation, starting with the ephemeris from the LAT observations and extracted TOAs from each orbit using the ML method. As there is no apparent evolution in the pulse profiles over the $< 10\,\mathrm{keV}$ energy band, the offset between TOAs from both telescopes should be minimal. We then used the `tempo2` timing software package (Hobbs et al., 2006) to fit the TOAs.

It is apparent that the LAT ephemeris did not accurately describe the post-outburst TOAs and requires a change in the spin frequency. Due to the long integration times required to extract a TOA from LAT, we are unable to constrain the exact glitch epoch; for this analysis, we have fixed the glitch epoch to the time of the first GBM-detected burst (Younes et al., 2016) and fitted for a glitch in spin frequency and frequency derivative.

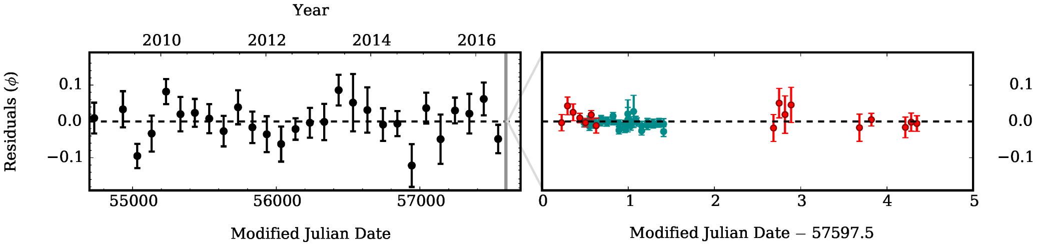

Figure 8.1 The left panel shows the LAT timing residuals of PSR J1119–6127 from MJD 54732 to 57544, (2008 September 23 – 2016 June 5), for the solution presented in Table 8.1. The gray vertical bar shows the burst epoch. The right panel shows the residuals for the post-outburst timing solution. Black points are LAT, red are XRT, and cyan are *NuSTAR*.

We measure a spin-up glitch with $\Delta\nu = 1.40(2) \times 10^{-5}$ Hz and $\Delta\dot{\nu} = -1.9(5) \times 10^{-12}$ Hz s^{-1}. We caution that this represents a snapshot of the frequency evolution, and that following glitches in magnetars, complex recoveries are often observed (e.g. Dib et al., 2008; Dib & Kaspi, 2014).

In Figure 8.2 we show the soft (0.7–2.5 keV), and hard (2.5–10 keV) X-ray pulse profiles from the radio pulsar state in 2011 (Ng et al., 2012), and the magnetar-like state in 2016. In the soft band, the root-mean-squared (RMS) pulse fraction has increased from 38(3)% to 71(4)%, while the pulse shape has remained similar. In the hard band, the RMS pulse fraction went from $< 10\%$ to 56(3)% pulsed.

X-RAY SPECTROSCOPY

All X-ray spectra were fit using `XSPEC` v12.9.0 (Arnaud, 1996) with a common value for hydrogen column density ($N_{\rm H}$). Magnetar spectra are typically described with an absorbed blackbody plus power-law model, which we use here. However, the independent *Swift*-XRT observations 00706396000 and 00034632002 were fit with a simple

Table 8.1 Phase-Coherent Ephemeris for PSR J1119–6127.

Fermi LAT Ephemeris	
Dates (MJD)	54732.82–57544.08
Dates	2008 Sept 23 – 2016 June 5
Epoch (MJD)	56264.00000
ν (s^{-1})	2.442 579 294 0(9)
$\dot{\nu}$ (s^{-2})	$-2.390\ 210(4)\times10^{-11}$
$\ddot{\nu}$ (s^{-3})	$5.68(3) \times 10^{-22}$
$\dddot{\nu}$ (s^{-4})	$-1.46(9) \times 10^{-30}$
$\nu^{(4)}$ (s^{-5})	$-3.1(7) \times 10^{-38}$
$\nu^{(5)}$ (s^{-6})	$1.8(1) \times 10^{-45}$
$\nu^{(6)}$ (s^{-7})	$3(1) \times 10^{-53}$
RMS residual (ms)	15.5
RMS residual (phase)	0.037
χ^2_ν/dof	1.08/20
Post-Outburst Ephemeris	
Dates (MJD)	57597.72–57601.85
Dates	28 July –1 Aug 2016
Epoch (MJD)	57600.
ν (s^{-1})	2.439 837 34(8)
$\dot{\nu}$ (s^{-2})	$-2.57(5)\times10^{-11}$
RMS residual (ms)	4.22
RMS residual (phase)	0.001
χ^2_ν/dof	0.74/46
Glitch Parameters	
Glitch Epoch (MJD), fixed	57596.547
$\Delta\nu$ (s^{-1})	$1.40(2) \times 10^{-5}$
$\Delta\dot{\nu}$ (s^{-2})	$-1.9(5) \times 10^{-12}$

Note: Figures in parentheses are the 1σ TEMPO2 uncertainties in the least-significant digits quoted. The source location was fixed at the *Chandra* position.

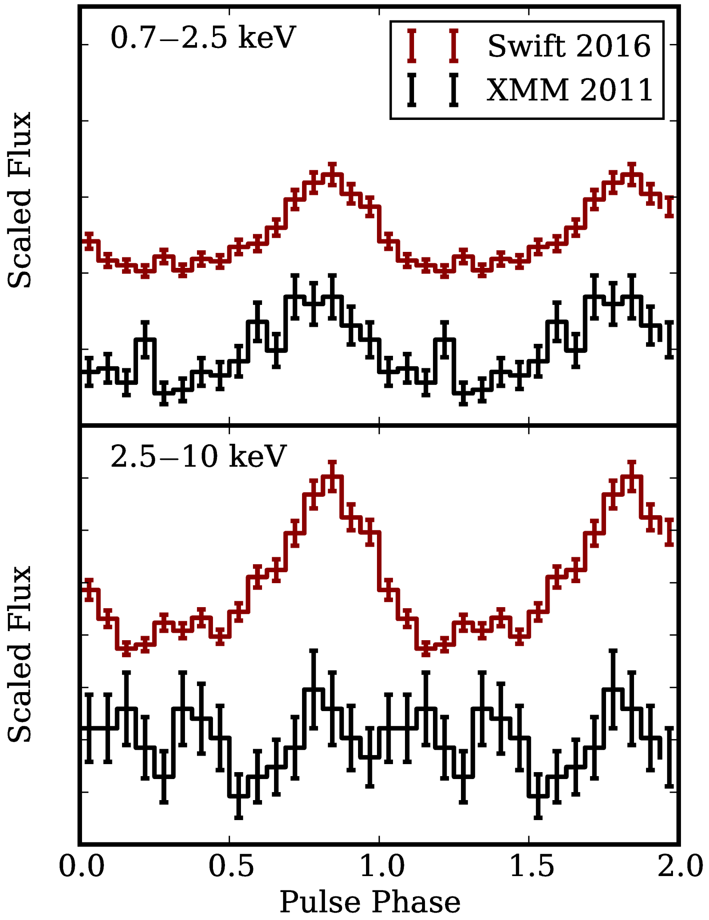

Figure 8.2 Pre- and post-outburst X-ray pulse profiles of PSR J1119–6127 from *Swift*-XRT (00034632001, red) and 2011 *XMM-Newton* data (Ng et al., 2012) (black) in the soft (0.7–2.5 keV, top panel) and hard (2.5–10 keV, bottom panel). The profiles have been arbitrarily offset vertically for clarity and aligned in phase based on the soft X-ray profile.

absorbed blackbody model between 0.7–7 keV as there is no constraint on the power law without the *NuSTAR* spectrum and there is little power-law contribution below 7 keV[i].

We used Cash statistics (Cash, 1979) for fitting and parameter estimation of the unbinned data. N_H was fit using `wilm` abundances and `vern` photoelectric cross-sections. The normalizations of *NuSTAR* FPMB and *Swift*-XRT spectra were allowed to vary with respect to that of the *NuSTAR* FPMA spectrum.

The hard X-ray tail seen above 8 keV in the PC mode observation (00706396000) may be caused by contamination due to short temporally unresolved X-ray bursts. Magnetar-like bursts are intrinsically harder than the average spectrum and the high count-rate leads to pile-up effects within the 2.5-s CCD readout time (e.g. Scholz & Kaspi, 2011). These pile-up effects are not mitigated by standard techniques such as the removal of the central bright region, as they are bunched temporally rather than spatially. If the hard X-ray tail were indeed real, it would have needed to fade by ~ 2 orders of magnitude in the day before the *NuSTAR* pointing to be consistent with the measured hard X-ray flux, while the blackbody temperatures measured on the two epochs are consistent with slow cooling. Hence, to fit the average spectra, we truncate the 00706396000 spectra above 7 keV.

Figure 8.3 shows the current *Swift*+*NuSTAR* spectral fits in comparison with a pre-burst *XMM-Newton* spectrum (from Ng et al., 2012). Table 8.2 details the parameter values with 90% confidence error bars.

Immediately after the burst, we measure a blackbody temperature $kT = 1.10(6)$ keV, slightly decreasing to $0.96(1)$ keV and $0.93(1)$ keV in the follow-up spectra. This is substantially higher than the pre-burst blackbody temperature of $0.21(4)$ keV (Ng

---

[i] Reduction and fitting of the *NuSTAR* data was performed by S. Tendulkar.

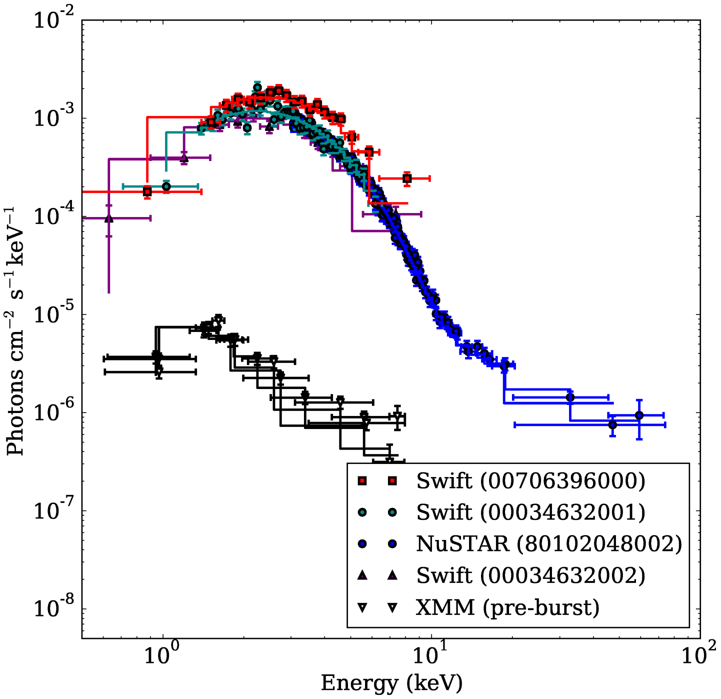

Figure 8.3 X-ray spectra of PSR J1119–6127. The data are as follows: pre-outburst *XMM-Newton* spectrum (inverted black triangles), *Swift*-XRT spectrum at burst (red squares), *Swift*-XRT and *NuSTAR* spectrum one day after the burst (green and blue circles, respectively), and a *Swift*-XRT spectrum three days after the burst (purple triangles). The flux increase above 8 keV in the *Swift*-XRT burst spectrum is likely due to pileup (see Section 8.3.2 for details). For clarity, the *NuSTAR* spectra from FPMA and FPMB are combined.

Table 8.2. Spectral Fits to NuSTAR and Swift-XRT Data

Component	Parameter	Value
`tbabs`	$N_{\rm H}$ ($10^{22}\,{\rm cm}^{-2}$)	1.2 ± 0.1
Swift-XRT 00706396000 (`tbabs*bbody`)		
`bbody`	$kT_{\rm BB}$ (keV)	1.10 ± 0.06
C − Stat/dof		333.82/413
goodness[a]		12%
Flux (0.5–10 keV)[b]		4.1 ± 0.1
L_X (0.5–10 keV)[c]		3.5
NuSTAR 80102048002 + *Swift*-XRT 00034632001 `const*tbabs*(bbody+powerlaw)`		
`const`	$C_{\rm FPMB}$[d]	1.01 ± 0.02
	$C_{\rm XRT}$[d]	0.94 ± 0.04
`bbody`	$kT_{\rm BB}$ (keV)	0.96 ± 0.01
`powerlaw`	Γ	1.2 ± 0.2
C − Stat/dof		2133.1/2327
goodness[a]		20%
Flux (0.5–10 keV)[b]		2.7 ± 0.1
L_X (0.5–10 keV)[c]		2.3
Flux (3–79 keV)[b]		1.9 ± 0.1
L_X (3–79 keV)[c]		1.6

et al., 2012). In the *NuSTAR* spectra, we also measure a hard power law with photon index $\Gamma = 1.2(2)$ that is marginally harder than the pre-burst value $\Gamma_{\rm PSR} = 2.1(8)$ (Ng et al., 2012). We also note that Ng et al. (2012) and Safi-Harb & Kumar (2008) measured the power law emission from the pulsar wind nebula (PWN) around PSR J1119–6127 to have $\Gamma_{\rm PWN} = 1.1 - 1.4$, close to the current hard power law index, but with a flux of $\sim 2 \times 10^{-14}\,{\rm erg\,cm^{-2}\,s^{-1}}$, almost three orders of magnitude fainter.

Table 8.2 (cont'd)

Component	Parameter	Value
Swift-XRT 00034632002 (`tbabs*bbody`)		
`bbody`	$kT_{\rm BB}$ (keV)	0.93 ± 0.06
$\rm C-Stat/dof$		304.7/355
goodness[a]		34%
Flux (0.5–10 keV)[b]		2.1 ± 0.2
L_X (0.5–10 keV)[c]		1.8

[a] Percentage of C-Stat statistic simulation trials from model parameters that are less than the fit statistic.

[b] Unabsorbed flux in units of $10^{-11}\,{\rm erg\,cm^{-2}\,s^{-1}}$.

[c] X-ray luminosity assuming isotropic emission at a distance of 8.4 kpc in units of $10^{35}\,{\rm erg\,s^{-1}}$.

[d] Cross-normalization constants w.r.t. *NuSTAR* FPMA.

Discussion

The outburst from PSR J1119−6127 is observationally very similar to those seen in magnetars. The phenomenology of magnetar outbursts is rich (see Rea & Esposito, 2011, for a review), but with established commonalities, practically all of which are observed in the PSR J1119−6127 event. A hallmark of magnetar outbursts are short-duration ($<$ 1-s) hard X-ray bursts, as reported for PSR J1119−6127 (Kennea et al., 2016; Younes et al., 2016). The large flux enhancement, here by a factor of $>$ 160, is commonly seen in magnetar outbursts, notably those in which the quiescent luminosity is below $\sim 10^{33}$ erg s^{-1} (e.g. Scholz & Kaspi, 2011; Kargaltsev et al., 2012). Moreover, the spectral hardening we report is classic for magnetar outbursts (Rea &

Esposito, 2011), as are timing anomalies, most often spin-up glitches (Dib et al., 2008; Dib & Kaspi, 2014). Overall, the PSR J1119−6127 event is clearly magnetar-like.

Most similar to the PSR J1119−6127 event is the 2006 magnetar-like outburst of PSR J1846−0258 (Gavriil et al., 2008). The latter is also a young ($\tau < 1000$ yr), high-B ($B = 5 \times 10^{13}$ G) rotation-powered pulsar, albeit radio undetected (Archibald et al., 2008). Next we compare this object's 2006 outburst with the event studied here.

One difference between the outbursts is their energetics. For PSR J1119−6127, the 0.5–10-keV flux as measured in the joint *Swift* and *NuSTAR* observation was $4.1(1) \times 10^{-11}$ erg s^{-1} cm^{-2}. For a distance of 8.4 kpc, and assuming isotropic emission, this implies a luminosity of 3.5×10^{35} erg s^{-1}, or $0.1\dot{E}$. This represents an increase over the quiescent value in this band of a factor of over ~ 160. Including the flux from 10 keV extrapolated to the top of the *NuSTAR* band increases this value by ∼20%. The efficiency for conversion of $\dot{E}$ to *Fermi*-band γ-ray emission, at least in quiescence, was estimated by Parent et al. (2011) to be 0.23. With a comparable amount of energy suddenly appearing in X-rays, the *Fermi*-band emission may have been affected during this outburst. However, the normally low *Fermi*/LAT count rate (see §8.3.1) requires multiple weeks of integration for a detection, hence a short-term anomaly may be undetectable.

By contrast, for PSR J1846−0258, in *Chandra* observations made within one week of its first detected magnetar-like burst, the unabsorbed flux in the 0.5–10-keV band was $4.0^{+1.6}_{-0.9} \times 10^{-11}$ erg s^{-1} cm^{-2} (Gavriil et al., 2008). For isotropic emission and a distance of 6 kpc (Leahy & Tian, 2008), this implies a luminosity of 1.7×10^{35} erg s^{-1}, or $0.02\dot{E}$. This represented an increase of a factor of $7.7^{+3.9}_{-1.8}$ over the quiescent value. As this outburst had no real-time trigger, it is possible that initially the pulsar brightened more. However the pulsed flux measured by *RXTE* at the initial burst epoch was comparable a week later. Hence the increase in flux was probably not much larger than a factor of ∼10, never exceeding a few percent of $\dot{E}$. Thus energetically, the PSR J1119−6127 outburst is far larger than that in PSR J1846−0258.

The spectral evolution in the two events also differed. In quiescence, PSR J1846−0258's X-ray spectrum is well described by a simple power law of index 1.1(1) (Gavriil et al., 2008), very different from the soft quiescent spectrum PSR J1119−6127. The latter, well described by a blackbody of $kT = 0.21(4)$ keV and power law of index 2.1(8) (Safi-Harb & Kumar, 2008; Ng et al., 2012), made this pulsar the youngest with detected thermal emission. It was also one of the hottest and most luminous thermal emitters even among rotation-powered pulsars of similar age (Olausen et al., 2013). This emission was also noted to be unusual for its high pulsed fraction (Ng et al., 2012).

During outburst, PSR J1846−0258 developed a bright soft component, whereas the harder power-law spectrum remained unchanged, apart from an increase in normalization by ∼35% above 10 keV (Kuiper & Hermsen, 2009). The soft component was described as having a power-law spectrum of index 1.9(1) (Safi-Harb & Kumar, 2008; Gavriil et al., 2008). By contrast, the spectrum of PSR J1119−6127 has undergone a radical hardening, with kT increasing from 0.21(4) keV to 1.10(6) keV. Nevertheless, the net effect in both outbursts was a transition to a spectrum very similar to those of bright magnetars.

It is also interesting to compare the outburst timing anomalies. In PSR J1846−0258, it suffered a sudden spin-up having $\Delta\nu/\nu \simeq 3 \times 10^{-6}$, followed by a large increase in $\dot{\nu}$ yielding a strong over-recovery of the glitch (Livingstone et al., 2010; Kuiper & Hermsen, 2009; Livingstone et al., 2011). The net long-term effect was a spin-

down, accompanied by a change in braking index and a long-term enhancement in timing noise. While it is too early to know the post-outburst timing evolution in PSR J1119−6127, from our timing analysis, we find that the pulsar had a similar-sized spin-up glitch with $\Delta\nu/\nu \simeq 5.8 \times 10^{-6}$. Presently any increase in spin-down rate is modest compared to some glitch recoveries in magnetars and certainly compared to that following the 2006 PSR J1846−0258 glitch. However, greater evolution may yet be detected.

In young radio pulsars like PSR J1119−6127, hard X-ray emission is thought to arise in the context of outer gap models (e.g. Wang et al., 2013) from synchrotron radiation from secondary electron/positron pairs produced by inward propagating curvature radiation γ-rays. As discussed by Parent et al. (2011), in PSR J1119−6127, the X-ray/γ-ray phase offset, together with the single-peak morphology of the γ-ray pulse, are well explained in outer gap models. The luminosity of both the X-ray and γ-ray emission in this picture must be bounded by the spin-down power.

The increase in X-ray luminosity particularly in the hard X-ray range during the outburst of PSR J1846−0258 was argued by Kuiper & Hermsen (2009) to be plausibly due to the above-described rotation-powered outer-gap emission, enhanced by particle injection due to perhaps to crust cracking that occurred at the glitch, reasonable given the lack of evidence for the hard X-ray luminosity exceeding more than a few percent of $\dot{E}$.

The new hard X-ray emission component in PSR J1119−6127 could have an outer-gap origin as well, but the large luminosity rise to within $0.1\dot{E}$ in the X-ray band alone may be difficult to accommodate in such a picture, and might require a commensurate increase in γ-ray luminosity, impossible given the available $\dot{E}$ energy budget.

Alternatively, the hard X-ray emission may be magnetar-like. The origin of the bright hard X-ray component in magnetars has been argued to be a decelerating electron/positron flow in the closed magnetosphere, in the higher altitude regions of large magnetic loops (Beloborodov, 2013). This emission is powered ultimately by the internal stellar magnetic field and is not limited by $\dot{E}$. In this interpretation, the pulsar suffered an instability such that a significant twist in its field lines occurred, with highly relativistic particles ($\gamma >> 10$) injected near the star where $B >> B_{QED} = 4.4 \times 10^{13}$ G. If this is origin of the hard X-rays in PSR J1119−6127, then the true internal field of this pulsar is far higher than is inferred from its dipole component. This would support the argument for additional non-dipolar field components in apparently low-magnetic-field magnetars (Rea et al., 2010; Scholz et al., 2014b). One way to test this explanation is through modelling of the phase-resolved hard X-ray spectrum. This can yield constraints on the geometry of the emission region (e.g. Hascoët et al., 2014). Such constraints could then be compared with similar ones from radio polarimetry (Weltevrede et al., 2011) and/or modelling of the γ-ray light curve (Parent et al., 2011).

Importantly, PSRs J1846−0258 and now J1119−6127 are the only two rotation-powered pulsars to have exhibited radiative changes at glitch epochs; this must be a consequence of their high spin-inferred B. Indeed no X-ray enhancement was seen in *Chandra* observations made 3.5 days following a large ($\Delta\nu/\nu = 3 \times 10^{-6}$) spin-up glitch in the lower-field ($B = 3.4 \times 10^{12}$ G) Vela radio pulsar (Helfand et al., 2001). On the other hand, there was no evidence for an X-ray enhancement in PSR J1846−0258 near the epoch of a much smaller glitch having $\Delta\nu/\nu = 2.5 \times 10^{-9}$ (Livingstone et al., 2006), nor in previous glitches ($\Delta\nu/\nu = 2.9 \times 10^{-7}$ and 4.1×10^{-6} in 2004 and 2007, respectively) in PSR J1119−6127 (Weltevrede et al., 2011;

Antonopoulou et al., 2015), although proodempt X-ray observations were not performed in those cases. Moreover, multiple sizeable glitches in *bona fide* magnetars have been unaccompanied by radiative changes (Scholz et al., 2014a; Dib & Kaspi, 2014). This may indicate that an independent parameter such as the crustal depth of the glitch location plays a role in the radiative detectability of high-B neutron-stars at glitch epochs (see, e.g., Eichler & Cheng, 1989; Lyubarsky et al., 2002).

The possibility of a magnetar-like outburst from a high-B radio pulsar was discussed by Kaspi & McLaughlin (2005), who also suggested the possibility of radio emission from magnetars prior to its discovery by Camilo et al. (2006). Pons & Perna (2011) and Perna & Pons (2011) provided theoretical groundwork for the hypothesis, and magnetothermal modelling such as that by Viganò et al. (2013) have further developed these ideas, which are now on solid observational ground. Other high-B radio pulsars like PSRs J1718−3718 (Zhu et al., 2011) and J1734−3333 (Olausen et al., 2013) seem likely to also undergo a magnetar-like transition in coming years.

Thou Pow'r Supreme, whose mighty scheme
These woes of mine fulfil,
Here, firm, I rest, they must be best, Because
they are Thy will!
Then all I want (O, do Thou grant This one re-
quest of mine!) Since to enjoy Thou dost deny,
Assist me to resign.

Robert Burns

9

Conclusion

In this thesis, I have presented X-ray timing studies of five young pulsars. Three of these studies are on objects traditionally classified as rotation-powered pulsars, and two on objects which are prototypical of the magnetar class, although this distinction, as we saw in Chapter 8, is becoming more and more blurred. Each of these results indicates that pulsar magnetospheres have a more complex structure than a simple dipole, and that the magnetosphere can have a strong effect on all the observed properties of neutron stars. Here, I will review the main results presented in this thesis, and put them in context with recent results from the field. I will then speculate on future directions to make progress in the field.

On Braking Indices

In this thesis I presented two novel results on braking indices. First, that braking indices can suddenly undergo long-lived changes (see Chapter 4), which we argue is due to a change in magnetospheric configuration. Second, we showed that braking indices can be greater than the three, as for a vacuum dipole (see Chapter 5), indicating that quadrupolar magnetic fields in the magnetosphere likely influence the spin-down rate of PSR J1640−4631, and likely all neutron stars.

I will start off this section by introducing one more pulsar braking index to the fold, measured after the publication of Chapters 4 & 5. PSR J1208−6238 is a newly discovered radio-quiet *Fermi* gamma-ray pulsar with a spin frequency of 2.26 Hz (Clark et al., 2016). Conveniently, due to the continuous, all-sky scan strategy of *Fermi* LAT data, despite being discovered in 2016, it was possible to time the pulsar over five years, yielding a braking index of $n = 2.598 \pm 0.001$ (Clark et al., 2016). As can be seen in Figure 9.1, this is a rather typical braking index.

More excitingly, since the report of the change in braking index of PSR J1846−0258 (see Chapter 4), another braking index has been reported to change dramatically. PSR B0540−69 is a young ($\tau_c \sim 1700$ year old) pulsar in the Large Magellanic Cloud with a spin frequency of 19.8 Hz. In 15.8 years of timing using *RXTE*, PSR B0540−69's braking index was measured to be constant at $n = 2.129 \pm 0.012$ over three epochs separated by two glitches (Ferdman et al., 2015). At the end of this 15.8 year monitoring, the spin-down rate suddenly increased by $\sim$ 36% (Marshall et al., 2015). In this new high spin-down state, a timing campaign showed the braking index too had changed to be $n = 0.031 \pm 0.013$ (Marshall et al., 2016) –i.e. the braking index changed by 2.10 ± 0.02. Intriguingly as pointed out by Marshall et al. (2016),

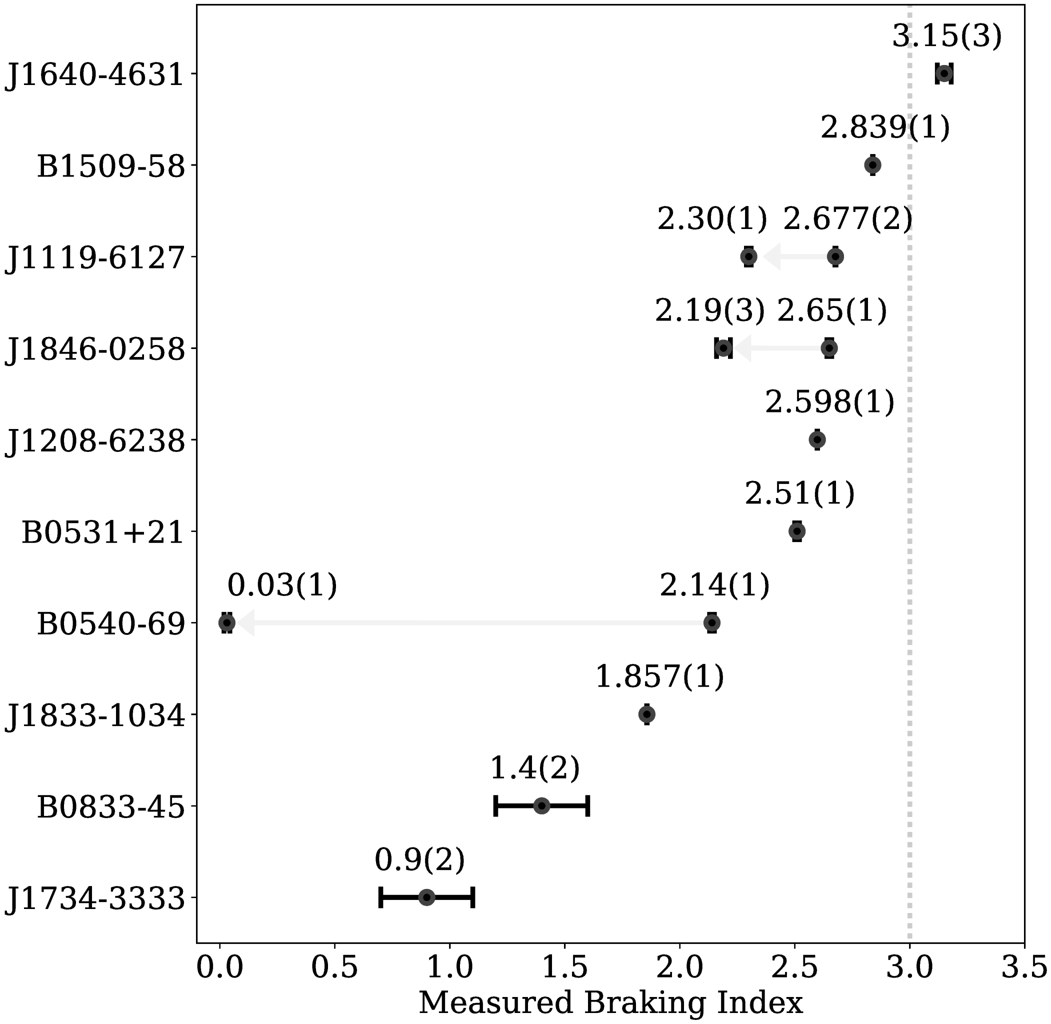

Figure 9.1 All measured braking indices. The grey dotted line indicates a braking index of three, that which is expected for a pure magnetic dipole. For PSR J1846−0258 (Archibald et al., 2015b), PSR J1119−6127 (Antonopoulou et al., 2015), and PSR B0540−69 (Marshall et al., 2016), where the braking index changed following glitches, the grey arrows indicate the direction of change following the glitch. The braking index of PSR J1208−6238 is from Clark et al. (2016). All other braking indices are from Lyne et al. (2015) and references therein.

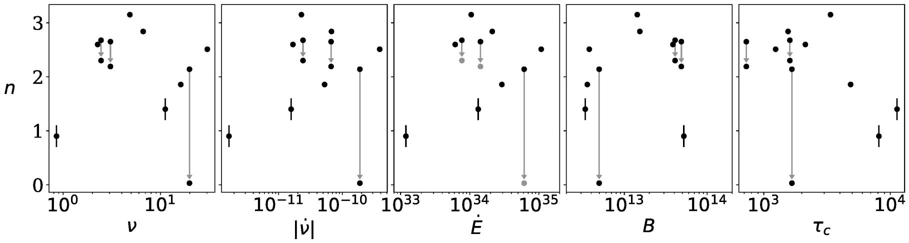

Figure 9.2 All measured braking indices plotted against ν, $\dot{\nu}$, $\dot{E}$, B, and τ_c. For the three braking indices that have changed, a grey arrow points from the old to the new braking index. For the origins of this data, see Figure 9.1. Also, keep in mind that $n = \nu\ddot{\nu}/\dot{\nu}^2$ i.e. is not completely independent of the x-axis in any case.

the change in n reported in PSR B0540−69 is distinct from the other two pulsars in which changes in n have been reported in the literature (see Chapter 4 and Antonopoulou et al., 2015). In both those other cases, the change in n was at the time of atypical radiatively loud glitches. Additionally, PSR B0540−69 has a much lower magnetic field (B$\sim 6\times10^{12}$ G) than either PSR J1846−0258 (B$\sim 5\times10^{13}$ G) or PSR J1119−6127 (B$\sim 4\times10^{13}$ G) , the two other pulsars that have had a change in their braking indices. In Chapter 4, we suggested that the changes in n were likely to be related to their high-B fields, and connected to a reconfiguration of the pulsar magnetosphere following magnetar-like activity. With this low-B case, however, it is hard to invoke this argument due to the much lower magnetic field, and lack of magnetar-like activity coincident with this change. A possible explanation in this case,as suggested by Marshall et al. (2016), is that the difference is due to a different magnetospheric mode, similar to mode-changing pulsars (see Lyne et al., 2010, and § 6.3).

The entire collection of measured braking indices is plotted in Figure 9.2 against ν, $\dot{\nu}$, $\dot{E}$, B, and τ_c, but no clear trend emerges. I would, however, like to point out that now, of the 10 pulsars with measured braking indices we have seen 3 of them suddenly change in the 50 years since the discovery of pulsars. This strongly suggests that the generally made assumptions in measuring characteristic ages, and in population synthesis models that a braking index is a constant quantity must be modified.

Initial work in this direction is indeed being done. Johnston & Karastergiou (2017) have recently performed a population study where, instead of pulsars being born with a constant braking index as in e.g. Faucher-Giguère & Kaspi (2006), they chose a random braking index, and allowed it to evolve via magnetic field decay, a changing α, as well as a random component which changed the braking index every 1000 years. In this implementation, they find that to match the observed pulsar population, older pulsars[i] should have higher braking indices. As well, the smaller a pulsar's α, the larger the braking index should be. While this initial attempt made many simplifying assumptions, e.g. all pulsars are born with the same period, these initial results are encouraging.

ON THE REPETITION OF OUTBURSTS & TORQUE FLUCTUATIONS IN 1E 1048.1−5937

In Chapter 6, I presented X-ray observations of 1E 1048.1−5937 which showed a quasi-periodic repetition in both X-ray flux enhancements and in its spin-down behaviour. On 23 July-2016 (MJD 57592), 1E 1048.1−5937 entered another flux enhanced state (Archibald et al., 2016b). This is a 1670 ± 10 day span since the prior outburst, compared to separations of 1800 ± 10, and 1740 ± 10 days between the prior flares as discussed in Chapter 6. This is consistent with the quasi-periodicity reported in Chapter 6, but the origin of this remains a mystery. At the start of this new flare,

---

[i] Here, older refers to pulsars with $\tau_c \quad >> \quad 10^5$ yr i.e. older than all the ones with a measured value, and thus this prediction is not testable by measuring the braking indices of young pulsars, but rather by an analysis of the larger pulsar population via e.g. population synthesis modelling.

we triggered a *NuSTAR* target-of-opportunity observation, and Gemini near-infrared observations, the results of which shall be studied and presented in a future work.

On Spin-down Glitches

In Chapter 7, I presented X-ray observations of two outbursts from the magnetar 4U 0142+61. Interestingly, one of these outbursts was accompanied by a rare net spin-down glitch. Based on both the observation that all spin-down events have occurred in high-B pulsars, and the radiatively loud nature of all confirmed net spin-down events reported in the literature (see Table 7.3), we argued that these spin spin-down events are likely to be due to magnetospheric changes, rather than internal exchanges of angular momentum in normal pulsar glitches.

On The Spread of Magnetar Behaviour

As described in Chapter 8, in 2016 a radio-detected, high-magnetic-field, rotation-powered pulsar PSR J1119−6127, underwent a magnetar-like outburst – increasing its X-ray luminosity by a factor of at least 160, and emitting several high-energy X-ray bursts (see Chapter 8, Archibald et al., 2016a; Göğüş et al., 2016).

Taken with the 2006 outburst of the high magnetic field rotation-powered pulsar PSR J1846−0258 (Gavriil et al., 2008), this new outburst proves an unambiguous connection between the radio pulsar and magnetar populations as initially suggested by Kaspi & McLaughlin (2005).

In addition, we are starting to see magnetar-like behaviour from an even wider variety of sources. In 2016, the central compact object in the supernova remnant RCW 103, 2E 1613.5−5053, which is the slowest known isolated pulsar, recently underwent a magnetar-like outburst. Despite an unusual slow 6.67 hr rotation period[ii], the source underwent what was otherwise a typical magnetar-like outburst: its X-ray luminosity increased by a factor of ∼100, and emitted a magnetar-like burst (D'Aì et al., 2016; Rea et al., 2016). Indeed, the energy contained in this one outburst is comparable to the rotational energy of the pulsar, meaning the outburst cannot be rotationally powered (D'Aì et al., 2016). The slow 6.67 hr rotation remains a challenge to reconcile with the ∼ 2000 yr age of RCW 103, given the observed spin-periods of young pulsars.

The collection of magnetar behaviour from sources throughout the neutron star zoo raises questions on the origin on magnetar activity, and what properties a source requires to exhibit it. Indeed, we may need to consider the magnetic energy stores for all pulsars.

On Future Directions

The best way to further our understanding of braking indices is to measure them for many more pulsars. The best prospect for this is the upcoming Square Kilometre Array (SKA). The SKA, as implied by the name, will have a large amount of collecting area, and can therefore be used to conduct sensitive pulsar searches. With these, the SKA is projected to increase the number of known pulsars by nearly an order of magnitude (Smits et al., 2009). This should then increase the number of pulsars for which we can measure a braking index by a similar factor, and take us well out of the small number statistics regime that currently exists for braking indices.

[ii] While this periodicity has been suggested to be due to binary motion and not simple rotation, new near-infrared constraints on the existence of a companion are strong evidence that this is indeed an isolated pulsar (Tendulkar et al., 2016).

As mentioned several times throughout this document, an excellent way to constrain the geometry of pulsars and their magnetosphere is by means of X-ray polarisation measurements. These measurements are useful as the magnetic fields present in the magnetosphere will introduce a very phase dependent polarisation which depends on the geometry of the magnetic fields (Costa et al., 2006; Heyl & Shaviv, 2002; Lai & Ho, 2003). The *Imaging X-ray Polarimetry Explorer (IXPE)* has been selected as a NASA Small Explorer class mission (Weisskopf et al., 2016). This mission, and other future missions building on it, will be useful to test models of both the geometries implied by some models for braking indices, as well as those of the magnetars.

In the near future, we may also be able to capture weaker magnetar-like outbursts. More sensitive all sky X-ray monitors such as the Wide Field Monitor on the proposed *LOFT/STROBE-X* will be sensitive to weaker magnetar like bursts and outbursts from pulsars (Brandt et al., 2012; Wilson-Hodge et al., 2017). Importantly, this should continue the legacy of the *Swift* BAT and *Fermi* GBM, giving an unbiased sample all across both the sky and the $P - \dot{P}$ diagram, an excellent test of which pulsars display such behaviour.

References

Alpar, M. A., Cheng, A. F., Ruderman, M. A., & Shaham, J. 1982, Nature, 300, 728

An, H., Kaspi, V. M., Tomsick, J. A., et al. 2012, ApJ, 757, 68

An, H., Hascoët, R., Kaspi, V. M., et al. 2013, ApJ, 779, 163

An, H., Archibald, R. F., Hascoët, R., et al. 2015, ApJ, 807, 93

Anderson, P. W., & Itoh, N. 1975, Nature, 256, 25

Antonopoulou, D., Vasilopoulos, G., & Espinoza, C. M. 2016, The Astronomer's Telegram, 9282

Antonopoulou, D., Weltevrede, P., Espinoza, C. M., et al. 2015, MNRAS, 447, 3924

Archibald, A. M., Kaspi, V. M., Livingstone, M. A., & McLaughlin, M. A. 2008, ApJ, 688, 550

Archibald, A. M., Bogdanov, S., Patruno, A., et al. 2015a, ApJ, 807, 62

Archibald, R., Scholz, P., & Kaspi, V. M. 2017a, The Astronomer's Telegram, 10107

Archibald, R. F., Kaspi, V. M., Beardmore, A. P., Gehrels, N., & Kennea, J. A. 2015b, ApJ, 810, 67

Archibald, R. F., Kaspi, V. M., Ng, C.-Y., et al. 2015c, ApJ, 800, 33

Archibald, R. F., Kaspi, V. M., Scholz, P., et al. 2017b, ApJ, 834, 163

Archibald, R. F., Kaspi, V. M., Tendulkar, S. P., & Scholz, P. 2016a, ApJ, 829, L21

Archibald, R. F., Tendulkar, S. P., Scholz, P., & Kaspi, V. M. 2016b, The Astronomer's Telegram, 9316

Archibald, R. F., Kaspi, V. M., Ng, C.-Y., et al. 2013, Nature, 497, 591

Archibald, R. F., Gotthelf, E. V., Ferdman, R. D., et al. 2016c, ApJ, 819, L16

Arnaud, K. A. 1996, in Astronomical Society of the Pacific Conference Series, Vol. 101, Astronomical Data Analysis Software and Systems V, ed. G. H. Jacoby & J. Barnes, 17

Arzoumanian, Z., Nice, D. J., Taylor, J. H., & Thorsett, S. E. 1994, ApJ, 422, 671

Arzoumanian, Z., Brazier, A., Burke-Spolaor, S., et al. 2016, ApJ, 821, 13

Atwood, W., Albert, A., Baldini, L., et al. 2013, ArXiv e-prints, arXiv:1303.3514 [astro-ph.IM]

Atwood, W. B., Abdo, A. A., Ackermann, M., et al. 2009, ApJ, 697, 1071

Baade, W., & Zwicky, F. 1934a, Proc. N.A.S., 20, 259

—. 1934b, Phys. Rev., 46, 76

Backer, D. C., Kulkarni, S. R., Heiles, C., Davis, M. M., & Goss, W. M. 1982, Nature, 300, 615

Barthelmy, S. D., Gehrels, N., Kennea, J. A., et al. 2015, GRB Coordinates Network, 17507, 1

Barthelmy, S. D., Barbier, L. M., Cummings, J. R., et al. 2005, Space Sci. Rev., 120, 143

Barthelmy, S. D., D'Elia, V., Gehrels, N., et al. 2012, GRB Coordinates Network, 12829

Baym, G., Pethick, C., & Pines, D. 1969, Nature, 224, 673

Beloborodov, A. M. 2009, ApJ, 703, 1044

—. 2013, ApJ, 762, 13

Beloborodov, A. M., & Thompson, C. 2007, ApJ, 657, 967

Bernardini, F., Israel, G. L., Stella, L., et al. 2011, A&A, 529, A19

Bisnovatyi-Kogan, G. S., & Postnov, K. A. 1993, Nature, 366, 663

Blandford, R. D., & Romani, R. W. 1988, MNRAS, 234, 57P

Boldt, E. A., Desai, U. D., Holt, S. S., Serlemitsos, P. J., & Silverberg, R. F. 1969, Nature, 223, 280

Bowyer, S., Byram, E. T., Chubb, T. A., & Friedman, H. 1964a, Science, 146, 912

—. 1964b, AJ, 69, 135

Boynton, P. E., Groth, E. J., Hutchinson, D. P., et al. 1972, ApJ, 175, 217

Brandt, S., Hernanz, M., Alvarez, L., et al. 2012, in Proc. SPIE, Vol. 8443, Space Telescopes and Instrumentation 2012: Ultraviolet to Gamma Ray, 84432G

Brown, E. F., & Cumming, A. 2009, ApJ, 698, 1020

Brown, J. C., Haverkorn, M., Gaensler, B. M., et al. 2007, ApJ, 663, 258

Burgay, M., Possenti, A., Kerr, M., et al. 2016, The Astronomer's Telegram, 9286

Burgay, M., Rea, N., Israel, G. L., et al. 2006, MNRAS, 372, 410

Burrows, D. N., Hill, J. E., Nousek, J. A., et al. 2005, Space Sci. Rev., 120, 165

Şaşmaz Muş, S., Aydın, B., & Göğüş, E. 2014, MNRAS, 440, 2916

Camilo, F., Kaspi, V. M., Lyne, A. G., et al. 2000, ApJ, 541, 367

Camilo, F., Ransom, S. M., Halpern, J. P., et al. 2006, Nature, 442, 892

Camilo, F., & Reynolds, J. 2007, The Astronomer's Telegram, 1056, 1

Camilo, F., Cognard, I., Ransom, S. M., et al. 2007, ApJ, 663, 497

Cash, W. 1979, ApJ, 228, 939

Caswell, J. L., McClure-Griffiths, N. M., & Cheung, M. C. M. 2004, MNRAS, 352, 1405

Chadwick, J. 1932, Nature, 129, 312

Chen, A. Y., & Beloborodov, A. M. 2014, ApJ, 795, L22

Cheng, K. S., Ho, C., & Ruderman, M. 1986, ApJ, 300, 500

Chiu, H.-Y., & Salpeter, E. E. 1964, Physical Review Letters, 12, 413

Clark, C. J., Pletsch, H. J., Wu, J., et al. 2016, ApJ, 832, L15

Collazzi, A. C., Kouveliotou, C., van der Horst, A. J., et al. 2015, ApJS, 218, 11

Contopoulos, I., & Spitkovsky, A. 2006, ApJ, 643, 1139

Cordes, J. M., & Downs, G. S. 1985, ApJS, 59, 343

Costa, E., Bellazzini, R., Soffitta, P., et al. 2006, ArXiv Astrophysics e-prints, astro-ph/0603399

Crawford, F., Gaensler, B. M., Kaspi, V. M., et al. 2001, ApJ, 554, 152

D'Aì, A., Evans, P. A., Burrows, D. N., et al. 2016, MNRAS, 463, 2394

de Jager, O. C., Raubenheimer, B. C., & Swanepoel, J. W. H. 1989, A&A, 221, 180

Deibel, A., Cumming, A., Brown, E. F., & Page, D. 2015, ApJ, 809, L31

den Herder, J. W., Brinkman, A. C., Kahn, S. M., et al. 2001, A&A, 365, L7

Deutsch, A. J. 1955, Annales d'Astrophysique, 18, 1

Dib, R., & Kaspi, V. M. 2014, ApJ, 784, 37

Dib, R., Kaspi, V. M., & Gavriil, F. P. 2007, ApJ, 666, 1152

Dib, R., Kaspi, V. M., & Gavriil, F. P. 2008, ApJ, 673, 1044

—. 2009, ApJ, 702, 614

Dierckx, P. 1975, J.Comp.Appl.Maths, 1, 165

Dodson, R. G., McCulloch, P. M., & Lewis, D. R. 2002, ApJ, 564, L85

Ducros, G., Ducros, R., Rocchia, R., & Tarrius, A. 1970, Nature, 227, 152

Duncan, R. C., & Thompson, C. 1992, ApJ, 392, L9

Efron, B. 1979, Ann. Statist., 7, 1

Eichler, D., & Cheng, A. F. 1989, ApJ, 336, 360

Espinoza, C. M., Antonopoulou, D., Stappers, B. W., Watts, A., & Lyne, A. G. 2014, MNRAS, 440, 2755

Espinoza, C. M., Lyne, A. G., Stappers, B. W., & Kramer, M. 2011, MNRAS, 414, 1679

Faucher-Giguère, C.-A., & Kaspi, V. M. 2006, ApJ, 643, 332

Ferdman, R. D., Archibald, R. F., & Kaspi, V. M. 2015, ApJ, 812, 95

Gavriil, F. P., Dib, R., & Kaspi, V. M. 2011a, ApJ, 736, 138

Gavriil, F. P., Gonzalez, M. E., Gotthelf, E. V., et al. 2008, Science, 319, 1802

Gavriil, F. P., & Kaspi, V. M. 2004, ApJ, 609, L67

Gavriil, F. P., Kaspi, V. M., Livingstone, M. A., Scholz, P., & Archibald, R. 2011b, The Astronomer's Telegram, 3520, 1

Gavriil, F. P., Kaspi, V. M., & Woods, P. M. 2002, Nature, 419, 142

—. 2004, ApJ, 607, 959

Gehrels, N., & Mészáros, P. 2012, Science, 337, 932

Giacconi, R., Gursky, H., Paolini, F. R., & Rossi, B. B. 1962, Physical Review Letters, 9, 439

Giacconi, R., Murray, S., Gursky, H., et al. 1972, ApJ, 178, 281

Gold, T. 1968, Nature, 218, 731

Goldreich, P., & Julian, W. H. 1969, ApJ, 157, 869

Golenetskii, S. V., Ilinskii, V. N., & Mazets, E. P. 1984, Nature, 307, 41

Golenetskij, S. V., Mazets, E. P., Ilinskij, V. N., & Guryan, Y. A. 1979, Soviet Astronomy Letters, 5, 636

Gonzalez, M., & Safi-Harb, S. 2003, ApJ, 591, L143

Gotthelf, E. V., Halpern, J. P., & Alford, J. 2013, ApJ, 765, 58

Gotthelf, E. V., Vasisht, G., Boylan-Kolchin, M., & Torii, K. 2000, ApJ, 542, L37

Gotthelf, E. V., Tomsick, J. A., Halpern, J. P., et al. 2014, ApJ, 788, 155

Göğüş, E., Lin, L., Kaneko, Y., et al. 2016, ApJ, 829, L25

Gourgouliatos, K. N., & Cumming, A. 2015, MNRAS, 446, 1121

Gunn, J. E., & Ostriker, J. P. 1969, Nature, 221, 454

Haensel, P. 2001, in Lecture Notes in Physics, Berlin Springer Verlag, Vol. 578, Physics of Neutron Star Interiors, ed. D. Blaschke, N. K. Glendenning, & A. Sedrakian, 127

Haensel, P., Zdunik, J. L., & Douchin, F. 2002, A&A, 385, 301

Halpern, J. P., & Gotthelf, E. V. 2010, ApJ, 709, 436

Hansen, B. M. S., & Phinney, E. S. 1997, MNRAS, 291, 569

Harding, A. K. 2007, ArXiv e-prints, arXiv:0710.3517

Harding, A. K., Contopoulos, I., & Kazanas, D. 1999, ApJ, 525, L125

Harding, A. K., & Muslimov, A. G. 2001, ApJ, 556, 987

Harrison, F. A., Craig, W. W., Christensen, F. E., et al. 2013, ApJ, 770, 103

Hascoët, R., Beloborodov, A. M., & den Hartog, P. R. 2014, ApJ, 786, L1

Haskell, B., & Melatos, A. 2015, International Journal of Modern Physics D, 24, 1530008

Helfand, D. J., Collins, B. F., & Gotthelf, E. V. 2003, ApJ, 582, 783

Helfand, D. J., Gotthelf, E. V., & Halpern, J. P. 2001, ApJ, 556, 380

Hewish, A., Bell, S. J., Pilkington, J. D. H., Scott, P. F., & Collins, R. A. 1968, Nature, 217, 709

Heyl, J. S., & Shaviv, N. J. 2002, Phys. Rev. D, 66, 023002

Ho, W. C. G., Espinoza, C. M., Antonopoulou, D., & Andersson, N. 2015, Science Advances, 1, e1500578

Hobbs, G., Lyne, A. G., & Kramer, M. 2010, MNRAS, 402, 1027

Hobbs, G. B., Edwards, R. T., & Manchester, R. N. 2006, MNRAS, 369, 655

Hulleman, F., van Kerkwijk, M. H., & Kulkarni, S. R. 2004, A&A, 416, 1037

Hurley, K., Cline, T., Mazets, E., et al. 1999, Nature, 397, 41

Içdem, B., Baykal, A., & Inam, S. Ç. 2012, MNRAS, 419, 3109

Israel, G. L., Campana, S., Dall'Osso, S., et al. 2007, ApJ, 664, 448

Israel, G. L., Mereghetti, S., & Stella, L. 1994, ApJ, 433, L25

Jahoda, K., Swank, J. H., Giles, A. B., et al. 1996, in Society of Photo-Optical Instrumentation Engineers (SPIE) Conference Series, Vol. 2808, EUV, X-Ray, and Gamma-Ray Instrumentation for Astronomy VII, ed. O. H. Siegmund & M. A. Gummin, 59

Jansen, F., Lumb, D., Altieri, B., et al. 2001, A&A, 365, L1

Johnston, S., & Galloway, D. 1999, MNRAS, 306, L50

Johnston, S., & Karastergiou, A. 2017, ArXiv e-prints, arXiv:1702.03616 [astro-ph.HE]

Kalapotharakos, C., Harding, A. K., & Kazanas, D. 2014, ApJ, 793, 97

Kantor, E. M., & Gusakov, M. E. 2014, ApJ, 797, L4

Kaplan, D. L., & van Kerkwijk, M. H. 2009, ApJ, 705, 798

Kargaltsev, O., Kouveliotou, C., Pavlov, G. G., et al. 2012, ApJ, 748, 26

Kaspi, V. M., Gavriil, F. P., Chakrabarty, D., Lackey, J. R., & Muno, M. P. 2001, ApJ, 558, 253

Kaspi, V. M., Gavriil, F. P., Woods, P. M., et al. 2003, ApJ, 588, L93

Kaspi, V. M., Lackey, J. R., & Chakrabarty, D. 2000, ApJ, 537, L31

Kaspi, V. M., & McLaughlin, M. A. 2005, ApJ, 618, L41

Kaspi, V. M., Roberts, M. S. E., & Harding, A. K. 2006, Isolated neutron stars, ed. W. H. G. Lewin & M. van der Klis, 279

Kennea, J. A., Lien, A. Y., Marshall, F. E., et al. 2016, GRB Coordinates Network, 19735

Klochkov, D., Suleimanov, V., Sasaki, M., & Santangelo, A. 2016, A&A, 592, L12

Kramer, M., Lyne, A. G., O'Brien, J. T., Jordan, C. A., & Lorimer, D. R. 2006, Science, 312, 549

Kuiper, L., & Hermsen, W. 2009, A&A, 501, 1031

Kumar, H. S., & Safi-Harb, S. 2008, ApJ, 678, L43

Lai, D., & Ho, W. C. 2003, Physical Review Letters, 91, 071101

Large, M. I., Vaughan, A. E., & Mills, B. Y. 1968, Nature, 220, 340

Lasky, P. D., Melatos, A., Ravi, V., & Hobbs, G. 2015, MNRAS, 449, 3293

Lattimer, J. M., & Prakash, M. 2001, ApJ, 550, 426

—. 2004, Science, 304, 536

Lazarus, P., Kaspi, V. M., Champion, D. J., Hessels, J. W. T., & Dib, R. 2012, ApJ, 744, 97

Leahy, D. A., & Tian, W. W. 2008, A&A, 480, L25

Lemiere, A., Slane, P., Gaensler, B. M., & Murray, S. 2009, ApJ, 706, 1269

Lin, L., Kouveliotou, C., Göğüş, E., et al. 2011, ApJ, 740, L16

Link, B., Epstein, R. I., & van Riper, K. A. 1992, Nature, 359, 616

Livingstone, M. A., Kaspi, V. M., & Gavriil, F. P. 2010, ApJ, 710, 1710

Livingstone, M. A., Kaspi, V. M., Gotthelf, E. V., & Kuiper, L. 2006, ApJ, 647, 1286

Livingstone, M. A., Ng, C.-Y., Kaspi, V. M., Gavriil, F. P., & Gotthelf, E. V. 2011, ApJ, 730, 66

Livingstone, M. A., Ransom, S. M., Camilo, F., et al. 2009, ApJ, 706, 1163

Lorimer, D., & Kramer, M. 2005, Handbook of Pulsar Astronomy, Cambridge Observing Handbooks for Research Astronomers (Cambridge University Press)

Lyne, A., & Graham-Smith, F. 1990, Pulsar Astronomy, Cambridge Astrophysics (Cambridge University Press)

Lyne, A., Graham-Smith, F., Weltevrede, P., et al. 2013, Science, 342, 598

Lyne, A., Hobbs, G., Kramer, M., Stairs, I., & Stappers, B. 2010, Science, 329, 408

Lyne, A. G., Jordan, C. A., Graham-Smith, F., et al. 2015, MNRAS, 446, 857

Lyne, A. G., Shemar, S. L., & Smith, F. G. 2000, MNRAS, 315, 534

Lyne, A. G., Burgay, M., Kramer, M., et al. 2004, Science, 303, 1153

Lyubarsky, Y., Eichler, D., & Thompson, C. 2002, ApJ, 580, L69

Madsen, K. K., Harrison, F. A., Markwardt, C. B., et al. 2015, ApJS, 220, 8

Manchester, R. N., & Hobbs, G. 2011, ApJ, 736, L31

Manchester, R. N., Hobbs, G. B., Teoh, A., & Hobbs, M. 2005, AJ, 129, 1993

Manchester, R. N., Newton, L. M., & Durdin, J. M. 1985, Nature, 313, 374

Manchester, R. N., & Taylor, J. H. 1977, Pulsars

Marshall, F. E., Guillemot, L., Harding, A. K., Martin, P., & Smith, D. A. 2015, ApJ, 807, L27

—. 2016, ApJ, 827, L39

Mazets, E. P., Golenetskij, S. V., & Guryan, Y. A. 1979a, Soviet Astronomy Letters, 5, 641

Mazets, E. P., Golentskii, S. V., Ilinskii, V. N., Aptekar, R. L., & Guryan, I. A. 1979b, Nature, 282, 587

Meegan, C., Lichti, G., Bhat, P. N., et al. 2009, ApJ, 702, 791

Melatos, A. 1997, MNRAS, 288, 1049

—. 1999, ApJ, 519, L77

Melatos, A., & Link, B. 2014, MNRAS, 437, 21

Melrose, D. B., & Yuen, R. 2016, Journal of Plasma Physics, 82, 635820202

Mereghetti, S., Israel, G. L., & Stella, L. 1998, MNRAS, 296, 689

Mereghetti, S., Pons, J. A., & Melatos, A. 2015, Space Sci. Rev., 191, 315

Mereghetti, S., & Stella, L. 1995, ApJ, 442, L17

Mereghetti, S., Tiengo, A., Stella, L., et al. 2004, ApJ, 608, 427

Michel, F. C. 1969, ApJ, 158, 727

Morton, D. C. 1964, ApJ, 140, 460

Muno, M. P. 2007, in American Institute of Physics Conference Series, Vol. 924, The Multicolored Landscape of Compact Objects and Their Explosive Origins, ed. T. di Salvo, G. L. Israel, L. Piersant, L. Burderi, G. Matt, A. Tornambe, & M. T. Menna, 166

Ng, C.-Y., Kaspi, V. M., Ho, W. C. G., et al. 2012, ApJ, 761, 65

Ng, C.-Y., Slane, P. O., Gaensler, B. M., & Hughes, J. P. 2008, ApJ, 686, 508

Ng, C.-Y., Kaspi, V. M., Dib, R., et al. 2011, ApJ, 729, 131

Oda, M. 1964, Nature, 202, 1321

Olausen, S. A., & Kaspi, V. M. 2014, ApJS, 212, 6

Olausen, S. A., Zhu, W. W., Vogel, J. K., et al. 2013, ApJ, 764, 1

Ostriker, J. 1968, Nature, 217, 1227

Owen, B. J. 2005, Physical Review Letters, 95, 211101

Özel, F., & Freire, P. 2016, ARA&A, 54, 401

Pacini, F. 1967, Nature, 216, 567

Palmer, D. M., Barthelmy, S., Gehrels, N., et al. 2005, Nature, 434, 1107

Palomba, C. 2000, A&A, 354, 163

Parent, D., Kerr, M., den Hartog, P. R., et al. 2011, ApJ, 743, 170

Parfrey, K., Beloborodov, A. M., & Hui, L. 2012, ApJ, 754, L12

—. 2013, ApJ, 774, 92

Perna, R., & Pons, J. A. 2011, ApJ, 727, L51

Pethick, C. J., & Ravenhall, D. G. 1991, Annals of the New York Academy of Sciences, 647, 503

Pétri, J. 2015, MNRAS, 450, 714

Pines, D., & Alpar, M. A. 1985, Nature, 316, 27

Pons, J. A., Link, B., Miralles, J. A., & Geppert, U. 2007, Physical Review Letters, 98, 071101

Pons, J. A., & Perna, R. 2011, ApJ, 741, 123

Potekhin, A. Y. 2010, Physics Uspekhi, 53, 1235

Radhakrishnan, V., & Manchester, R. N. 1969, Nature, 222, 228

Radhakrishnan, V., & Srinivasan, G. 1982, Current Science, 51, 1096

Ransom, S. M., Eikenberry, S. S., & Middleditch, J. 2002, AJ, 124, 1788

Ray, P. S., Kerr, M., Parent, D., et al. 2011, ApJS, 194, 17

Rea, N., Borghese, A., Esposito, P., et al. 2016, ApJ, 828, L13

Rea, N., & Esposito, P. 2011, Astrophysics and Space Science Proceedings, 21, 247

Rea, N., Esposito, P., Turolla, R., et al. 2010, Science, 330, 944

Rea, N., Israel, G. L., Pons, J. A., et al. 2013, ApJ, 770, 65

Reichley, P. E., & Downs, G. S. 1969, Nature, 222, 229

Roming, P. W. A., Kennedy, T. E., Mason, K. O., et al. 2005, Space Sci. Rev., 120, 95

Ruderman, M. 1969, Nature, 223, 597

Ruderman, M. A., & Sutherland, P. G. 1975, ApJ, 196, 51

Safi-Harb, S., & Kumar, H. S. 2008, ApJ, 684, 532

Saslaw, W. C. 1968, Nature, 217, 1222

Scholz, P., Archibald, R. F., Kaspi, V. M., et al. 2014a, ApJ, 783, 99

Scholz, P., & Kaspi, V. M. 2011, ApJ, 739, 94

Scholz, P., Kaspi, V. M., & Cumming, A. 2014b, ApJ, 786, 62

Scholz, P., Ng, C.-Y., Livingstone, M. A., et al. 2012, ApJ, 761, 66

Shaham, J. 1977, ApJ, 214, 251

Smits, R., Kramer, M., Stappers, B., et al. 2009, A&A, 493, 1161

Spitkovsky, A. 2004, in IAU Symposium, Vol. 218, Young Neutron Stars and Their Environments, ed. F. Camilo & B. M. Gaensler, 357

Staelin, D. H., & Reifenstein, III, E. C. 1968, Science, 162, 1481

Stairs, I. H., Lyne, A. G., & Shemar, S. L. 2000, Nature, 406, 484

Strüder, L., Briel, U., Dennerl, K., et al. 2001, A&A, 365, L18

Tam, C. R., Gavriil, F. P., Dib, R., et al. 2008, ApJ, 677, 503

Taverna, R., Muleri, F., Turolla, R., et al. 2014, MNRAS, 438, 1686

Tendulkar, S. P., Kaspi, V. M., Archibald, R. F., & Scholz, P. 2016, ArXiv e-prints, arXiv:1610.02268 [astro-ph.HE]

Thompson, C., & Duncan, R. C. 1995, MNRAS, 275, 255

—. 1996, ApJ, 473, 322

Thompson, C., Duncan, R. C., Woods, P. M., et al. 2000, ApJ, 543, 340

Thompson, C., Lyutikov, M., & Kulkarni, S. R. 2002, ApJ, 574, 332

Tiengo, A., Mereghetti, S., Turolla, R., et al. 2005, A&A, 437, 997

Timokhin, A. N. 2010, MNRAS, 408, L41

Tong, H., Xu, R. X., Song, L. M., & Qiao, G. J. 2013, ApJ, 768, 144

Torii, K., Kinugasa, K., Katayama, K., Tsunemi, H., & Yamauchi, S. 1998, ApJ, 503, 843

Tsang, D., & Gourgouliatos, K. N. 2013, ApJ, 773, L17

Tsang, T. 1997, Classical Electrodynamics, Advanced Series on Theoretical Physical Sciences (World Scientific)

Tsujimoto, M., Guainazzi, M., Plucinsky, P. P., et al. 2011, A&A, 525, A25

Tsunemi, H., Mori, K., Miyata, E., et al. 2001, ApJ, 554, 496

Turner, M. J. L., Abbey, A., Arnaud, M., et al. 2001, A&A, 365, L27

Turolla, R. 2009, in Astrophysics and Space Science Library, Vol. 357, Astrophysics and Space Science Library, ed. W. Becker, 141

van Adelsberg, M., & Lai, D. 2006, MNRAS, 373, 1495

van Kerkwijk, M. H., & Kaplan, D. L. 2007, Ap&SS, 308, 191

Vasisht, G., & Gotthelf, E. V. 1997, ApJ, 486, L129

Verner, D. A., Ferland, G. J., Korista, K. T., & Yakovlev, D. G. 1996, ApJ, 465, 487

Viganò, D., Rea, N., Pons, J. A., et al. 2013, MNRAS, 434, 123

Wang, N., Manchester, R. N., Pace, R. T., et al. 2000, MNRAS, 317, 843

Wang, Y., Takata, J., & Cheng, K. S. 2013, ApJ, 764, 51

Wang, Z., & Chakrabarty, D. 2002, ApJ, 579, L33

Watanabe, G., & Maruyama, T. 2011, ArXiv e-prints, arXiv:1109.3511 [nucl-th]

Weisskopf, M. C., Tananbaum, H. D., Van Speybroeck, L. P., & O'Dell, S. L. 2000, in Proc. SPIE, Vol. 4012, X-Ray Optics, Instruments, and Missions III, ed. J. E. Truemper & B. Aschenbach, 2

Weisskopf, M. C., Ramsey, B., O'Dell, S., et al. 2016, in Proc. SPIE, Vol. 9905, Space Telescopes and Instrumentation 2016: Ultraviolet to Gamma Ray, 990517

Weltevrede, P., Johnston, S., & Espinoza, C. M. 2011, MNRAS, 411, 1917

Wilms, J., Allen, A., & McCray, R. 2000, ApJ, 542, 914

Wilson-Hodge, C. A., Ray, P. S., Gendreau, K., et al. 2017, in American Astronomical Society Meeting Abstracts, Vol. 229, American Astronomical Society Meeting Abstracts, 309.04

Wolszczan, A., & Frail, D. A. 1992, Nature, 355, 145

Woods, P. M., Kouveliotou, C., van Paradijs, J., et al. 1999, ApJ, 524, L55

Woods, P. M., Kaspi, V. M., Thompson, C., et al. 2004, ApJ, 605, 378

Younes, G., Kouveliotou, C., & Roberts, O. 2016, GRB Coordinates Network, 19736

Yu, M., Manchester, R. N., Hobbs, G., et al. 2013, MNRAS, 429, 688

Zhang, B., & Harding, A. K. 2000, ApJ, 532, 1150

Zhu, W., Kaspi, V. M., Dib, R., et al. 2008, ApJ, 686, 520

Zhu, W. W., Kaspi, V. M., McLaughlin, M. A., et al. 2011, ApJ, 734, 44